CALCULATION OF FREQUENCY-DEPENDENT PARAMETERS OF UNDERGROUND POWER CABLES WITH FINITE ELEMENT METHOD

By

YANAN YIN

B. Eng., Shanghai Jiaotong University, 1982
M. Sc., Tsinghua University, 1984

A THESIS SUBMITTED IN PARTIAL FULFILLMENT OF
THE REQUIREMENTS FOR THE DEGREE OF
DOCTOR OF PHILOSOPHY

in

THE FACULTY OF GRADUATE STUDIES
DEPARTMENT OF ELECTRICAL ENGINEERING

We accept this thesis as conforming
to the required standard

THE UNIVERSITY OF BRITISH COLUMBIA
September 1990

In presenting this thesis in partial fulfilment of the requirements for an advanced degree at the University of British Columbia, I agree that the Library shall make it freely available for reference and study. I further agree that permission for extensive copying of this thesis for scholarly purposes may be granted by the head of my department or by his or her representatives. It is understood that copying or publication of this thesis for financial gain shall not be allowed without my written permission.

Department of ELECTRICAL ENGINEERING

The University of British Columbia
Vancouver, Canada

Date September 26, 1990

Abstract

In this thesis, the finite element method (FEM) is applied to the calculation of frequency-dependent series impedances and shunt capacitances of underground power cables. The principal equations describing the quasi-magnetic fields and static electric fields are solved with FEM based on the Galerkin technique. The J_S method and the loss-energy method are derived to calculate the impedances of a multiconductor system from its field solution, and the energy method and the surface charge method are derived to calculate the capacitances. With a single-core (SC) coaxial cable, the suitability of quadratic isoparametric elements and high-order simplex elements are studied, and a suitable division scheme is suggested for the auto-mesh program.

The conventional FEM with a field truncation boundary is applied to the impedance calculation of buried SC cables. Suitable locations for the field truncation boundary and division schemes in the earth are studied. The results show that $r_b \geq 12\delta_e$ is required to obtain accurate impedances of shallowly buried cables with the conventional FEM. This requires a large solution region in the earth at low frequencies. A new technique based on the perturbation concept is proposed to reduce the solution region in the earth. Comparisons between the results from the conventional FEM and from the proposed technique with a significantly reduced solution region in the earth show good agreement.

In the case studies, the FEM is applied to the parameter calculation of multiphase SC cables, PT cables, sector-shaped cables, and stranded conductors. The numerical results are compared with those from analytical formulas.

Table of Contents

List of Tables

List of Figures

Acknowledgements

I wish to express my gratitude to my parents, who inspired and supported me to undertake this venture.

I wish to express my sincere appreciation to my supervisor, Dr. Hermann Dommel, for his excellent guidance, encouragement, readiness to help, and patience. I also wish to thank Dr. Martin Wedepohl for sharing his vast experience and offering many constructive suggestions during my thesis work.

I would like to thank the Transmission Engineering Division of B. C. Hydro and Power Authority for providing some of the cable data used in this thesis. The financial support of the System Planning Division of B. C. Hydro and Power Authority and of the University of British Columbia is gratefully acknowledged.

I would like to thank Dr. Jośe Marti and my colleagues Luis Naredo and Liu Guang for many inspiring and helpful discussions, and to Dr. Luis Marti for letting me use his earth return impedance routine.

Appreciation is also expressed to the staff of the Department of Electrical Engineering, UBC, for their assistance, especially to Mr. Robert Ross and Mr. Dave Gagne for their patience and help in answering so many of my questions.

Last but not the least, I thank my wife, Jie, who through her incredible thoughtfulness, encouragement, and patience has helped me with every step during my doctoral program.

Dedicated

TO MY PARENTS

Chapter 1

Introduction

Underground power cables are widely used in electric power systems, and are therefore one of the important components in power system transient analysis. Unlike overhead power lines, cables are geometrically compact. The distances among conductors are comparable with the dimensions of the conductors. The conductors and cables often have non-coaxial geometries (Fig. 1.1), which make closed-form solutions difficult or impossible. Proximity effects are no longer negligible in cables, compared to overhead lines. Because of proximity and skin effects, cables possess much stronger frequency-dependent characteristics than overhead lines, and mathematical models are needed for cables in the transient analysis which include these characteristics.

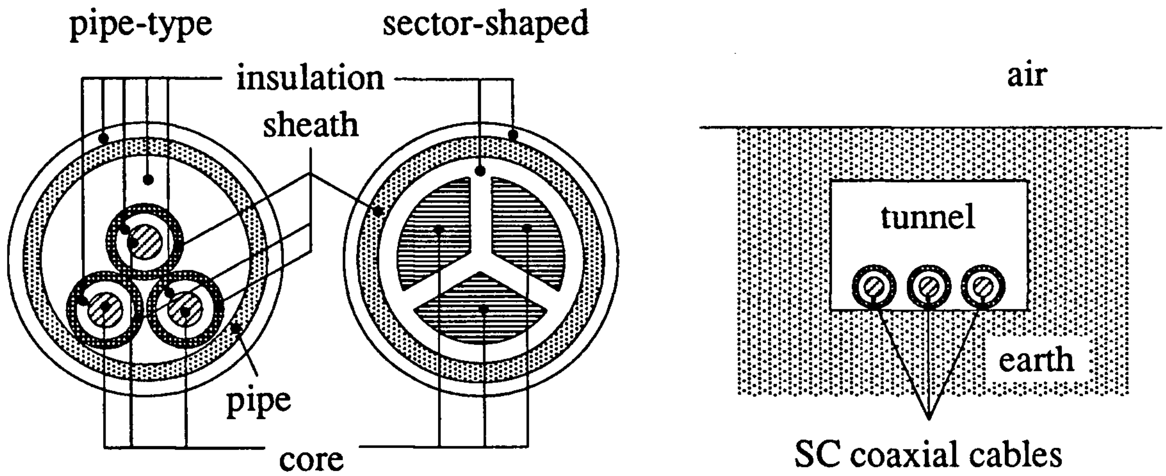

(a) Different types of three-phase cables (b) Tunnel-installed SC coaxial cables

Figure 1.1: Three-phase cables and tunnel-installed single-core (SC) coaxial cables

Several accurate mathematical models for the transient analysis of power cables have been developed. For frequency domain based methods a general model for overhead lines and underground cables was developed by Wedepohl *et al* in 1969 [6]. As the transients are calculated in the frequency domain, the frequency-dependence can easily be included. For time domain transient analysis a general model was developed by J. Marti in 1982 [29]. In this model, curve-fitting techniques are used to find approximate rational functions to replace the frequency-dependent characteristics of mode parameters in the frequency domain. The mode parameters are related to the phase parameters through mode-phase transformation matrices. A similar model was developed by Humpage *et al* in 1980 [25]. In that approach, the z-transformation technique is used, and the curve-fitting is done in the z domain. These two models, however, do not consider the frequency-dependent characteristics of the mode-phase transformation matrix. J. Marti's model was improved by L. Marti in 1988 to take the frequency-dependence of the mode-phase transformation matrix into account [39].

The frequency-dependent phase parameters of the cable, i.e. series impedance matrix and shunt admittance matrix per unit length, are the input data for all the models mentioned above. The calculation of these parameters, however, is not an easy task, especially the calculation of the series impedance matrix. There are mainly two ways to calculate these parameters: analytically and numerically.

In the early days before the arrival of computers, many theoretical studies were done on the calculation of series impedances of overhead lines and of underground power cables. In 1926 Carson derived formulas for the earth return impedance of overhead lines [1], and Pollaczek derived similar formulas for underground cables in the same year [2]. In 1934 Schelkunoff gave the complete solution for the electromagnetic fields inside a single-core (SC) coaxial cable and derived corresponding impedance formulas[3]. The earth return impedance formulas and the impedance formulas for SC coaxial cables are still widely used in modern cable parameter calculation programs [10][23]. With the recent increase in computing power, more sophisticated formulas were developed as well. Tegopoulos *et at* derived the field solution for pipe-type (PT) cables with circular inner conductors in 1971 [8]. The formulas for the impedances of these PT cables were derived by Brown *et al* in 1975 [13].

The closed-form formulas, however, are limited to cables with simple geometries. Even for PT cables with circular inner conductors, several approximations have to be made in order to derive the impedance formulas. If irregular geometric shapes are involved, or if all the skin and proximity effects should be considered in the parameter calculation, then the closed-form formulas are no longer applicable, as there is no analytical solution for those problems. Numerical methods have to be used instead.

In order to calculate the parameters of underground power cables with numerical methods, the corresponding electromagnetic field problem is solved first, and the parameters are then derived from the numerical field solution. Based on the assumptions discussed in Chapter 2, the related electromagnetic fields are split into static electric fields, from which the shunt admittance matrix is calculated, and quasi-static magnetic fields, from which the series impedance matrix is calculated. Because of skin and proximity effects, it is more difficult to solve quasi-static magnetic fields than to solve static electric fields.

Several numerical methods can be applied to solve the quasi-static magnetic fields needed for the series impedance calculation: subdivision method, finite element method (FEM), boundary element method (BEM), and hybrid method.

The subdivision method divides conductors of a multiconductor system into small subconductors such that the current density within the subconductors can be assumed as uniform. A set of linear equations is established by using self and mutual impedance formulas among the subconductors. The series impedance matrix of the multiconductor system can then be found from the coefficient matrix of the linear equations by matrix reduction. The method was first applied to the series impedance calculation of multiconductor systems by Comellini *et al* in 1973 [9]. In their paper, round subconductors with uniform current density were used. Rectangular subconductors and subconductors with other shapes were used by Deeley *et al* [16] and Lucas *et al* [17] in 1978, as well as by Weeks *et al* for microstrip lines in 1979 [22]. This method was applied to the impedance calculation of PT cables by Arizon *et al* in 1988 [38]. With the subdivision method, the series impedance matrix of a multiconductor system is calculated without solving the field equations. Only the conductor regions are needed. The coefficient matrix, however, is a full matrix, and a homogeneous permeability in the space must be assumed. Because uniform current density in each subconductor is generally assumed, a very fine subdivision has to be used to achieve accurate results if strong skin and proximity effects are present.

With the finite element method, the domain of a closed boundary problem is divided into small elements such that the original unknown field distribution in each element can be approximated by certain functions expressed in terms of unknown field variables at element vertices. The field variable values at all the vertices of the FEM mesh can then be determined with variational technique or with Galerkin technique. In the early 1970's, the method began to be applied to eddy-current related problems in power apparatus. It was used to find the field distribution in magnetic structures such as motors by Chari in 1974 [12], in a case where super-conductivity was assumed for the current carrying conductors. The method was applied to study the skin effect in a single current carrying conductor by Chari *et al* in 1977 [14]. It was extended to study the skin effect in multiple current carrying conductor systems by Konrad in 1981 and in 1982 [26][28]. In his papers, source current density J_S was related to measurable conductor currents; therefore, conductor currents replaced J_S to become the forcing function. It was also suggested in his papers that the impedance matrix of a multiconductor system could be calculated from the J_S vector directly. In 1982 Weiss *et al* combined the original FEM equations, which had an unknown J_S vector, with the equations which relate the J_S vector to the conductor currents [31][32]. As a result, the field solution can be found in a single step.

The final linear equations in FEM generally have a symmetric, diagonally dominant, banded, complex coefficient matrix. It is easy for FEM to handle problems with regions having different permeabilities. The method is also flexible with respect to the shape of the elements and to the order of the approximating functions. Open boundary problems, however, cannot be handled easily by FEM, though the ballooning technique can be used for problems with Laplacian exterior regions. Also, the whole problem domain within the closed boundary has to be discretized in FEM.

Instead of discretizing the whole problem domain, only the boundary of the problem domain is divided into small elements with the boundary element method, over which approximating functions with unknown coefficients are assumed. These unknown coefficients are found by applying Green's theorem and the basic solution for impulse sources (Green's function). There are several applications of BEM to eddy-current related problems [24][33]. It has also been used to solve the field distribution in power cables [36]. However, few applications relate to the parameter calculation of multiconductor systems. BEM handles open boundary problems with Laplacian exterior regions easily. It has fewer variables because only the boundary is discretized. The final coefficient matrix, however, is generally an unsymmetric full matrix, and there is no general procedure to derive the Green's functions for arbitrary problems. It may be difficult to apply BEM to the earth impedance calculation where the cable systems are surrounded by the poorly conductive earth occupying half space.

The hybrid method has been suggested to combine the advantages of FEM and BEM. Several applications to eddy-current problems have been reported [30][35].

In this thesis project, FEM is applied to the calculation of the series impedance matrix and shunt admittance matrix of underground power cables. Although FEM has been used to solve eddy-current related problems, most applications have been concerned with the field distribution in the whole problem domain at low frequencies. Only a few studies have been made on the parameter calculation of multiconductor systems[41][42].

The following topics were studied: selection of element types; selection of function orders for high order approximating functions; optimal mesh generation; model development for infinite earth region in FEM; algorithm for solving the final banded complex matrix; and error analysis for different types of elements and for approximating functions with different orders.

In Chapter 2 the principal equations for the calculation of the series impedance matrix ($[Z]$) of underground power cables are derived. The FEM based on the Galerkin technique is used to solve the principal equations. Two formulations for the $[Z]$ calculation of a multiconductor system from the field solution, the J_S method and the loss-energy method, are derived. These formulations are new in the literature, although the concepts already exist.

In Chapter 3 two types of elements in $[Z]$ calculations are discussed. They are high order simplex elements and quadratic isoparametric elements. The accuracy in $[Z]$ calculations, the computational efficiency, and the mesh generation schemes of these elements are studied numerically by calculating the $[Z]$ of SC coaxial cables. The J_S method and the loss-energy method are also compared numerically. The integration matrices of simplex elements are given in the exact fraction form for the first order up to the sixth order.

In Chapter 4 a new technique is developed to include the infinitely large and conductive earth in the FEM in $[Z]$ calculations. This technique reduces the solution region drastically.

In Chapter 5 the principal equations for the shunt admittance matrix ($[Y]$) of underground power cables, i.e. Laplace equations, are solved with the FEM, and the formulations to calculate $[Y]$ from the field solution are discussed.

In Chapter 6 the numerical results of several case studies are presented. These studies include the applications of Pollaczek's earth return impedance formula to multiphase underground cables with irregular structures; comparisons of parameters of PT cables or of sector-shaped cables between the results from the FEM and those from the analytical formulas; and the internal resistance calculation of stranded conductors with the FEM.

In Chapter 7 the conclusions of this thesis project are presented and possibilities for future research work are discussed.

Chapter 2

Impedance Calculation with Finite Element Method

2.1 Introduction

This chapter is mainly concerned with the formulation of the field equations and the corresponding FEM solution for the series impedance of underground power cables. The line parameters, i.e. series impedance matrix per unit length ($[Z]$) and shunt admittance matrix per unit length ($[Y]$), are defined in connection with the transmission line equations. The principal equations describing the magnetic fields for the $[Z]$ calculation are derived. These equations are solved by FEM based on the Galerkin technique. In order to retrieve $[Z]$ from the field solution, two methods are suggested. One is to relate the source current density vector $[J_S]$ to $[Z]$ directly, and the other is to split the power loss and the stored magnetic energy in the system into summations of elements which relate to the elements in $[Z]$. As the magnetic fields in SC coaxial cables can be solved analytically, the analytical solutions can be used to check the accuracy of the numerical approaches. In this chapter, a general form of $[Z]$ for SC coaxial cables is given, which will be used frequently in later chapters.

2.2 Definition of Transmission Line Parameters

An overhead transmission line or an underground power cable can be represented as a general multiconductor system. The following assumptions are made for such a system.

1. The system is composed of infinitely long metallic conductors and the earth. The axes of the conductors are parallel to each other and to the surface of the earth.

2. The system is isotropic, linear, and longitudinally homogeneous. All the conductors and dielectrics have constant permittivity ϵ_r, permeability μ_r, and conductivity σ. So does the earth.

3. There is no volume charge inside the conductors and the earth. The charges are only located on the surfaces of the conductors and the earth.

4. Displacement currents in the conductors and the earth are ignored.

5. The frequencies used in the study are far below the value where the corresponding wave length λ becomes comparable with the lateral dimensions of the system.

With the above assumptions, a unique relationship between field quantities, E and H, and circuit quantities, V and I, can be established. Therefore, the electromagnetic fields in the system can be represented by a distributed-parameter electric network. The transmission line equations (telegraph equations), instead of Maxwell's equations, can then be used to describe the system.

Fig. 2.1 shows a longitudinal section with infinitesimal length dz of a $(K+1)$-conductor system. The $(K+1)$th conductor is used as a reference conductor. V_1, V_2, ..., V_K are the conductor voltages with respect to the reference conductor $K+1$, and I_1, I_2, ..., I_K are the conductor currents. They are phasors. The z axis is in parallel with the axes of conductors.

The circuit representation of the system in the frequency domain is shown in Fig. 2.2. In Fig. 2.2, all the variables are in vector form, and all the parameters are in matrix form and are quantities per unit length. $[R(\omega)]$ and $[L_C(\omega)]$ account for the power loss and magnetic energy storage in the conductors, respectively. $[L_D]$ accounts for the magnetic energy stored in the dielectrics. $[C]$ and $[G]$ represent the electric energy storage and the power loss in the dielectrics, respectively.

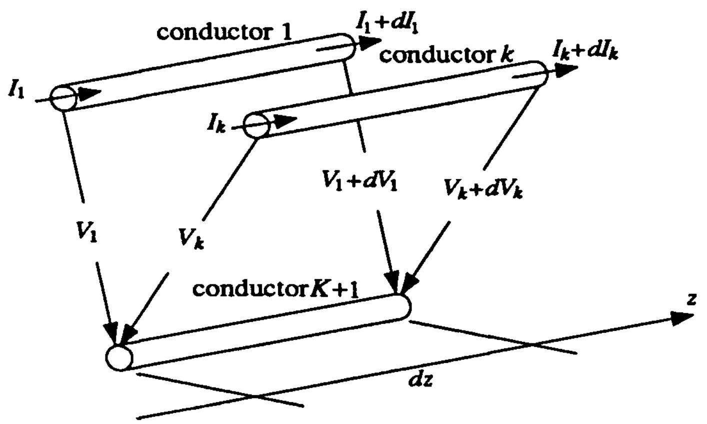

Figure 2.1: A $(K+1)$-conductor system

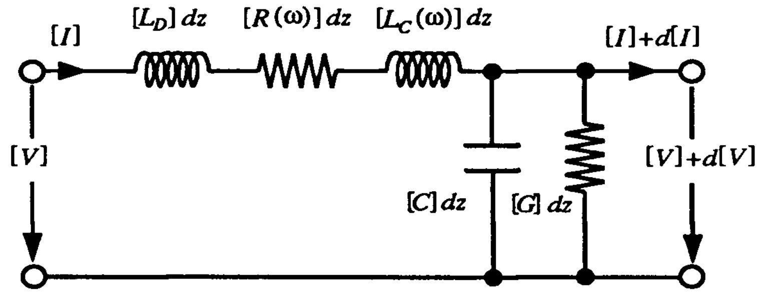

Figure 2.2: Circuit representation of a multiconductor system

The transmission line equations corresponding to Fig. 2.2 are

$$-\frac{d[V]}{dz} = ([R(\omega)] + j\omega[L(\omega)])[I] = [Z(\omega)][I] \tag{2.1}$$

$$-\frac{d[I]}{dz} = ([G] + j\omega[C])[V] = [Y(\omega)][V] \tag{2.2}$$

in which

$$[V] \quad = [V_1, V_2, \ldots, V_K]^T \tag{2.3}$$

$$[I] = [I_1, I_2, \ldots, I_K]^T \tag{2.4}$$

$$[Z(\omega)] = [R(\omega)] + j\omega[L(\omega)] = [R(\omega)] + j\omega([L_C(\omega)] + [L_D]) \tag{2.5}$$

$$[Y(\omega)] = [G] + j\omega[C] \tag{2.6}$$

$[Z(\omega)]$ and $[Y(\omega)]$ are the series impedance matrix per unit length and shunt admittance matrix per unit length of the system, respectively. They are generally referred to as transmission line parameters. In most cases, $[Z(\omega)]$ is a nonlinear function of ω, while $[Y(\omega)]$ can be simplified as $j\omega[C]$ by ignoring $[G]$. For simplicity, ω will be omitted from $[Z(\omega)]$ and $[Y(\omega)]$.

The transmission line equations are the fundamental equations on which all transient analysis models for underground power cables are based [10][29][39]. $[Z]$ and $[Y]$ are the input data for those models. According to the assumptions made before, $[Z]$ and $[Y]$ can be calculated from a quasi-static magnetic field and a static electric field of the system, respectively.

2.3 Principal Equations in Impedance Calculations

The matrix $[Z]$ of an underground power cable can be found from the magnetic field distribution in and around the cable. In order to do so, the principal equations describing the magnetic fields have to be derived first.

Based on the assumptions 1 and 2 given in the previous section, the electromagnetic field of a cable system is two-dimensional and linear. In order to isolate the magnetic field of the system, displacement currents in dielectrics are also ignored in addition to assumption 4. As a result, the original electromagnetic field becomes a quasi-static magnetic field which is excited solely by the conductor currents. Ignoring displacement currents in the series impedance calculation is common practice[1][2]. To justify this assumption, Wedepohl and Efthymiadis rigorously analyzed the overhead line case over the full frequency spectrum[18][19]. They found that the assumption was valid until the height of the conductor above ground became comparable with 1/4 of the wavelength. The same result will hold for a cable system, but since the dielectric spacings are only a few centimeters, differences will only occur above several hundred MHz, which is orders of magnitude above the frequencies of interest in power system transients. Recent comparisons between field tests and simulations also confirm the validity of the assumption[39][43]. The displacement currents are therefore ignored in the series impedance calculation.

With the discussed assumptions, the following equations are derived from Maxwell's equations

$$\nabla \times \mathbf{E} = -j\omega \mathbf{B} \tag{2.7}$$

$$\frac{1}{\mu}\nabla \times \mathbf{B} = \mathbf{J} \tag{2.8}$$

$$\nabla \cdot \mathbf{E} = 0 \tag{2.9}$$

Introducing the magnetic vector potential $\mathbf{A}$ as

$$\mathbf{B} = \nabla \times \mathbf{A} \tag{2.10}$$

and inserting (2.10) into (2.8) and employing unity $\nabla \times \nabla \times \mathbf{A} = \nabla(\nabla \cdot \mathbf{A}) - \nabla^2 \mathbf{A}$, the following equation is obtained

$$\frac{1}{\mu}\nabla(\nabla \cdot \mathbf{A}) - \frac{1}{\mu}\nabla^2 \mathbf{A} = \mathbf{J} \tag{2.11}$$

Assuming

$$\nabla \cdot \mathbf{A} = 0 \tag{2.12}$$

(2.11) gives

$$-\frac{1}{\mu}\nabla^2 \mathbf{A} = \mathbf{J} \tag{2.13}$$

As the current density has only a longitudinal component, $\mathbf{J}$, $\mathbf{E}$, and $\mathbf{A}$ can be written respectively as $J\mathbf{u_z}$, $E\mathbf{u_z}$, and $A\mathbf{u_z}$. $\mathbf{u_z}$ is the unit vector along the z axis. By inserting

(2.10) into (2.7), the following equation can be derived

$$(E + j\omega A)\mathbf{u_z} = -\nabla\phi \tag{2.14}$$

where ϕ is a scalar function. Reference [28] gives the following properties of ϕ in a conductor: the equal value surfaces of ϕ are perpendicular to the z axis and $\nabla\phi$ is a constant within each conductor. These properties make it possible to define a unique voltage between one conductor and the reference conductor at a location along the system. Constant $-\nabla\phi$ in each conductor is defined as the source electric field E_S. The physical meaning of E_S (or $-\nabla\phi$) is the voltage drop along a unit length of the system. The current density corresponding to E_S is called the source current density J_S, which is a constant over the cross section of a conductor. Three quantities are related by

$$J_S\mathbf{u_z} = \sigma E_S\mathbf{u_z} = -\sigma\nabla\phi \tag{2.15}$$

(2.14) can now be written as

$$J = -j\omega\sigma A + J_S \tag{2.16}$$

Combining (2.13) with (2.16), the following linear two-dimensional diffusion equation can be derived

$$\frac{1}{\mu}\nabla^2 A - j\omega\sigma A + J_S = 0 \tag{2.17}$$

The integration of (2.16) over the cross section of a conductor gives

$$I = \int_{S_C} J ds = -j\omega \int_{S_C} \sigma A ds + S_C J_S \tag{2.18}$$

in which S_C is the cross-section area of the conductor. For a multiconductor system, there is one such equation for each conductor. (2.17) and (2.18) are the principal equations describing the quasi-static magnetic fields needed for the $[Z]$ calculation. These equations are solved with FEM in the next section.

2.4 FEM Based on the Galerkin Technique for the Principal Equations

For a multiconductor system with K conductors, the principal equations in the $[Z]$ calculation can be summarized as

$$\frac{1}{\mu}\nabla^2 A - j\omega\sigma A + J_S = 0 \qquad \text{in } S_R \tag{2.19}$$

$$-j\omega\int_{S_{C_k}} \sigma A ds + S_{C_k} J_{S_k} = I_k \qquad (k = 1, 2, \ldots, K) \tag{2.20}$$

with boundary conditions

$$A|_{\Gamma_0} = g_0(x, y) \tag{2.21}$$

$$\left.\frac{\partial A}{\partial \mathrm{n}}\right|_{\Gamma_1} = 0 \tag{2.22}$$

S_R is the solution region surrounded by boundary $\Gamma = \Gamma_0 + \Gamma_1$. S_{C_k} and J_{S_k} are the cross-section area and the source current density of the kth conductor, respectively. $g_0(x, y)$ is a known function. Γ_0 and Γ_1 are the Dirichlet boundary and the homogeneous Neumann boundary, respectively.

2.4.1 The Galerkin technique for solving differential equations

The Galerkin technique approximates the field distribution A satisfying the differential equation (2.19) by a finite set of base functions φ_n $(n = 1, 2, \ldots, N)$ as

$$A = \psi_0 + \sum_{n=1}^{N} a_n \varphi_n \tag{2.23}$$

where $a_1, a_2, \ldots, a_N$ are unknown coefficients. ψ_0 is such that

$$\psi_0|_{\Gamma_0} = g_0 \tag{2.24}$$

φ_1, φ_2, ..., φ_N form a subset of the complete base functions of A. φ_n satisfies the boundary condition

$$\varphi_n|_{\Gamma_0} = 0 \qquad (n = 1, 2, \ldots, N) \tag{2.25}$$

Putting the approximate solution (2.23) into (2.19), a residual is introduced as

$$R(A) = \frac{1}{\mu}\nabla^2 A - j\omega\sigma A + J_S \qquad \text{in } S_R \tag{2.26}$$

The Galerkin technique forces this residual to satisfy the following integral equation

$$\int_{S_R} R(A)\varphi_n ds = 0 \qquad (n = 1, 2, \ldots, N) \tag{2.27}$$

The above equation means that the projection of the residual on each base function is zero, or the residual is orthogonal to all the base functions. As there are N integral equations in (2.27), N unknown coefficients in (2.23) can be determined completely by (2.27).

The forms of the base functions (also called trial or shape functions) will be discussed in the next chapter. In general, they should be simple functions. Polynomials are among popular base functions because they can be easily differentiated and integrated.

With (2.23) and (2.26), (2.27) becomes

$$\begin{aligned} \int_{S_R} \frac{1}{\mu}\left(\nabla\cdot\nabla(\psi_0 + \sum_{n=1}^{N} a_n\varphi_n)\right)\varphi_m ds \quad - \quad \int_{S_R} j\omega\sigma(\psi_0 + \sum_{n=1}^{N} a_n\varphi_n)\varphi_m ds + \\ + \int_{S_R} J_S\varphi_m ds = 0 \qquad\qquad (m = 1, 2, \ldots, N) \end{aligned} \tag{2.28}$$

Applying Green's formula $\nabla\cdot(v\nabla u) = \nabla v\cdot\nabla u + v\nabla^2 u$, the first term in the above equation becomes

$$\begin{aligned} -\int_{S_R} \frac{1}{\mu}\nabla\varphi_m\cdot\nabla(\psi_0 + \sum_{n=1}^{N} a_n\varphi_n)ds + \int_{S_R} \frac{1}{\mu}\nabla\cdot(\varphi_m\nabla(\psi_0 + \sum_{n=1}^{N} a_n\varphi_n))ds \\ = -\int_{S_R} \frac{1}{\mu}\nabla\varphi_m\cdot\nabla(\psi_0 + \sum_{n=1}^{N} a_n\varphi_n)ds + \oint_{\Gamma_0+\Gamma_1} \frac{1}{\mu}\varphi_m(\frac{\partial\psi_0}{\partial \mathrm{n}} + \sum_{n=1}^{N} a_n\frac{\partial\varphi_n}{\partial \mathrm{n}})d\Gamma \\ (m = 1, 2, \ldots, N) \end{aligned} \tag{2.29}$$

It is shown in [44] that boundary conditions in (2.22) and (2.25) can be automatically satisfied if the second loop integral in the above equation is set to zero. Therefore, once φ_n

is established, the N unknown coefficients are found by solving the following equations

$$-\int_{S_R} \frac{1}{\mu} \nabla \varphi_m \cdot \nabla(\psi_0 + \sum_{n=1}^{N} a_n \varphi_n) ds \quad - \quad \int_{S_R} j\omega\sigma(\psi_0 + \sum_{n=1}^{N} a_n \varphi_n)\varphi_m ds + \\ + \int_{S_R} J_S \varphi_m ds = 0 \qquad (m = 1, 2, \ldots, N) \tag{2.30}$$

The differentiation order in the above equations is one order lower than that in (2.28).

It is very difficult to use simple form base functions to approximate the original complicated field function over the whole solution region directly. If the solution region is divided into small subregions such that the original field function changes smoothly in each subregion, it will be possible to approximate the function by simple base functions, such as polynomials, within each subregion. This is the main idea behind finite element methods.

2.4.2 The FEM based on the Galerkin technique

With the FEM, the solution region is divided into elements (subregions) and the base functions are systematically established in each element, as required by the Galerkin technique or other techniques for solving the differential equations. The algebraic equations (2.30) can be assembled element by element, and the unknown variables can then be found. The process for dividing the solution region is called meshing process, and the resulting region made up of elements is called a finite element mesh. All the element vertices and additional locations either on the element sides or inside the elements are defined as nodes.

With the Galerkin technique, the values of the field variables at the nodes become the unknowns in (2.23). In the $[Z]$ calculation, the field variable is A, and its nodal values are A_n $(n = 1, 2, \ldots, N)$, with N being the number of nodes within the mesh. The coordinates of A_n are represented by (x_n, y_n). The shape function φ_n $(n = 1, 2, \ldots, N)$ in the $[Z]$ calculation satisfies the following conditions.

1. φ_n is continuous inside S_R. Therefore, it is continuous across the interelement boundary;

2.
$$\varphi_n(x_m, y_m) = \begin{cases} 1 & m = n \\ 0 & m \neq n \end{cases} \qquad (n, m = 1, 2, \ldots, N)$$

When the solution region is divided, the boundary is also discretized. The boundary will be made of boundary element sides, and the nodes on the boundary element sides become boundary nodes. The original continuous Dirichlet boundary condition is now represented by those boundary nodes on Γ_0 with prescribed values. A similar expression can be written for ψ_0 as

$$\psi_0 = \sum_{i=1}^{N_B} A_{Bi}\varphi_{Bi} \tag{2.31}$$

in which A_{Bi} represents the known node value on the boundary Γ_0, φ_{Bi} represents the corresponding shape function which has the same characteristics as φ_n discussed above, and N_B is the number of Dirichlet boundary nodes on Γ_0.

The nodes can be renumbered such that the first N nodes are the nodes with unknown node values and that the last N_B nodes are Dirichlet boundary nodes with prescribed node values. The total node number is $N_T = N + N_B$. The approximate solution for A can be written as

$$A = \sum_{n=1}^{N_T} A_n\varphi_n \tag{2.32}$$

and (2.30) and (2.20) become

$$\begin{aligned} & -\int_{S_R} \frac{1}{\mu}\nabla\varphi_m \cdot \nabla \sum_{n=1}^{N_T} A_n\varphi_n ds - \int_{S_R} j\omega\sigma\varphi_m \sum_{n=1}^{N_T} A_n\varphi_n ds + \int_{S_R} J_S\varphi_m ds \\ & = -\sum_{n=1}^{N_T} A_n \int_{S_R} \left(\frac{1}{\mu}\nabla\varphi_m \cdot \nabla\varphi_n + j\omega\sigma\varphi_m\varphi_n\right) ds + \int_{S_R} J_S\varphi_m ds = 0 \\ & \qquad (m = 1, 2, \ldots, N) \end{aligned} \tag{2.33}$$

$$-j\omega\sum_{n=1}^{N_T} A_n\left(\int_{S_{C_k}} \sigma\varphi_n ds\right) + S_{C_k} J_{S_k} = I_k \qquad (k = 1, 2, \ldots, K) \tag{2.34}$$

Equations (2.33) and (2.34) are combined together to form the following final algebraic equations in matrix form

$$\begin{pmatrix} [U] + j\omega[T] & -[F] \\ -j\omega[G_C]\,[\,[F]^T,\ [F_B]^T\,] & [S_C] \end{pmatrix} \begin{pmatrix} [A] \\ [J_S] \end{pmatrix} = \begin{pmatrix} [0] \\ [I] \end{pmatrix} \tag{2.35}$$

in which

$$\begin{array}{rcl} U_{mn} & = & \int_{S_R} \frac{1}{\mu}\nabla\varphi_m \cdot \nabla\varphi_n ds \\ T_{mn} & = & \int_{S_R} \sigma\varphi_m\varphi_n ds \\ F_{mk} & = & \int_{S_{C_k}} \varphi_m ds \\ F_{B_{lk}} & = & \int_{S_{C_k}} \varphi_l ds \\ [G_C] & = & diag[\sigma_1, \sigma_2, \ldots, \sigma_K] \\ [S_C] & = & diag[S_{C_1}, S_{C_2}, \ldots, S_{C_K}] \\ [A] & = & [A_1, A_2, \ldots, A_{N_T}]^T \\ [J_S] & = & [J_{S_1}, J_{S_2}, \ldots, J_{S_K}]^T \end{array} \quad \begin{pmatrix} m = 1, 2, \ldots, N \\ n = 1, 2, \ldots, N_T \\ l = N+1, N+2, \ldots, N_T \\ k = 1, 2, \ldots, K \end{pmatrix} \tag{2.36}$$

In matrices $[F]$ and $[F_B]$ only the elements corresponding to the nodes in the conductor regions have non-zero values, and the others are zero. $[S_C]$ is the conductor cross-section area matrix. $[0]$ is a zero vector. $[G_C]$ is the conductivity matrix. It is assumed that each conductor has uniform conductivity in its cross section; otherwise, $[G_C]$ could not be extracted explicitly as in submatrix $[G_C]\,[\,[F]^T,\ [F_B]^T\,]$. In practice, (2.35) is assembled element by element. That means all the integrals in (2.36) become the summations of integrals over the elements as

$$\int_{S_R} = \sum_{i=1}^{M} \int_{S_{E_i}} \tag{2.37}$$

M is the number of elements in the finite element mesh. S_{E_i} $(i = 1, 2, \ldots, M)$ is the region in the ith element. $S_R = S_{E_1} \bigcup S_{E_2} \bigcup \cdots \bigcup S_{E_M}$, and $S_{C_k} \in S_R$. Inside the ith element (2.32) becomes

$$A = \sum_{n=1}^{N_{E_i}} A_n^{E_i} \varphi_n^{E_i} \qquad \text{in } S_{E_i} \tag{2.38}$$

in which N_{E_i} is the number of nodes in the ith element, $A_n^{E_i}$ is the node value of A, and $\varphi_n^{E_i}$ is the shape function defined locally in the element. U_{mn} and T_{mn} become

$$\begin{aligned} U_{mn}^{E_i} &= \frac{1}{\mu_{E_i}} \int_{S_{E_i}} \nabla\varphi_m^{E_i} \cdot \nabla\varphi_n^{E_i} ds \\ T_{mn}^{E_i} &= \sigma_{E_i} \int_{S_{E_i}} \varphi_m^{E_i} \varphi_n^{E_i} ds \\ F_{mk}^{E_i} &= \int_{S_{E_i}} \varphi_m^{E_i} ds \qquad \text{for conductor elements} \\ F_{B_{lk}}^{E_i} &= \int_{S_{E_i}} \varphi_l^{E_i} ds \qquad \text{for conductor elements} \end{aligned} \tag{2.39}$$

where $m = 1, 2, \ldots, N_{E_i}$ excluding boundary nodes, $n = 1, 2, \ldots, N_{E_i}$, $l = 1, 2, \ldots, N_{E_i}$ excluding unknown nodes, and $i = 1, 2, \ldots, M$. Boundary nodes are those on the boundary Γ_0 with prescribed node values whose global numbers are bigger than N, and unknown nodes are the nodes with unknown node values whose global numbers are equal to or smaller than N. The unknown nodes are made up of nodes inside the solution region and of those on the boundary Γ_1. μ_{E_i} and σ_{E_i} are the permeability and conductivity in the ith element, respectively. The above formulas use local node numbers, while each node has a global node number. A node on an element side may be shared by several adjacent elements. When the assembly (2.37) is done, those elements will have contributions to the entry of the same global node in the final matrix (2.35).

In (2.35), the unknown variables are the unknown node values and the source current density J_S in all the conductors, while the forcing factors are the Dirichlet boundary node values and the conductor currents. Once the boundary conditions and the conductor currents are given, the magnetic field represented by the discrete node values of A can be found by solving (2.35). From the field solutions, the series impedance can be calculated. This is the topic of the next section.

2.5 $[Z]$ Calculations from the Field Solutions

Two methods have been developed to calculate $[Z]$ from the field solutions: the J_S method and the loss-energy method. With the J_S method, $[Z]$ is calculated directly from the vector $[J_S]$. With the loss-energy method, the power losses and the stored magnetic energy are calculated from the field solution first. $[R]$ is then calculated from the power losses, and $[L]$ from the stored magnetic energy. The basic concepts on which these two methods are based have existed in the literature. However, they have not been applied to the impedance calculation of multiconductor transmission line systems in the way described here. The loss-energy method used in [41] for the impedance calculation differs from the method of Section 2.5.2.

2.5.1 The J_S method

As mentioned in Section 2.3, the physical meaning of E_S in (2.15) from the field analysis is the voltage drop per unit length along the system[28]. This corresponds to $\frac{d[V]}{dz}$ in (2.1) from the circuit analysis formulation. The relationship is

$$[E_S] = -\frac{d[V]}{dz} \tag{2.40}$$

where $[E_S] = [E_{S1}, E_{S2}, \ldots, E_{SK}]^T$. Therefore,

$$[J_S] = [G_C][E_S] = -[G_C]\frac{d[V]}{dz} = [G_C][Z][I] \tag{2.41}$$

If $[I]$ is assumed as $I_i = 0$ and $I_j \neq 0$ $(i, j = 1, 2, \ldots, K; i \neq j)$, the jth column of $[Z]$ can be derived from the above equation as

$$Z_{ij} = \frac{J_{S_i}}{I_j \sigma_i} \qquad (i = 1, 2, \ldots, K) \tag{2.42}$$

In order to find the whole $[Z]$ matrix of a multiconductor system, the corresponding equation (2.35) has to be solved K times. Each time only one conductor carries current, while the other conductors are open-circuited. This method is simple and straightforward. There is no need to know all the field distributions before calculating $[Z]$.

2.5.2 The loss-energy method

When the field distributions represented by A and J are known, the power loss and the stored magnetic energy in the system can be calculated. They are related to the series resistances and inductances in the system. However, as the system is made up of multiple conductors, the power loss and the magnetic energy of the whole system cannot be used directly in the $[Z]$ calculation. In the following, the formulas for calculating $[Z]$ from the power loss and the stored magnetic energy are derived by comparing the corresponding formulas in the circuit analysis and the field analysis formulations. In the derivation, the loss and the energy are broken down into summations of elements. These elements are then related to the elements in $[Z]$. Equation (2.1) can be represented by the equivalent network shown in Fig. 2.3. For such a resistive-inductive passive network, the complex

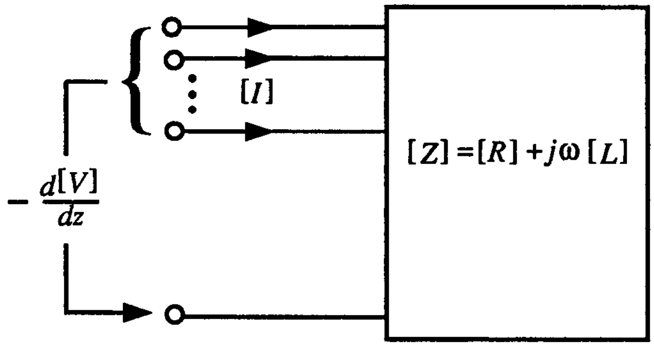

Figure 2.3: An equivalent network for the line

power going into the network is

$$S = P - jQ = \left(-\frac{d[V]}{dz}\right)^{T*} [I] = [I]^{T*}[R][I] - j\omega[I]^{T*}[L][I] \tag{2.43}$$

where S, P, and Q are time-average complex power, time-average power loss, and time-average reactive power in the equivalent network. Assuming $[I] = [I_R] + j[I_I]$ and using the fact that $P = P^T$ and $Q = Q^T$, the following equations can be derived

$$P = [I_R]^T[R][I_R] + [I_I]^T[R][I_I] = \sum_{i=1}^{K}\sum_{j=1}^{K} p_{ij} \tag{2.44}$$

$$Q = \omega([I_R]^T[L][I_R] + [I_I]^T[L][I_I]) = \sum_{i=1}^{K}\sum_{j=1}^{K} q_{ij} \tag{2.45}$$

in which

$$p_{ij} = R_{ij}(I_{R_i}I_{R_j} + I_{I_i}I_{I_j}) \tag{2.46}$$

$$q_{ij} = \omega L_{ij}(I_{R_i}I_{R_j} + I_{I_i}I_{I_j}) \tag{2.47}$$

The time-average magnetic energy W_M stored in the system is related to Q by

$$W_M = \frac{1}{2\omega}Q = \frac{1}{2}([I_R]^T[L][I_R] + [I_I]^T[L][I_I]) = \sum_{i=1}^{K}\sum_{j=1}^{K} w_{M_{ij}} \tag{2.48}$$

in which

$$w_{M_{ij}} = \frac{1}{2}L_{ij}(I_{R_i}I_{R_j} + I_{I_i}I_{I_j}) \tag{2.49}$$

Consequently, if p_{ij} and $w_{M_{ij}}$ can be calculated from the field solution, R_{ij} and L_{ij} will be given by (2.46) and (2.49), respectively.

The formulas to calculate the time-average power loss and the time-average magnetic energy stored in the fields are

$$P = \sum_{k=1}^{K}\int_{S_{C_k}} \frac{JJ^*}{\sigma}ds \tag{2.50}$$

$$W_M = \frac{1}{2}\int_{S_R} BH^*ds = \frac{1}{2}\sum_{k=1}^{K}\mathbf{Re}\left(\int_{S_{C_k}} AJ^*ds\right) \tag{2.51}$$

where all the phasors are in RMS. These formulas, however, only give the total power loss or the magnetic energy in the system. When the system has an arbitrary combination of conductor currents, J in a conductor is caused by all the conductor currents. Because the system is linear, J in the conductor can be written as a summation of different current densities caused by different conductor currents. Assuming $J_{(k)}$ is the current density in the kth conductor, it can be written as

$$J_{(k)} = \sum_{i=1}^{K} J_{(ki)} \qquad (k = 1, 2, \ldots, K) \tag{2.52}$$

where $J_{(ki)}$ is the current density in the kth conductor caused by the current I_i in the ith conductor. (2.50) now becomes

$$\begin{aligned} P &= \sum_{k=1}^{K} \int_{S_{C_k}} \frac{J_{(k)} J^*_{(k)}}{\sigma} ds = \sum_{k=1}^{K} \int_{S_{C_k}} \frac{1}{\sigma} \sum_{i=1}^{K} J_{(ki)} \sum_{i=1}^{K} J^*_{(ki)} ds \\ &= \sum_{k=1}^{K} \int_{S_{C_k}} \frac{1}{\sigma} \sum_{i=1}^{K} \sum_{j=1}^{K} J_{(ki)} J^*_{(kj)} ds = \sum_{i=1}^{K} \sum_{j=1}^{K} \sum_{k=1}^{K} \int_{S_{C_k}} \frac{J_{(ki)} J^*_{(kj)}}{\sigma} ds \\ &= \sum_{i=1}^{K} \sum_{j=1}^{K} p_{ij} \end{aligned} \tag{2.53}$$

$$p_{ij} = \sum_{k=1}^{K} \int_{S_{C_k}} \frac{J_{(ki)} J^*_{(kj)}}{\sigma} ds \tag{2.54}$$

Similarly,

$$\begin{aligned} W_M &= \frac{1}{2} \sum_{k=1}^{K} \mathbf{Re} \left(\int_{S_{C_k}} A_{(k)} J^*_{(k)} ds \right) \\ &= \sum_{i=1}^{K} \sum_{j=1}^{K} \frac{1}{2} \sum_{k=1}^{K} \mathbf{Re} \left(\int_{S_{C_k}} A_{(ki)} J^*_{(kj)} ds \right) = \sum_{i=1}^{K} \sum_{j=1}^{K} w_{M_{ij}} \end{aligned} \tag{2.55}$$

$$w_{M_{ij}} = \frac{1}{2} \sum_{k=1}^{K} \mathbf{Re} \left(\int_{S_{C_k}} A_{(ki)} J^*_{(kj)} ds \right) \tag{2.56}$$

where $A_{(k)} = \sum_{i=1}^{K} A_{(ki)}$. $A_{(ki)}$ is the A in the kth conductor caused by current I_i. Relating (2.54) and (2.56) with (2.46) and (2.49), respectively, gives R_{ij} and L_{ij} as

$$R_{ij} = \left\{ \sum_{k=1}^{K} \int_{S_{C_k}} \frac{J_{(ki)} J^*_{(kj)}}{\sigma} ds \right\} / (I_{R_i} I_{R_j} + I_{I_i} I_{I_j}) \qquad (i, j = 1, 2, \ldots, K) \tag{2.57}$$

$$L_{ij} = \left\{ \sum_{k=1}^{K} \mathbf{Re} \left(\int_{S_{C_k}} A_{(ki)} J^*_{(kj)} ds \right) \right\} / (I_{R_i} I_{R_j} + I_{I_i} I_{I_j}) \quad (i, j = 1, 2, \ldots, K) \tag{2.58}$$

In order to obtain $J_{(ki)}$ and $A_{(ki)}$ $(k, i = 1, 2, \ldots, K)$, (2.35) of the system has also to be solved K times with only one conductor carrying current at a time.

Compared with the J_S method, the loss-energy method needs the full information about the field distributions at least inside the conductors in order to retrieve the $[Z]$ matrix. It also requires additional calculations to evaluate the integrals in (2.57) and (2.58). The two methods are applied to simple coaxial conductor systems in Chapter 3, and the comparisons are made for the elements of $[Z]$ with different kinds of elements.

2.6 Impedances of Single-Core Coaxial Cables

The quasi-static magnetic fields inside single-core (SC) coaxial cables can be solved analytically due to axisymmetrical geometry of the cables. The field solutions were derived by Schelkunoff in 1934[3]. The formulas for the impedance calculation of SC coaxial cables can then be derived from the analytical field solutions. In later chapters, these impedance formulas are used frequently to test various numerical approaches.

Fig. 2.4 shows a SC coaxial cable with K cylindrical conductors. r_{Ak} and r_{Bk}

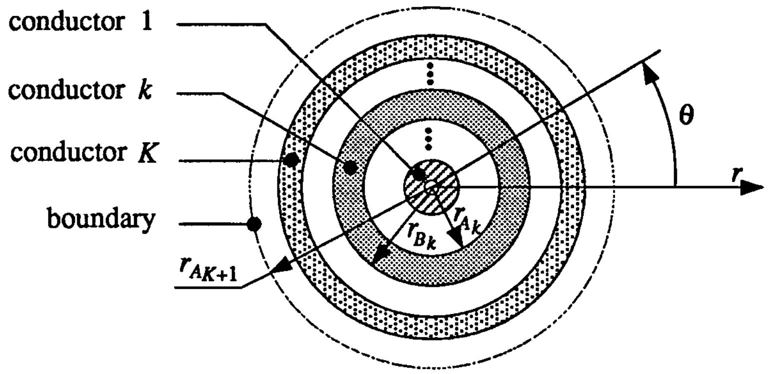

Figure 2.4: A SC coaxial cable with K cylindrical conductors

are internal and external radii of the kth cylindrical conductor, respectively. With the same assumptions as made in Section 2.2, the transverse magnetic field $H\mathbf{u}_\theta$ and the longitudinal electric field $E\mathbf{u}_\mathbf{z}$ satisfy the following equations in cylindrical coordinates

$$\frac{d}{dr}\left(\frac{1}{r}\frac{d(rH)}{dr}\right) = j\omega\sigma\mu H \tag{2.59}$$

$$E = \frac{1}{r\sigma}\frac{d(rH)}{dr} \tag{2.60}$$

The solution for E inside the kth conductor is

$$E(r) = \frac{1}{\sigma p_k}\left(C_{Ik}\mathrm{I}_0(r/p_k) - C_{Kk}\mathrm{K}_0(r/p_k)\right) \qquad r_{Ak} \le r \le r_{Bk} \tag{2.61}$$

where

$$\begin{aligned}
C_{Ik} &= \frac{1}{2\pi C_{Dk}}\left(\frac{I_{Ak}}{r_{Ak}}\mathrm{K}_1(r_{Bk}/p_k) + \frac{I_{Bk}}{r_{Bk}}\mathrm{K}_1(r_{Ak}/p_k)\right) \\
C_{Kk} &= \frac{-1}{2\pi C_{Dk}}\left(\frac{I_{Ak}}{r_{Ak}}\mathrm{I}_1(r_{Bk}/p_k) + \frac{I_{Bk}}{r_{Bk}}\mathrm{I}_1(r_{Ak}/p_k)\right) \\
C_{Dk} &= \mathrm{I}_1(r_{Bk}/p_k)\mathrm{K}_1(r_{Ak}/p_k) - \mathrm{I}_1(r_{Ak}/p_k)\mathrm{K}_1(r_{Bk}/p_k) \\
p_k &= \sqrt{\frac{1}{j\omega\sigma_k\mu_k}}
\end{aligned} \tag{2.62}$$

I_{Ak} and I_{Bk} are internal and external return currents of the kth conductor, respectively. p_k is a complex penetration depth in the kth conductor. I_n, and K_n ($n = 0, 1$) are the modified Bessel functions of the nth order and respectively of the first and second kinds.

E on the internal and external surfaces of the kth conductor can be derived as

$$E(r_{Ak}) = Z_{Ak}I_{Ak} + Z_{Mk}I_{Bk} \tag{2.63}$$

$$E(r_{Bk}) = Z_{Mk}I_{Ak} + Z_{Bk}I_{Bk} \tag{2.64}$$

where

$$Z_{Ak} = \frac{1}{2\pi r_{Ak}\sigma_k p_k C_{Dk}}\left(\mathrm{I}_0(r_{Ak}/p_k)\mathrm{K}_1(r_{Bk}/p_k) + \mathrm{K}_0(r_{Ak}/p_k)\mathrm{I}_1(r_{Bk}/p_k)\right) \tag{2.65}$$

$$Z_{Bk} = \frac{1}{2\pi r_{Bk}\sigma_k p_k C_{Dk}}\left(\mathrm{I}_0(r_{Bk}/p_k)\mathrm{K}_1(r_{Ak}/p_k) + \mathrm{K}_0(r_{Bk}/p_k)\mathrm{I}_1(r_{Ak}/p_k)\right) \tag{2.66}$$

$$Z_{Mk} = \frac{1}{2\pi r_{Ak}r_{Bk}\sigma_k C_{Dk}} \tag{2.67}$$

Z_{Ak}, Z_{Bk}, and Z_{Mk} are defined by Schelkunoff as internal surface impedance, external surface impedance, and transfer impedance of the kth cylindrical conductor, respectively.

Suppose that the system in Fig. 2.4 has a superconductive surface at $r_{A_{K+1}}$. This surface will be used as the reference for the conductor voltages and the return path for the conductor currents. The series impedance matrix of the system can then be derived as [10][23]

$$[Z] = \begin{pmatrix} Z_1^d & Z_2^{od} & Z_3^{od} & \dots & Z_K^{od} \\ Z_2^{od} & Z_2^d & Z_3^{od} & \dots & Z_K^{od} \\ Z_3^{od} & Z_3^{od} & Z_3^d & \dots & Z_K^{od} \\ \vdots & \vdots & \vdots & \ddots & \vdots \\ Z_K^{od} & Z_K^{od} & Z_K^{od} & \dots & Z_K^d \end{pmatrix} \tag{2.68}$$

where

$$Z_i^d = \sum_{k=i}^{K} Z_{EQ_k} - 2\sum_{k=i+1}^{K} Z_{Mk} \qquad (i = 1,2,\dots,K) \tag{2.69}$$

$$Z_i^{od} = \sum_{k=i}^{K} Z_{EQ_k} - Z_{Mi} - 2\sum_{k=i+1}^{K} Z_{Mk} \qquad (i = 2,3,\dots,K) \tag{2.70}$$

$$Z_{EQ_k} = Z_{Bk} + Z_{Dk} + Z_{Ak+1} \qquad (k = 1,2,\dots,K-1) \tag{2.71}$$

$$Z_{EQ_K} = Z_{B_K} + Z_{D_K} \tag{2.72}$$

$$Z_{Dk} = \frac{j\omega\mu_0}{2\pi}\ln\left(\frac{r_{Ak+1}}{r_{Bk}}\right) \qquad (i = 1,2,\dots,K) \tag{2.73}$$

Z_{Ak+1}, Z_{Bk}, and Z_{Mk} are given by (2.65)-(2.67). Z_{Di} is the impedance related to the inductance in the insulation between the kth conductor and the $(k+1)$th conductor.

2.7 Summary

In this chapter the basic assumptions in the impedance calculation of underground power cables with FEM are discussed, and the principal equations are derived from Maxwell's equations. The principal equations are then solved with FEM using the Galerkin technique. The J_S method and the loss-energy method are derived for the impedance calculation from the field solution. The general form of $[Z]$ for SC coaxial cables is also given in this chapter.

Chapter 3

Element Types and Shape Functions

3.1 Introduction

The finite element formulation derived in the last chapter is incomplete because the shape function $\phi_n^{E_i}$ $(n = 1, 2, \ldots, N_{E_i})$ inside an element is still unknown. The shape function $\phi_n^{E_i}$ is related to element shapes and interpolation functions in the elements. In this chapter two kinds of elements are discussed in connection with $[Z]$ calculations: the simplex element and the isoparametric element. The corresponding shape functions of these elements are used to complete the finite element formulation.

In most two-dimensional eddy-current related problems, high-order simplex elements are used to calculate the magnetic fields. These problems are generally dealing with the fields in non-current-carrying conductor regions or non-conductor regions at low frequencies. In $[Z]$ calculations, however, the frequency will vary from 0 to 1 MHz, and accurate solutions for the fields inside the current-carrying conductor regions are very important to obtain $[Z]$ with good accuracy. At high frequencies, the conductor currents are concentrated in narrow regions near the conductor surfaces, which generally follow the contours of conductor surfaces. Under this situation, the curve-sided isoparametric element may be more suitable than the straight-sided simplex element due to the fact that most underground power cables are made from round conductors.

Very little work has been done so far on the shape functions for $[Z]$ calculations. To find out which element is more suitable, the high-order simplex element or the curve-sided isoparametric element, several factors have to be considered: the accuracy of [Z]; the computation efficiency, which depends on the number of nodes in the mesh, on the final matrix bandwidth and pivoting, and on the CPU requirement; and the mesh generation.

In this chapter, SC coaxial cables are used to study the shape functions in [Z] calculations. Because the [Z] for a SC coaxial cable is known, the FEM results with different shape functions can be compared with the theoretical results. This is used as an accuracy criterion. The factors mentioned above are compared for different elements. Also, based on the numerical results, the J_S method and the loss-energy method for calculating [Z] from the field solutions are compared.

3.2 High-Order Simplex Elements

The approximate field solution given by (2.32) in the preceding chapter can be viewed as a two-dimensional interpolation formula. Once the field values at discrete nodes are known, the field value at an arbitrary location within the solution region can be calculated with the interpolation formula. The shape functions in (2.32) can also be established through setting up such an interpolation formula.

As briefly mentioned in Section 2.4.1, the polynomials are among the popular shape functions used in finite element analysis, because they can be differentiated and integrated easily. The corresponding shape functions of the simplex elements and the isoparametric elements discussed in this section and in the next section are based on polynomials. Therefore, the shape functions to be discussed can be treated as interpolation polynomials which satisfy the conditions given in Section 2.4.2: the shape function for the [Z] calculation must be continuous across the interelement boundary; it must reach unity at its associated node and it must be zero at other nodes.

A simplex in N-dimensional space is the minimal possible nontrivial geometric figure defined by $N+1$ vertices. Therefore, a simplex in two dimensions is a triangle. A triangle (simplex) with area S is shown in Fig. 3.1(a). An arbitrary point P inside the triangle can be used to split the triangle into three subtriangles with areas S_1, S_2, and S_3 as shown in the figure. Simplex coordinates are defined as

$$\zeta_i = \frac{S_i}{S} \qquad i = 1,2,3 \tag{3.1}$$

The location of point P can be uniquely defined by the simplex coordinates.

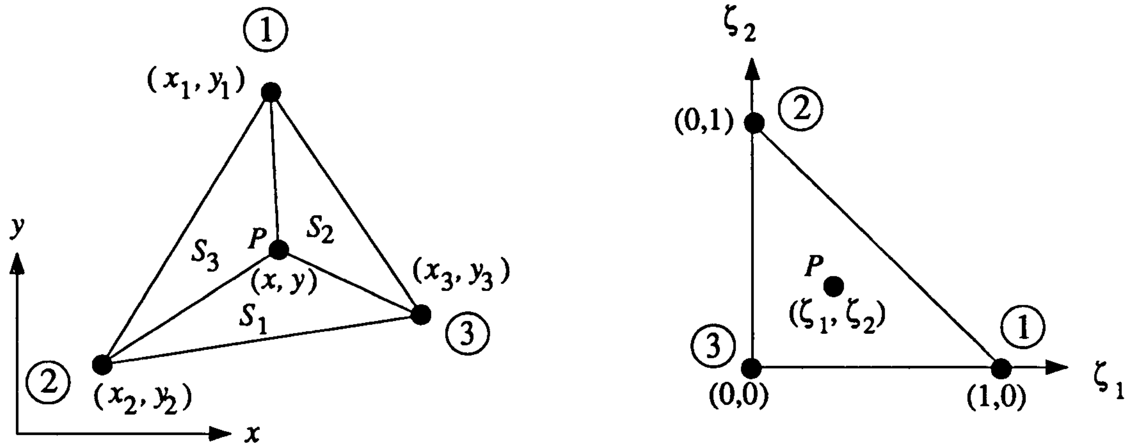

(a) global coordinates (b) simplex (local) coordinates

Figure 3.1: Definition of simplex coordinates in a simplex with area S

From (3.1), the simplex coordinates are obviously varying in the range between zero and one. They are independent of the location of the triangle in the original x-y coordinate system. Only two of the three simplex coordinates are independent because

$$\zeta_1 + \zeta_2 + \zeta_3 = \frac{S_1 + S_2 + S_3}{S} = 1 \tag{3.2}$$

With (3.1) a triangle in x-y (global) coordinates in Fig. 3.1(a) will be transformed into another one in simplex (local) coordinates in Fig. 3.1(b).

The interpolation polynomials required by FEM for $[Z]$ calculations can be easily established with simplex coordinates. The detailed derivations can be found in [7] and [34]. Some key equations are given below, and the integrals in (2.39) are completed.

3.2.1 Shape functions in simplex elements

Applying the formula calculating the area of a triangle from the coordinates of its vertices to (3.1), the relationship between the simplex coordinates, or local coordinates, and x-y coordinates, or global coordinates, can be found as

$$\begin{pmatrix} \zeta_1 \\ \zeta_2 \\ \zeta_3 \end{pmatrix} = \frac{1}{2S} \begin{pmatrix} x_2y_3 - x_3y_2 & y_2 - y_3 & x_3 - x_2 \\ x_3y_1 - x_1y_3 & y_3 - y_1 & x_1 - x_3 \\ x_1y_2 - x_2y_1 & y_1 - y_2 & x_2 - x_1 \end{pmatrix} \begin{pmatrix} 1 \\ x \\ y \end{pmatrix} \tag{3.3}$$

In a simplex the shape functions can be expressed in terms of simplex coordinates as [34]

$$\alpha_{m_1m_2m_3} = P_{m_1}(N_p,\zeta_1)P_{m_2}(N_p,\zeta_2)P_{m_3}(N_p,\zeta_3) \qquad m_1 + m_2 + m_3 = N_p \tag{3.4}$$

in which $P_{m_1}(N_p,\zeta_1)$, $P_{m_2}(N_p,\zeta_2)$, and $P_{m_3}(N_p,\zeta_3)$ are auxiliary polynomials given by

$$P_m(N_p,\zeta) = \frac{1}{m!}\prod_{k=0}^{m-1}(N_p\zeta - k) \qquad m = 1,2,\ldots,N_p \tag{3.5}$$

$$P_0(N_p,\zeta) = 1 \tag{3.6}$$

N_p is the order of the polynomials. Integer indices m_1, m_2, and m_3 have values from 0 to N_p and are related to the locations of nodes inside the triangle. They will be called location indices. The nodes inside a simplex element are at the intersections of three groups of equally spaced parallel lines as shown in Fig. 3.2(a). Each group is in parallel with one of the triangle sides. The lines in a group are numbered from 0 to N_p starting from the line aligned with the triangle side. Therefore, for each node there are three numbers associated with three intersecting lines where the node is located. These numbers indicate the locations of the lines in different groups and are the location indices $m_1 m_2 m_3$ in (3.4). The location indices can be easily extracted from Fig. 3.2(a) into an explicit form as shown in Fig. 3.2(b).

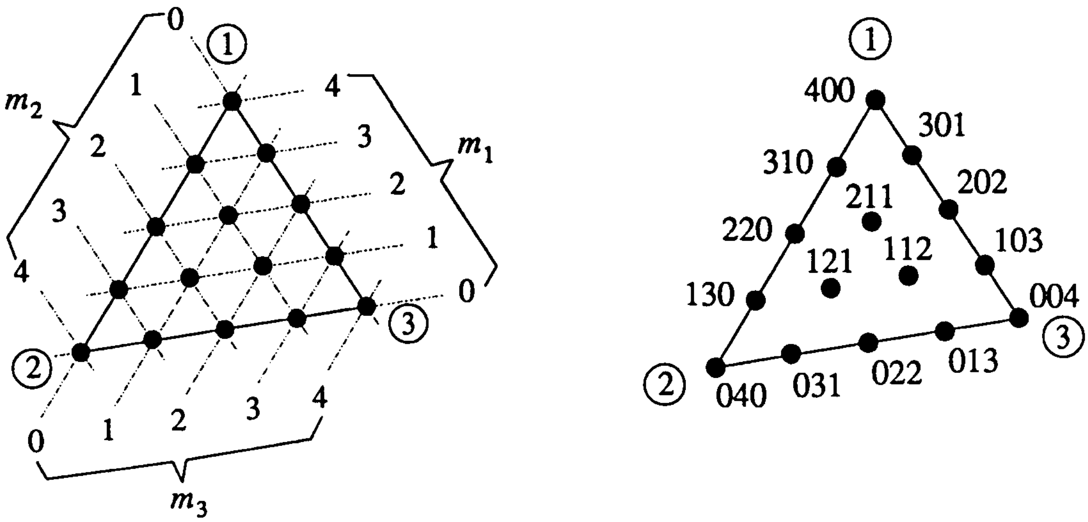

(a) element node arrangement (b) the location indices of the nodes

Figure 3.2: The arrangement and location indices of the nodes in the fourth order simplex element (N_p=4)

3.2.2 Integral matrices of simplex elements

In practice, the nodes in a simplex element can be numbered in any order; however, each node will have the fixed location indices. A commonly used node numbering scheme is shown in Fig. 3.3. For this scheme, the shape functions in (2.38) are related to the shape functions in (3.4) as $\varphi_1^{E_i} = \alpha_{n00}$, $\varphi_2^{E_i} = \alpha_{(n-1)10}, \ldots$, and $\varphi_{N_{B_i}}^{E_i} = \alpha_{00n}$. For the nth order polynomials, $N_{E_i} = (n+1)(n+2)/2$.

With such a node numbering scheme and the shape functions given by (3.4), the integral $U_{mn}^{E_i}$ and $T_{mn}^{E_i}$ in (2.39) can be derived as[34]

$$U_{mn}^{E_i} = \frac{1}{\mu_{E_i}} \sum_{k=1}^{3} Q_{mn}^{(k)} \cot(\theta_k^{E_i}) \tag{3.7}$$

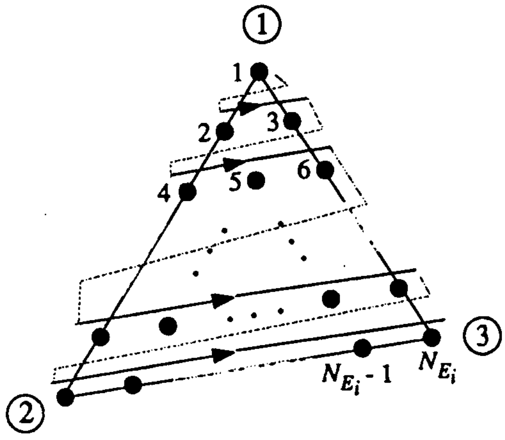

Figure 3.3: A commonly used node numbering scheme

$$T_{mn}^{E_i} = \sigma_{E_i} S_{E_i} T_{S_{mn}} \tag{3.8}$$

in which

$$Q_{mn}^{(k)} = \int_{S_{E_i}} \left(\frac{\partial \varphi_m^{E_i}}{\partial \zeta_{k+1}} - \frac{\partial \varphi_m^{E_i}}{\partial \zeta_{k-1}} \right) \left(\frac{\partial \varphi_n^{E_i}}{\partial \zeta_{k+1}} - \frac{\partial \varphi_n^{E_i}}{\partial \zeta_{k-1}} \right) \frac{ds}{2S_{E_i}} \qquad (k = 1, 2, 3) \tag{3.9}$$

$$T_{S_{mn}} = \int_{S_{E_i}} \varphi_m^{E_i} \varphi_n^{E_i} \frac{ds}{S_{E_i}} \tag{3.10}$$

$\theta_k^{E_i}$ is the included angle of vertex k in element E_i. As all the shape functions are in the form of (3.4), the integration functions in (3.9) and (3.10) are the functions of simplex coordinates only. They are the same for all the elements, independent of the element shapes and sizes. Therefore, they can be evaluated once and for all and tabulated.

From (3.3), the following equation can be derived

$$ds = dxdy = \begin{vmatrix} \frac{\partial x}{\partial \zeta_1} & \frac{\partial x}{\partial \zeta_2} \\ \frac{\partial y}{\partial \zeta_1} & \frac{\partial y}{\partial \zeta_2} \end{vmatrix} d\zeta_1 d\zeta_2 = 2S_{E_i} d\zeta_1 d\zeta_2 \tag{3.11}$$

As the integral functions in (3.9) and (3.10) can be broken into summations of product terms of simplex coordinates, these integral equations are evaluated by

$$\int_{S_{E_i}} \zeta_1^i \zeta_2^j \zeta_3^k \frac{ds}{2S_{E_i}} = \int_0^1 \int_0^{1-\zeta_1} \zeta_1^i \zeta_2^j (1 - \zeta_1 - \zeta_2)^k d\zeta_1 d\zeta_2 = \frac{i!j!k!}{(i+j+k+2)!} \tag{3.12}$$

Under the node numbering scheme shown in Fig. 3.3, the matrices $[Q^{(1)}]$ and $[T_S]$ of the first order to the fourth order have been given in the exact rational form in [7]. These matrices and those of the fifth and the sixth orders are listed in Appendix A as a reference. There are two typesetting errors in [7], one in $[Q^{(1)}]$ of the third order and one in $[T_S]$ of the fourth order.

$[Q^{(2)}]$ and $[Q^{(3)}]$ are related to $[Q^{(1)}]$ by

$$Q^{(2)}_{mn} = Q^{(1)}_{O(m)O(n)} \quad \text{and} \quad Q^{(3)}_{mn} = Q^{(2)}_{O(m)O(n)} = Q^{(1)}_{O(O(m))O(O(n))}$$

$O()$ is the index string for $[Q^{(k)}]$. Fig. 3.4 shows how to find the index string for the fourth order simplex element. The vertices have to be numbered counterclockwise. The nodes

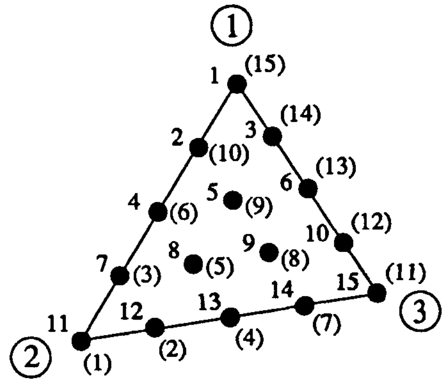

Figure 3.4: $[Q^{(k)}]$ index string of the fourth order simplex element

in the simplex are numbered in the scheme shown in Fig. 3.3 starting from vertex one. The numbers are those without parentheses in Fig. 3.4. The nodes are renumbered in the same way starting from vertex two. The numbers are those with parentheses. Then the first group of numbers are to be the indices in $O()$, and the second group of numbers are to be the corresponding values of $O()$. For the fourth order, $O(1) = 15$, $O(2) = 10$, $O(3) = 14$, and so on. Tab.3.1 shows $[Q^{(k)}]$ index strings for different orders.

Table 3.1: $[Q^{(k)}]$ index strings

Order	Index string $O()$														
1	3	1	2												
2	6	3	5	1	2	4									
3	10	6	9	3	5	8	1	2	4	7					
4	15	10	14	6	9	13	3	5	8	12	1	2	4	7	11
5	21	15	20	10	14	19	6	9	13	18	3	5	8	12	17
	1	2	4	7	11	16									
6	28	21	27	15	20	26	10	14	19	25	6	9	13	18	24
	3	5	8	12	17	23	1	2	4	7	11	16	22		

$F^{E_i}_{mk}$ and $F^{E_i}_{B_{lk}}$ can be calculated from $[T_S]$ as

$$F^{E_i}_{mk} = S_{E_i} \sum_{n=1}^{N_{B_i}} T_{S_{mn}} \tag{3.13}$$

$$F^{E_i}_{B_{lk}} = S_{E_i} \sum_{n=1}^{N_{B_i}} T_{S_{ln}} \tag{3.14}$$

where $m = 1, 2, \ldots, N_{E_i}$, excluding boundary nodes, and $l = 1, 2, \ldots, N_{E_i}$, excluding unknown nodes. Obviously, they can be calculated from the tabulated $[T_S]$ directly. No integral calculation is needed.

High order simplex elements satisfy the condition of interelement boundary continuity. With the nth order shape function, the approximation in (2.38) will also be an nth order polynomial which is uniquely defined by $(n+1)$ nodes on each element side. Therefore, if two adjacent elements have the same node value for each node on the shared element side, the function A will be continuous across the side.

High order simplex elements are simple. The integrations are exact and independent of triangle shapes and sizes and can be done once and for all. The nodes for higher orders can be easily created from the first order element mesh by the computer. Required by the shape function, the element sides are straight, and the nodes are evenly located. This may not be suitable for $[Z]$ calculations of underground power cables because most cables are made of round conductors. In the next section, the isoparametric element with curved sides will be discussed.

3.3 Isoparametric Elements

Cylindrical shells or round solids are common conductor shapes with underground power cables. Although elements with straight sides such as simplex elements can always be used to mesh a region with curved boundaries, many elements are required to fit the mesh into those boundaries. If elements with curved sides are used, instead, the number of elements in the mesh can be reduced.

For simplex elements, it can be seen from (3.3) that the relationship between the global coordinates x-y and the simplex (local) coordinates ζ_1-ζ_2-ζ_3 is linear. Therefore, a straight side element in the local coordinates will be mapped into a straight side element in the global coordinates. If a non-linear relationship is used, a straight side element in the local coordinates can be mapped into a curved side element in the global coordinates.

In this section, two types of curved side elements are briefly discussed: the quadratic quadrilateral isoparametric element and the quadratic triangular isoparametric element. Detailed derivations can be found in the literature [27][37].

3.3.1 Quadratic quadrilateral isoparametric element

In an isoparametric element, the global coordinates x and y are expressed as the interpolation functions of x coordinates and y coordinates, respectively, of the element nodes. These interpolation functions are in the same form as those used for the field variable in the element. In Fig. 3.5, a quadratic quadrilateral element is shown in both global and local coordinates. If the element nodes are numbered as shown in Fig. 3.5(a), interpolation formulas for A, x, and y in element E_i can be written as

$$A = [\beta][A^{E_i}] \tag{3.15}$$

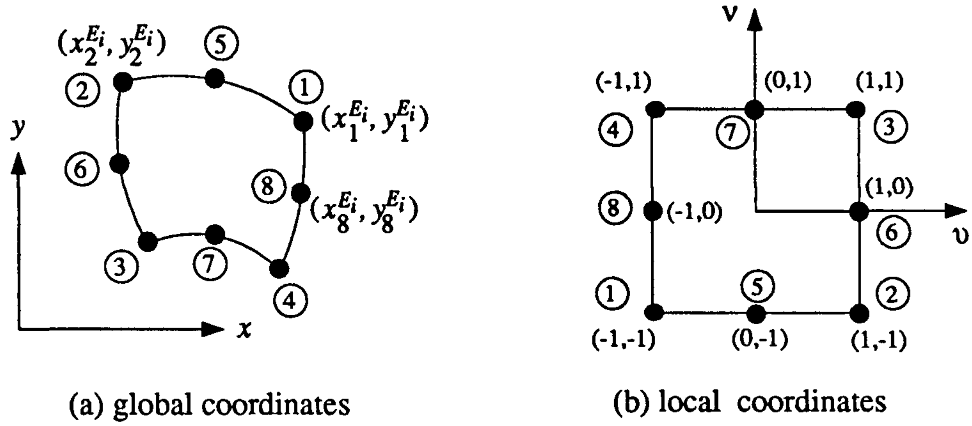

Figure 3.5: Quadratic quadrilateral isoparametric element

$$x = [\beta][x^{E_i}] \tag{3.16}$$

$$y = [\beta][y^{E_i}] \tag{3.17}$$

where

$$\begin{aligned} [A^{E_i}] &= [A_1^{E_i}, A_2^{E_i}, \ldots, A_8^{E_i}]^T \\ [x^{E_i}] &= [x_1^{E_i}, x_2^{E_i}, \ldots, x_8^{E_i}]^T \\ [y^{E_i}] &= [y_1^{E_i}, y_2^{E_i}, \ldots, y_8^{E_i}]^T \\ [\beta] &= [\beta_1, \beta_2, \ldots, \beta_8] \end{aligned} \tag{3.18}$$

$[\beta]$ is a row vector, and its elements are defined by the following expressions in the local coordinates [37].

$$\begin{array}{ll} \beta_1 = \frac{1}{4}(1-\upsilon)(1-\nu)(-1-\upsilon-\nu) & \beta_5 = \frac{1}{2}(1-\upsilon^2)(1-\nu) \\ \beta_2 = \frac{1}{4}(1+\upsilon)(1-\nu)(-1+\upsilon-\nu) & \beta_6 = \frac{1}{2}(1+\upsilon)(1-\nu^2) \\ \beta_3 = \frac{1}{4}(1+\upsilon)(1+\nu)(-1+\upsilon+\nu) & \beta_7 = \frac{1}{2}(1-\upsilon^2)(1+\nu) \\ \beta_4 = \frac{1}{4}(1-\upsilon)(1+\nu)(-1-\upsilon+\nu) & \beta_8 = \frac{1}{2}(1-\upsilon)(1-\nu^2) \end{array} \tag{3.19}$$

From (3.16)-(3.18), the following equations can be derived

$$\begin{bmatrix} \frac{\partial}{\partial x} \\ \frac{\partial}{\partial y} \end{bmatrix} = [J_a^{E_i}]^{-1} \begin{bmatrix} \frac{\partial}{\partial v} \\ \frac{\partial}{\partial \nu} \end{bmatrix} \tag{3.20}$$

$$ds = dxdy = det[J_a^{E_i}]d\nu dv \tag{3.21}$$

where $[J_a^{E_i}]$ is the Jacobian matrix of the transformation given by

$$[J_a^{E_i}] = \begin{bmatrix} \frac{\partial x}{\partial v} & \frac{\partial y}{\partial v} \\ \frac{\partial x}{\partial \nu} & \frac{\partial y}{\partial \nu} \end{bmatrix} = \begin{bmatrix} \frac{\partial}{\partial v} \\ \frac{\partial}{\partial \nu} \end{bmatrix} [\beta] \left([x^{E_i}] \; [y^{E_i}] \right) \tag{3.22}$$

The integrals $U_{mn}^{E_i}$ and $T_{mn}^{E_i}$ in (2.39) can now be evaluated in the local coordinates. The matrix form will be used. $[U^{E_i}]$ and $[T^{E_i}]$ are the matrices corresponding to $U_{mn}^{E_i}$ and $T_{mn}^{E_i}$, respectively. These matrices are 8×8 square matrices. Some of their elements, however, may not be used in the final matrix assembly because subscript m in $U_{mn}^{E_i}$ and $T_{mn}^{E_i}$ only refers to the unknown nodes in the element. $[U^{E_i}]$ and $[T^{E_i}]$ are given by

$$\begin{aligned} [U^{E_i}] &= \frac{1}{\mu_{E_i}} \int_{S_{B_i}} \nabla[\beta] \cdot \nabla[\beta]^T ds = \frac{1}{\mu_{E_i}} \int_{S_{B_i}} \left(\begin{bmatrix} \frac{\partial}{\partial x} \\ \frac{\partial}{\partial y} \end{bmatrix} [\beta] \right)^T \left(\begin{bmatrix} \frac{\partial}{\partial x} \\ \frac{\partial}{\partial y} \end{bmatrix} [\beta] \right) ds \\ &= \frac{1}{\mu_{E_i}} \int_{-1}^{1} \int_{-1}^{1} [D^{E_i}]^T [D^{E_i}] det[J_a^{E_i}] d\nu dv & (3.23) \\ [T^{E_i}] &= \sigma_{E_i} \int_{-1}^{1} \int_{-1}^{1} [\beta]^T [\beta] det[J_a^{E_i}] d\nu dv & (3.24) \end{aligned}$$

in which

$$[D^{E_i}] = \begin{bmatrix} \frac{\partial}{\partial x} \\ \frac{\partial}{\partial y} \end{bmatrix} [\beta] = [J_a^{E_i}]^{-1} \begin{bmatrix} \frac{\partial}{\partial v} \\ \frac{\partial}{\partial \nu} \end{bmatrix} [\beta] \tag{3.25}$$

As the integrals in (3.23) and (3.24) are related to the element node coordinates $[x^{E_i}]$ and $[y^{E_i}]$, $[U^{E_i}]$ and $[T^{E_i}]$ cannot be evaluated once and for all. Also it would be too complicated to integrate (3.23) and (3.24) analytically. Instead, numerical integration formulas are used. With Gaussian quadrature formulas, $[U^{E_i}]$ and $[T^{E_i}]$ become

$$[U^{E_i}] = \frac{1}{\mu_{E_i}} \sum_{j=1}^{N_S} \sum_{k=1}^{N_S} W_j W_k [D^{E_i}(v_j,\nu_k)]^T [D^{E_i}(v_j,\nu_k)] det[J_a^{E_i}(v_j,\nu_k)] \quad (3.26)$$

$$[T^{E_i}] = \sigma_{E_i} \sum_{j=1}^{N_S} \sum_{k=1}^{N_S} W_j W_k [\beta(v_j,\nu_k)]^T [\beta(v_j,\nu_k)] det[J_a^{E_i}(v_j,\nu_k)] \quad (3.27)$$

where (v_j,ν_k) gives the sampling point location in local coordinates, W_j and W_k are the weighting factors related to v_j and ν_k, respectively, and N_S is the number of sampling points in one direction. v_j and ν_k are the sampling point locations in the Gaussian quadrature formula. These locations and associated weighting factors are given in Tab.3.2[5]. If the integrand in (3.23) or in (3.24) is a polynomial of order $2N_S - 1$ for one variable (v or ν), the integral associated with that variable can be exactly calculated with N_S sampling points. Similar to (3.13) and (3.14), $F_{mk}^{E_i}$ and $F_{B_{ik}}^{E_i}$ are calculated from $[T^{E_i}]$.

Table 3.2: Locations of sampling points and weighting factors for Gaussian quadrature

N_S	v_j or ν_j	W_j
1	0	2
2	$\pm\frac{1}{\sqrt{3}}$	1
3	0	$\frac{8}{9}$
	±0.7745966692414834	$\frac{5}{9}$
4	±0.3399810435848563	0.6521451548625461
	±0.8611363115940526	0.3478548451374539
	0	0.5688888888888889
5	±0.5384693101056831	0.4786286704993665
	±0.9061798459386640	0.2369268850561891

3.3.2 Quadratic triangular isoparametric element

For the quadratic triangular isoparametric element shown in Fig. 3.6, all the previous equations, (3.15)-(3.17) and (3.20)-(3.25), are applicable except that the number of nodes is six instead of eight. The shape functions are the same as those of the second order simplex element, as indicated by the similarity between Fig. 3.1(b) and Fig. 3.6(b).

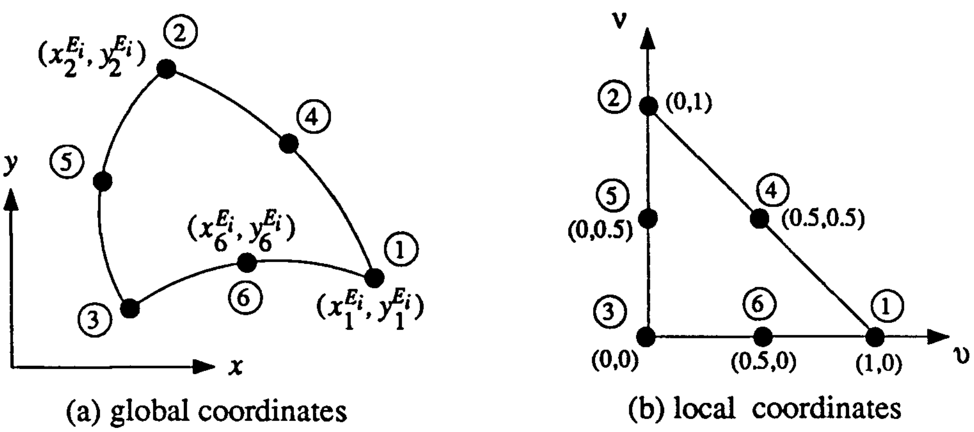

Figure 3.6: Quadratic triangular isoparametric element

Using the node numbering scheme shown in Fig. 3.6 and assuming $\zeta_1 = v$ and $\zeta_2 = \nu$, the shape functions can be derived from (3.2) and (3.4) as

$$
\begin{aligned}
\beta_1 &= \alpha_{200} = \zeta_1(2\zeta_1 - 1) = v(2v - 1) \\
\beta_2 &= \alpha_{020} = \zeta_2(2\zeta_2 - 1) = \nu(2\nu - 1) \\
\beta_3 &= \alpha_{002} = \zeta_3(2\zeta_3 - 1) = (1 - v - \nu)(1 - 2v - 2\nu) \\
\beta_4 &= \alpha_{110} = 4\zeta_1\zeta_2 = 4v\nu \\
\beta_5 &= \alpha_{011} = 4\zeta_2\zeta_3 = 4\nu(1 - v - \nu) \\
\beta_6 &= \alpha_{101} = 4\zeta_1\zeta_3 = 4v(1 - v - \nu)
\end{aligned} \tag{3.28}
$$

The numerical integration formula is applied again to calculate $[U^{E_i}]$ and $[T^{E_i}]$

$$[U^{E_i}] = \frac{1}{\mu_{E_i}} \sum_{j=1}^{N_S} W_j [D^{E_i}(v_j, \nu_j)]^T [D^{E_i}(v_j, \nu_j)] det[J_a^{E_i}(v_j, \nu_j)] \tag{3.29}$$

$$[T^{E_i}] = \sigma_{E_i} \sum_{j=1}^{N_S} W_j [\beta(v_j, \nu_j)]^T [\beta(v_j, \nu_j)] det[J_a^{E_i}(v_j, \nu_j)] \tag{3.30}$$

The locations and associated weighting factors are given in Tab.3.3 [11]. The error order term $o(h_k)$ indicates that the integral can be exactly calculated if the integrand is a polynomial of order $k-1$.

Compared with simplex elements, fewer elements are needed if the above isoparametric elements are used to mesh regions with curved boundaries. Consequently, the number of nodes can be reduced. The procedure for evaluating the integrals of these isoparametric elements, however, is much more complicated. The integrals are solved numerically and have to be calculated within each element. Therefore, the node number reduction with isoparametric elements may not result in a reduction of computation time, as more time may be needed by the integral evaluations. $F_{mk}^{E_i}$ and $F_{B_{ik}}^{E_i}$ are calculated from $[T^{E_i}]$.

Table 3.3: Locations of sampling points and weighting factors for quadratic triangular element

N_S	(v_j, ν_j)	W_j	Error
1	$(\frac{1}{3}, \frac{1}{3})$	$\frac{1}{2}$	$o(h_2)$
3	(0,0.5) (0.5,0) (0.5,0.5)	$\frac{1}{6}$ $\frac{1}{6}$ $\frac{1}{6}$	$o(h_3)$
4	$(\frac{1}{3}, \frac{1}{3})$ $(\frac{11}{15}, \frac{2}{15})$ $(\frac{2}{15}, \frac{11}{15})$ $(\frac{2}{15}, \frac{2}{15})$	$-\frac{27}{96}$ $\frac{25}{96}$ $\frac{25}{96}$ $\frac{25}{96}$	$o(h_4)$
7	$(\frac{1}{3}, \frac{1}{3})$ (0.47014206,0.05961587) (0.47014206,0.47014206) (0.05961587,0.47014206) (0.10128651,0.10128651) (0.79742699,0.10128651) (0.10128651,0.79742699)	0.1125 0.066197075 0.066197075 0.066197075 0.06296959 0.06296959 0.06296959	$o(h_6)$

3.4 Calculation of Integrals in the Loss-Energy Method

In the loss-energy method for $[Z]$ calculations, integrations (2.54) and (2.56) are used to calculate the power losses and stored magnetic energy. With the shape functions given in the preceding two sections, these integrations can be found. For high order simplex elements, p_{ij} in (2.54) becomes

$$p_{ij} = \sum_{k=1}^{K} \sum_{l} \int_{S_{E_l}} \frac{J_{(ki)} J^*_{(kj)}}{\sigma_{E_l}} ds = \sum_{k=1}^{K} \sum_{l} \frac{S_{E_l}}{\sigma_{E_l}} [J^{E_l}_{(ki)}]^T [T_S][J^{E_l *}_{(kj)}] \tag{3.31}$$

in which l refers to elements in conductor k, $[J^{E_l}_{(ki)}]$ and $[J^{E_l *}_{(kj)}]$ are node value vectors of current density distributions $J_{(ki)}$ and $J^*_{(kj)}$ in element E_l, respectively. $J^*_{(kj)}$ is the conjugate of $J_{(kj)}$. Similarly, $w_{M_{ij}}$ in (2.56) is given by

$$w_{M_{ij}} = \sum_{k=1}^{K} \mathbf{Re} \left(\sum_{l} \int_{S_{E_l}} A_{(ki)} J^*_{(kj)} ds \right) = \sum_{k=1}^{K} \mathbf{Re} \left(\sum_{l} S_{E_l} [A^{E_l}_{(ki)}]^T [T_S][J^{E_l *}_{(kj)}] \right) \tag{3.32}$$

in which $[A^{E_l}_{(ki)}]$ is the node value vector of magnetic vector potential distribution $A_{(ki)}$ in element E_l.

For quadratic isoparametric elements, p_{ij} and $w_{M_{ij}}$ are respectively given by

$$p_{ij} = \sum_{k=1}^{K} \sum_{l} \frac{1}{{\sigma_{E_l}}^2} [J^{E_l}_{(ki)}]^T [T^{E_l}][J^{E_l *}_{(kj)}] \tag{3.33}$$

$$w_{M_{ij}} = \sum_{k=1}^{K} \mathbf{Re} \left(\sum_{l} \frac{1}{\sigma_{E_l}} [A^{E_l}_{(ki)}]^T [T^{E_l}][J^{E_l *}_{(kj)}] \right) \tag{3.34}$$

where $[T^{E_l}]$ is given either by (3.27) for quadrilateral elements or by (3.30) for triangular elements.

3.5 General Procedures for $[Z]$ calculations with FEM

With the shape functions discussed in the preceding sections, all the entries in the final matrix given by (2.35) can be calculated. This section concentrates on the procedures for solving the final equations (2.35).

As mentioned in Section 2.4.2 that boundary nodes are numbered after unknown nodes, vector $[A]$ can be partitioned as

$$[A] = \begin{bmatrix} [A_U] \\ [A_B] \end{bmatrix} \tag{3.35}$$

where $[A_U] = [A_1, A_2, \ldots, A_N]^T$ and $[A_B] = [A_{N+1}, A_{N+2}, \ldots, A_{N_T}]^T$. Correspondingly, $[U] + j\omega[T]$ is partitioned as

$$[U] + j\omega[T] = \begin{bmatrix} [D] & [D_B] \end{bmatrix} \tag{3.36}$$

where $[D]$ is an $N \times N$ sparse complex symmetric matrix, $[D_B]$ is an $N \times N_B$ complex matrix. With (3.35) and (3.36), (2.35) becomes

$$\begin{bmatrix} [D] & -[F] \\ [F_H] & [S_C] \end{bmatrix} \begin{bmatrix} [A_U] \\ [J_S] \end{bmatrix} = \begin{bmatrix} [I_{E1}] \\ [I] + [I_{E2}] \end{bmatrix} \tag{3.37}$$

in which

$$\begin{aligned} [F_H] &= -j\omega[G_C][F]^T \\ [I_{E1}] &= -[D_B][A_B] \\ [I_{E2}] &= j\omega[G_C][F_B]^T[A_B] \end{aligned} \tag{3.38}$$

$[I_{E1}]$ and $[I_{E2}]$ are equivalent current vectors due to Dirichlet boundary conditions. In most cases of $[Z]$ calculations, the boundary value vector $[A_B]$ is a zero vector.

In order to make use of the sparsity of $[D]$, the node numbers are generally renumbered with certain algorithms [15] such that the matrix has the structure shown in Fig. 3.7. The shaded areas represent non-zero elements. $[D]$ can now be factorized by algorithms dealing with banded symmetric complex matrices into

$$[D] = [D_L][D_U] \tag{3.39}$$

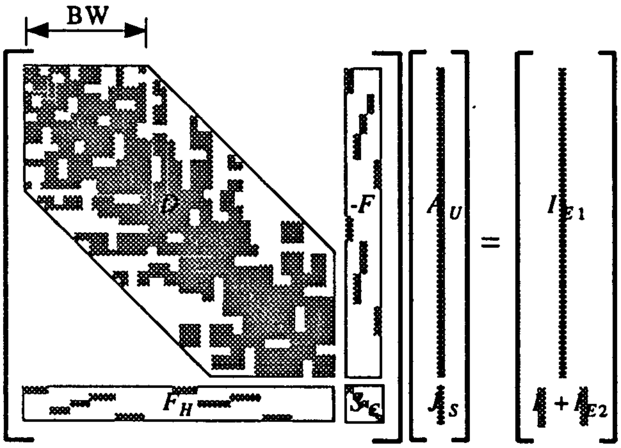

Figure 3.7: Matrix structure of the final equations for $[Z]$ calculations

$[D_L]$ is a banded lower triangular matrix and $[D_U]$ is a banded upper triangular matrix. Using the factors stored in $[D_L]$, (3.37) becomes

$$\begin{bmatrix} [D_U] & [F'] \\ [F_H] & [S_C] \end{bmatrix} \begin{bmatrix} [A_U] \\ [J_S] \end{bmatrix} = \begin{bmatrix} [I'_{E1}] \\ [I] + [I_{E2}] \end{bmatrix} \tag{3.40}$$

in which

$$\begin{aligned} [D_L][F'] &= -[F] \\ [D_L][I'_{E1}] &= [I_{E1}] \end{aligned} \tag{3.41}$$

Because $[D_U]$ is an upper triangular matrix, it can be used directly to delete $[F_H]$ in (3.40), and the following equation can be derived

$$\begin{bmatrix} [D_U] & [F'] \\ [0] & [S'_C] \end{bmatrix} \begin{bmatrix} [A_U] \\ [J_S] \end{bmatrix} = \begin{bmatrix} [I'_{E1}] \\ [I] + [I'_{E2}] \end{bmatrix} \tag{3.42}$$

in which

$$\begin{aligned} [S'_C] &= [S_C] - [F'_H][F'] \\ [I'_{E2}] &= [I_{E2}] - [F'_H][I'_{E1}] \\ [F'_H][D_U] &= [F_H] \end{aligned} \tag{3.43}$$

$[I]$ in (3.42) is left intact. It is the main excitation factor in the $[Z]$ calculation because $[I_{E1}]$ and $[I_{E2}]$ are generally zero vectors. According to the discussions in Section 2.4 and Section 2.5, for an N-conductor system (2.35) has to be solved N times in order to calculate the whole $[Z]$, with only one conductor carrying current at a time. (3.42) can be used repeatedly to solve for $[J_S]$ and $[A_U]$ for different assignments to $[I]$. Once $[I]$ is assigned, $[J_S]$ and $[A_U]$ are solved by

$$\begin{aligned} [S'_C][J_S] &= [I] + [I'_{E2}] \\ [D_U][A_U] &= [I'_{E1}] - [F'][J_S] \end{aligned} \tag{3.44}$$

The general procedure for $[Z]$ calculations with FEM is summerized in the program flowchart shown in Fig. 3.8.

3.6 $[Z]$ Calculation of an SC Coaxial Cable with FEM

In this section, FEM is applied to calculate $[Z]$ of a two-conductor SC coaxial cable. The numerical results are compared with analytical results given by (2.68) in Section 2.6. Optimum division and computation efficiency are studied and comparisons are made among different kinds of elements and different orders of simplex elements. Both the J_S method and the loss-energy method discussed in Section 2.5 are used. The results show that for $[Z]$ calculations of SC coaxial cables isoparametric elements are more efficient with respect to CPU time and storage requirements compared with simplex elements under the same accuracy. The loss-energy method gives the same results (up to eight digits) as the J_S method. When solving the final symmetric banded complex linear equations, a partial pivotal element selection algorithm gives the same solutions as a variable bandwidth Choleski algorithm.

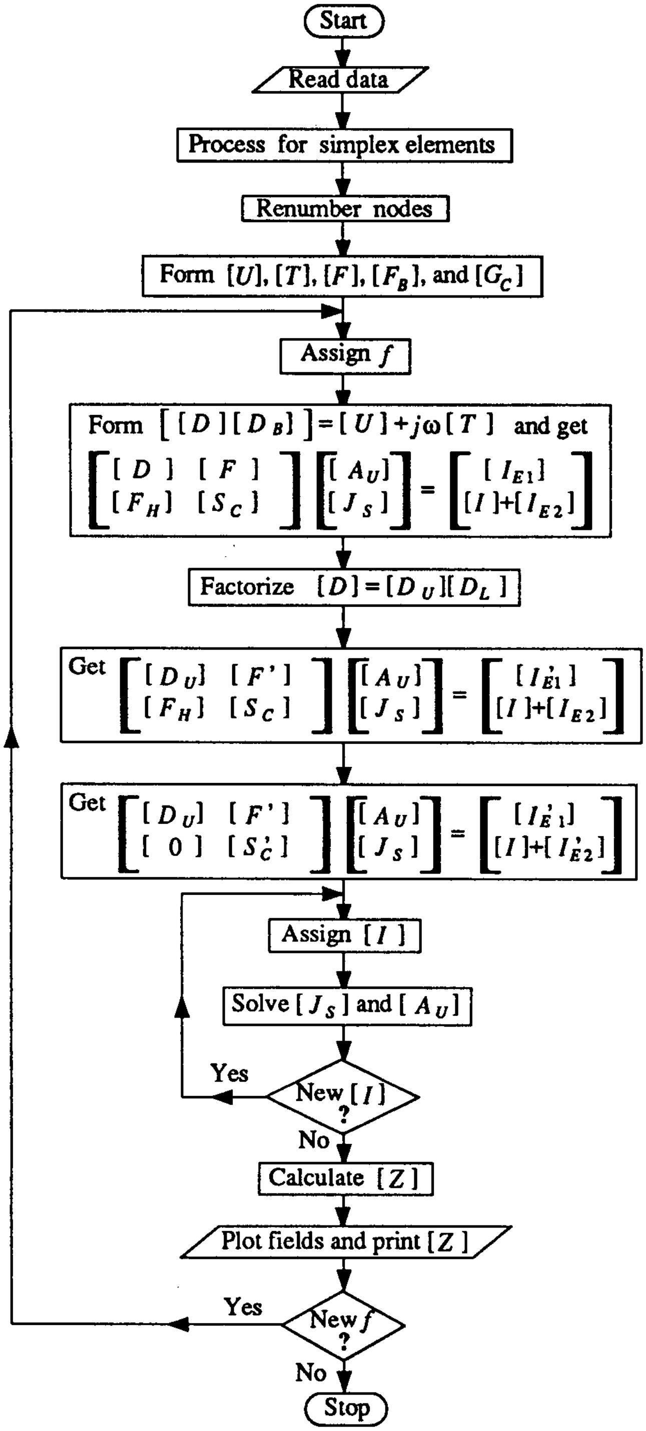

Figure 3.8: Program flow chart for $[Z]$ calculations with FEM

3.6.1 Optimum divisions for SC coaxial cables

Fig. 3.9(a) shows a two-conductor SC coaxial cable as an example for the [Z] calculation, and (b) shows its FEM solution region. The first step in calculating [Z] with FEM is

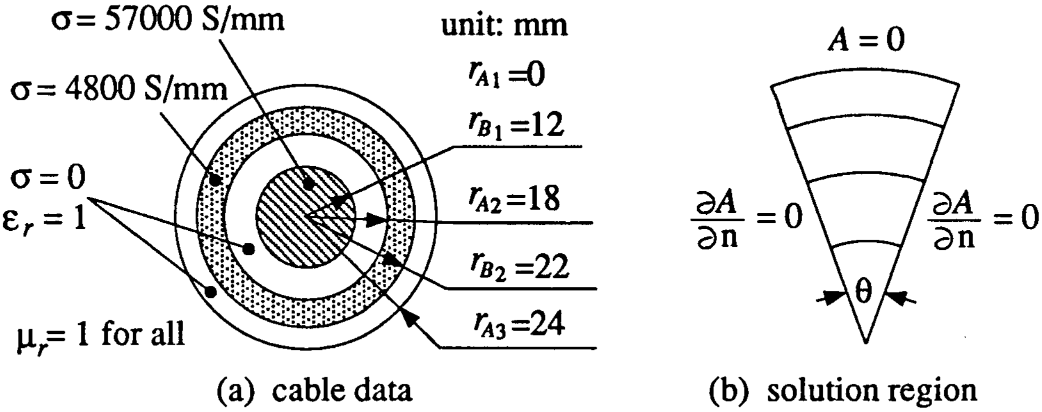

Figure 3.9: Geometry of a SC coaxial cable and its FEM solution region

to mesh the solution region into elements. The fineness of the mesh will affect not only the accuracy but also the amount of computation. In general, a fine mesh improves the accuracy but has more elements and nodes; therefore, it takes more CPU time and more storage.

An optimum division scheme should give a mesh with the least possible number of nodes while maintaining a certain accuracy. For SC coaxial cables there are two relevant factors for the fineness of the mesh: divisions along the radial direction and the span angle θ shown in Fig. 3.9(b)

Radial direction division

Because of axial symmetry, only a wedge-shaped region as shown in Fig. 3.9(b) is needed for the [Z] calculation. A small suitable θ can be used when studying the division scheme along the radial direction.

The basic idea for meshing a solution region is to have fine elements at locations where the field changes fast and to have large elements where the field changes smoothly. At high frequencies, the conductor currents will be concentrated in narrow regions near the conductor surfaces because of skin and proximity effects, and the magnitude of the current density decays quickly towards the centre of the conductors. In the region near the conductor surfaces, the field changes fast, and fine elements should be applied there in order to achieve accurate results. The depth of these regions beneath the conductor surfaces can be estimated by using the penetration depth

$$\delta = \sqrt{\frac{2}{\omega\mu\sigma}} \tag{3.45}$$

The divisions will then depend on δ, which is a function of frequency, conductor conductivity, and conductor permeability.

The wedge-shaped region in Fig. 3.9(b) is enlarged in Fig. 3.10. The dashed lines in the figure are possible radial divisions. d_{ij} is the width of the jth division from a surface

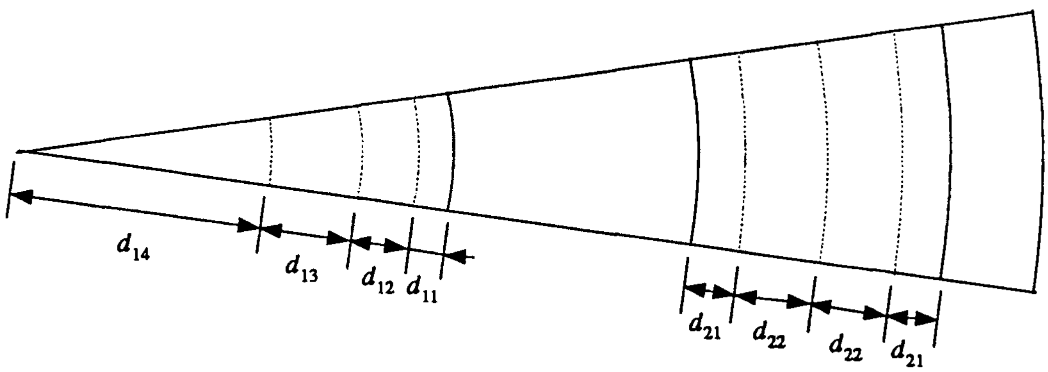

Figure 3.10: Radial divisions for SC coaxial cables

of the ith conductor. $d_{ij} \leq d_{ij+1}$. For the inner most conductor, divisions proceed from the outer surface only, even if the conductor is hollow. For other conductors divisions proceed from both the inner and outer surfaces as shown in Fig. 3.10.

The division width d_{ij} is related to the penetration depth δ. This relationship can be written as

$$d_{ij} = f_{d_j}\delta_i \tag{3.46}$$

where f_{d_j} is a division factor for the jth division and independent of δ_i. f_{d_j} is to be determined from numerical tests. The criteria are the error in $[Z]$ and the error in the J distribution. These two errors are related to each other.

For the cable shown in Fig. 3.9, the division factors found are listed in Tab.3.4, where

Table 3.4: Division factors f_{d_j} for the SC coaxial cable

element	f_{d_1}	f_{d_2}	f_{d_3}	f_{d_4}
sim1	0.3	0.5	0.9	1.8
iso or sim2	1.15	2.8	—	—
sim3	2.25	—	—	—
sim4	3.1	—	—	—
sim5	4.1	—	—	—
sim6	5	—	—	—

"iso" stands for quadratic isoparametric elements including quadrilateral and triangular elements, "sim1" stands for the 1st order simplex element, "sim2" stands for the 2nd order simplex element, and so on. Based on the division factors in Tab.3.4 and the data given in Fig. 3.9(a), the division radii for isoparametric and for the 2nd order simplex elements are calculated and listed in Tab.3.5. Division radii are the radii of division lines. The original material boundaries will also be division lines.

Table 3.5: Division radii for iso and sim2

f (Hz)	division radii (mm)										
6	0	12	18	22	24						
60	0	12	18	22	24						
600	0	8.87	12	18	22	24					
6000	0	8.601	11.01	12	18	20	22	24			
60000	0	10.925	11.687	12	18	19.079	20.921	22	24		
600000	0	11.66	11.901	12	18	18.341	19.171	20.829	21.659	22	24

The meshes generated according to Tab.3.4 are used to calculate $[Z]$. $\theta = 6^{\circ}$ is used in the calculation. The $[R]$ and $[L]$ values are listed in Tab.3.6. "ana" stands for

Table 3.6: $[R]$ and $[L]$ of a two-conductor SC coaxial cable

f (Hz)	element	R (Ω/km)			L (μH/km)		
		R_{11}	R_{12}	R_{22}	L_{11}	L_{12}	L_{22}
6	ana	0.0388114	0.216122×10^{-6}	0.414466	188.610	36.1306	29.4773
	iso	0.0388114	0.215176×10^{-6}	0.414466	188.590	36.1314	29.4758
	sim1	0.0388839	0.215349×10^{-6}	0.415225	187.280	36.1247	29.2811
	sim2	0.0388823	0.214880×10^{-6}	0.415225	188.592	36.1261	29.4689
	sim3	0.0388823	0.215736×10^{-6}	0.415225	188.607	36.1277	29.4742
	sim4	0.0388823	0.215739×10^{-6}	0.415225	188.607	36.1282	29.4747
	sim5	0.0388823	0.215740×10^{-6}	0.415225	188.607	36.1283	29.4748
	sim6	0.0388823	0.215740×10^{-6}	0.415225	188.607	36.1283	29.4749
60	ana	0.0417002	0.216120×10^{-4}	0.414477	186.786	36.1304	29.4772
	iso	0.0417370	0.215174×10^{-4}	0.414477	186.965	36.1312	29.4758
	sim1	0.0418227	0.215352×10^{-4}	0.415235	185.586	36.1245	29.2810
	sim2	0.0418023	0.214878×10^{-4}	0.415235	186.973	36.1259	29.4688
	sim3	0.0417662	0.215733×10^{-4}	0.415235	186.794	36.1275	29.4741
	sim4	0.0417665	0.215737×10^{-4}	0.415235	186.790	36.1280	29.4746
	sim5	0.0417665	0.215737×10^{-4}	0.415235	186.790	36.1281	29.4747
	sim6	0.0417665	0.215737×10^{-4}	0.415235	186.790	36.1281	29.4748
600	ana	0.100575	0.00215824	0.415564	160.987	36.1098	29.4672
	iso	0.100431	0.00214979	0.415553	160.933	36.1141	29.4676
	sim1	0.100645	0.00215072	0.416317	160.109	36.1049	29.2716
	sim2	0.100512	0.00214678	0.416310	160.938	36.1085	29.4605
	sim3	0.100645	0.00215449	0.416320	161.067	36.1070	29.4642
	sim4	0.100658	0.00215453	0.416320	161.005	36.1074	29.4647
	sim5	0.100643	0.00215453	0.416320	161.003	36.1075	29.4648
	sim6	0.100666	0.00215453	0.416320	161.005	36.1076	29.4648
6000	ana	0.683376	0.190695	0.512251	141.923	34.2940	28.5883
	iso	0.682959	0.191040	0.512392	141.926	34.3098	28.5986
	sim1	0.683443	0.191763	0.513133	141.514	34.3483	28.4171
	sim2	0.682408	0.190726	0.513005	141.928	34.3066	28.5928
	sim3	0.684061	0.190419	0.512891	141.999	34.2956	28.5911
	sim4	0.682981	0.190437	0.512876	141.945	34.2972	28.5885
	sim5	0.682998	0.190439	0.512877	141.939	34.2974	28.5887
	sim6	0.683092	0.190439	0.512877	141.939	34.2975	28.5887
60000	ana	4.55387	1.70847	1.64196	110.103	21.5995	21.6613
	iso	4.54685	1.70634	1.64644	110.053	21.5830	21.6629
	sim1	4.56176	1.71946	1.63998	109.402	21.4431	21.5415
	sim2	4.55291	1.70905	1.64730	110.056	21.5819	21.6573
	sim3	4.57740	1.71047	1.64424	110.144	21.6141	21.6731
	sim4	4.55865	1.71048	1.64354	110.105	21.6007	21.6620
	sim5	4.55860	1.71067	1.64278	110.109	21.5999	21.6622
	sim6	4.55913	1.71055	1.64367	110.109	21.6004	21.6619
600000	ana	13.9902	5.11638	5.11640	102.208	18.7503	18.7503
	iso	13.9102	5.08706	5.08729	102.188	18.7471	18.7467
	sim1	13.8688	5.08011	5.07796	101.775	18.7058	18.7052
	sim2	13.9682	5.10549	5.10596	102.169	18.7377	18.7375
	sim3	14.0963	5.12703	5.13941	102.214	18.7554	18.7562
	sim4	14.0001	5.12097	5.12041	102.203	18.7487	18.7487
	sim5	14.0028	5.12067	5.12070	102.204	18.7476	18.7476
	sim6	14.0079	5.12252	5.12254	102.204	18.7475	18.7475

analytical results given by (2.68). Compared with analytical results the overall errors of the numerical results are less than 1%. The division radii listed in Tab.3.5 are also used for other frequencies with similar magnitudes. The overall errors of the numerical results in the frequency range from 0 to 1MHz are less than 1.2% for isoparametric elements, less than 1.8% for the 1st order simplex elements, and less than 1% for other order simplex elements. The corresponding current density distributions in the radial direction at 6kHz and 60kHz are plotted in Fig. 3.11 and Fig. 3.12, respectively.

Span angle

In practical problems, axial symmetry does not always exist to give the simple wedge-shaped solution regions shown in Fig. 3.9(b). Instead, a whole circular region as in Fig. 3.9(a) may have to be meshed. A larger span angle θ results in a smaller number of elements and nodes. For straight-sided simplex elements, a larger θ means a larger "misfit" of the element sides into the conductor shapes. This misfit will introduce errors. Curve-sided isoparametric elements can be fitted into the conductor shapes nicely, even with θ larger than 90°. This enables isoparametric elements to maintain almost the same accuracy with large θ as that with small θ.

Fig. 3.13 gives the maximum errors in numerical results of $[R]$ and $[L]$ as functions of θ. The divisions along the radial direction are still based on Tab.3.4. For the 4th, 5th, and 6th order simplex elements the results are very similar to the 3rd order simplex element. From these results it can be seen that high orders in simplex elements do not really improve the accuracy when θ is large. For isoparametric elements the maximum errors are less than 4% for $[R]$ and 1.1% for $[L]$ at $\theta = 120^{\circ}$.

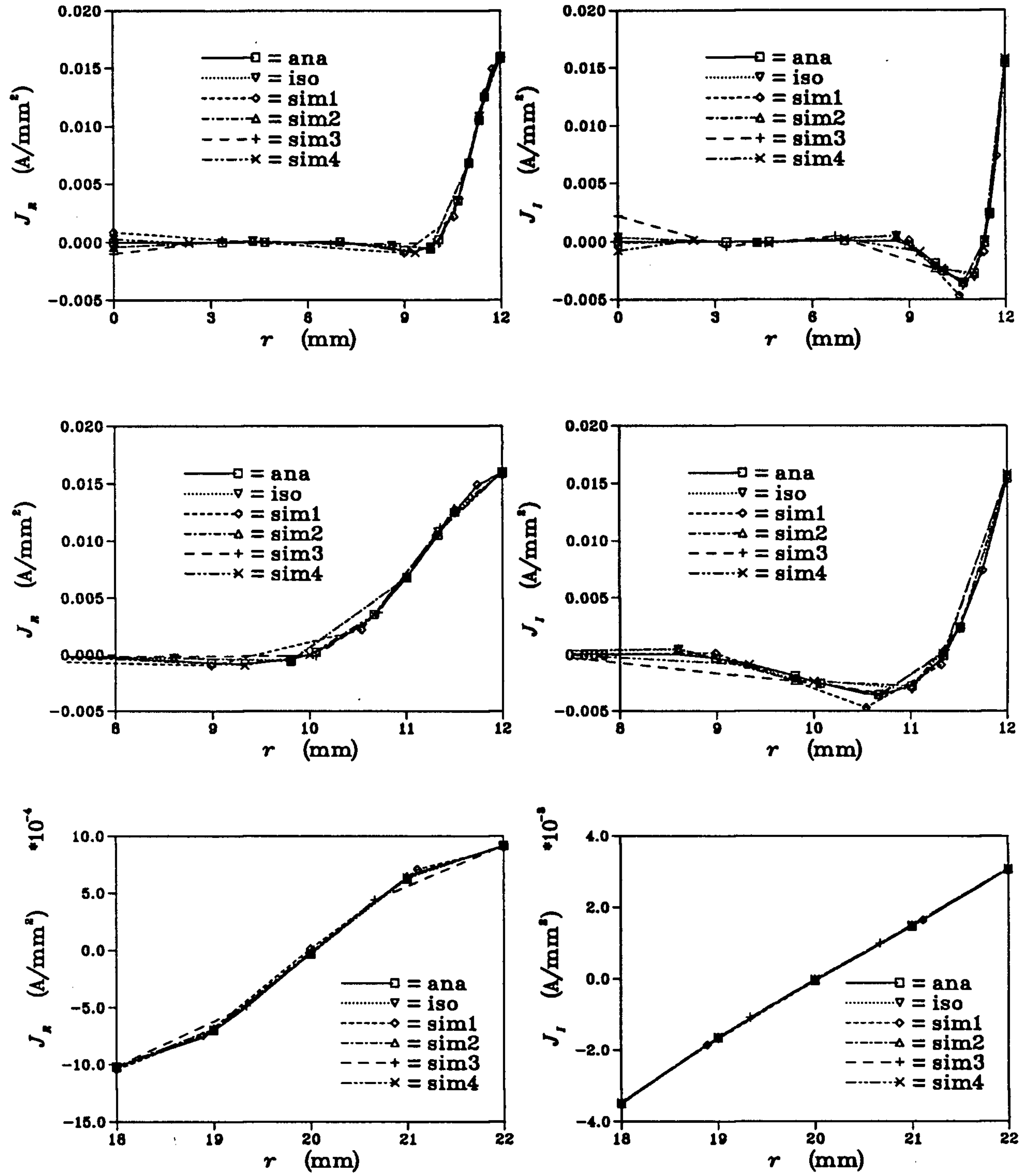

Figure 3.11: Current density distribution in the SC coaxial cable at 6kHz

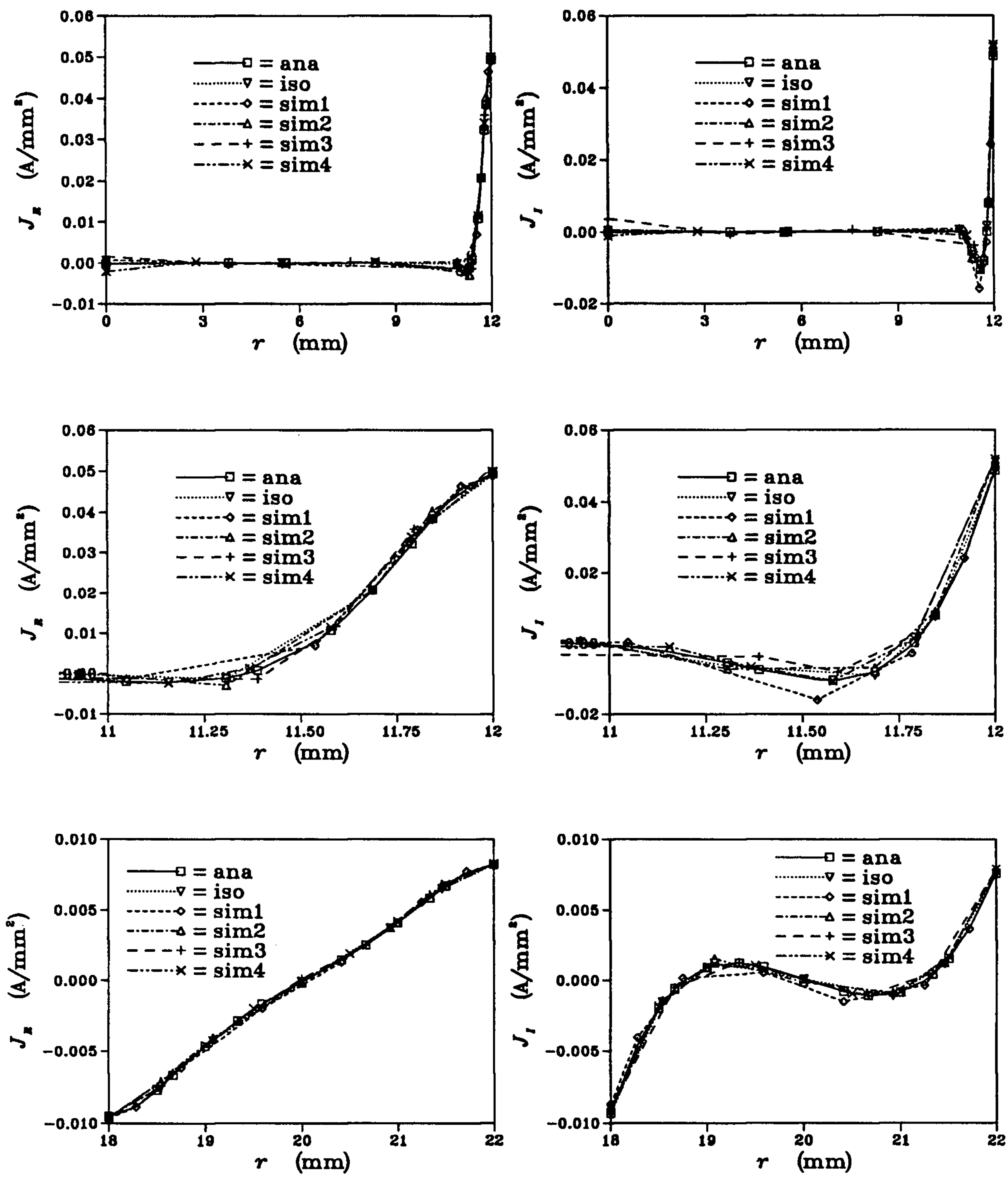

Figure 3.12: Current density distribution in the SC coaxial cable at 60kHz

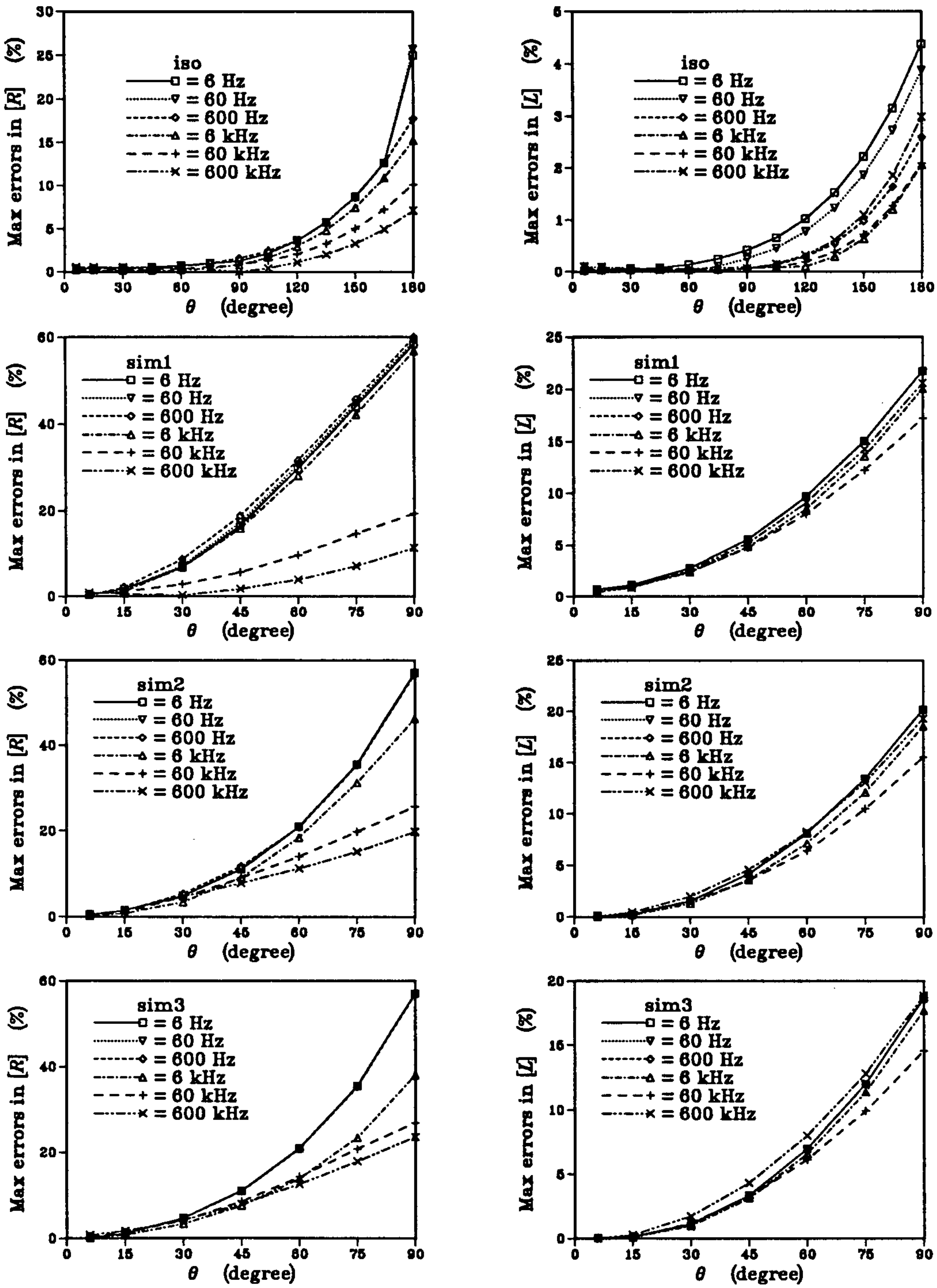

Figure 3.13: Maximum errors in $[R]$ and $[L]$ at different θ

3.6.2 Computation efficiency: CPU time, storage, and pivoting

From the preceding section it is seen that isoparametric elements can have larger θ than simplex elements for the same accuracy. This will certainly reduce the number of elements and number of nodes in the mesh if a whole circular region needs to be meshed. Consequently, CPU time and memory storage will be reduced.

There are other factors affecting the computation efficiency, such as bandwidth (BW) of the final equations depicted in Fig. 3.7, type of algorithm for solving the final equations, and element types.

In order to achieve an overall comparison, a whole circular region is used in the comparison study. When the error limit is given, different element types with different θ are applied to mesh the circular region. Fig. 3.14 gives the meshes of isoparametric and the 2nd order simplex elements at 60kHz with error limit of 2% and 15%, respectively.

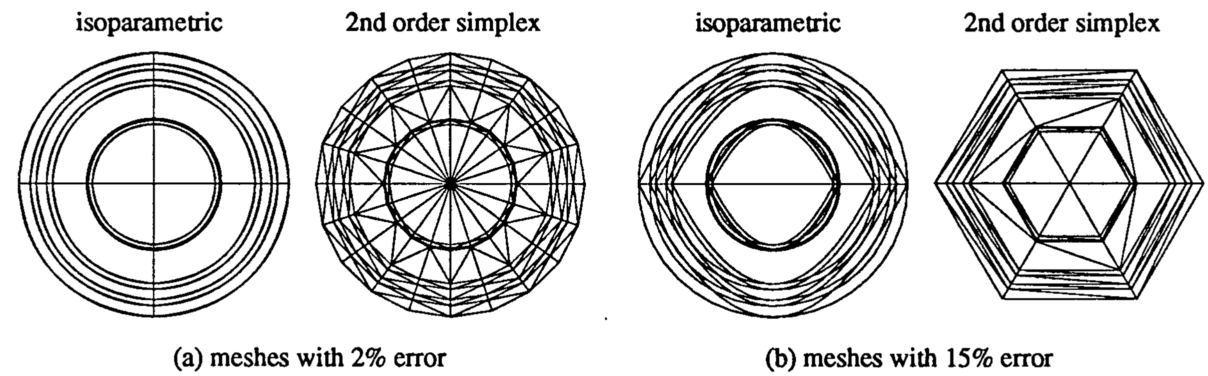

Figure 3.14: FEM meshes at 60kHz for different error limits

In isoparametric element meshes, circles in division radii are also drawn for the purpose of misfit observation. The misfit in the mesh in Fig. 3.14(a) is almost unnoticeable, while it is very large in Fig. 3.14(b). Tab.3.7 lists some of the main computation parameters for different elements and different order of simplex elements at 2% error limit. The final matrix is a complex matrix in double precision. M and N are the number of elements and number of unknown nodes, respectively. Tab.3.8 lists the corresponding CPU time for the calculation. The calculation is done on a VAX 11/750 having a speed of .6 $\sim$ .7 million instructions per second with floating point accelerator. As a variable bandwidth

Table 3.7: Storage and other parameters for different elements

element type	θ (degree)	M	N	BW	matrix dimension	storage (bytes)	Max errors (%)	
							R	L
iso	90	32	89	17	1088×1	83900	0.85	0.06
sim1	22.5	464	225	20	3666×1	227084	1.87	1.59
sim2	18	300	581	119	28474×1	1372376	1.65	0.52
sim3	18	220	961	206	70636×1	3838008	1.81	0.25
sim4	22.5	176	1377	319	151385×1	7387372	—	—

Table 3.8: CPU time requirements for different elements

element type	matrix formation	matrix factorization	solution	loss-energy method	others	total CPU time
iso	2.4 s (26.0%)	1.8 s (19.5%)	0.5 s (5.4%)	3.2 s (34.3%)	1.4 s (14.8%)	9.3 s
sim1	2.3 s (12.5%)	6.7 s (36.8%)	1.6 s (8.5%)	3.5 s (18.9%)	4.3 s (23.4%)	18.4 s
sim2	4.6 s (2.9%)	130.4 s (82.1%)	10.4 s (6.5%)	7.1 s (4.5%)	6.4 s (4.0%)	158.9 s
sim3	11.0 s (1.9%)	506.7 s (88.9%)	26.7 s (4.7%)	11.9 s (2.1%)	13.9 s (2.4%)	570.2 s

Choleski algorithm was used[15], the final matrix was stored as a one-dimensional array. For the 4th order simplex element the calculation was not completed and the CPU time is not available.

Tab.3.8 shows that the loss-energy method for calculating $[Z]$ from the field solution takes a substantial amount of CPU time. The results, however, are the same as those from the J_S method (up to eight digits), which takes negligible time. The agreement between these two methods exists in all the $[Z]$ calculation of the SC cable.

The variable bandwidth Choleski algorithm is modified from the one applied to real matrices. It takes advantage of the symmetry and sparsity of the matrix. However, it does not select a pivotal element when factorizing the matrix. Partial pivoting was also used in the solutions, and the results were the same as those without pivoting. The CPU time required by the pivoting algorithm is much higher, and the corresponding CPU time and storage requirements are listed in Tab.3.9.

Table 3.9: Storage and CPU time requirements for pivoting

element type	matrix dimension	storage (bytes)	CPU time	
			factorization	solution
iso	49×89	136268	2.8 s	0.7 s
sim1	58×225	377228	10.7 s	2.2 s
sim2	355×581	4216872	403.9 s	28.9 s
sim3	616×961	12179448	1703.7 s	103.1 s
sim4	955×1377	26005772	—	—

For 15% error limit, similar comparisons are given in Tab.3.10 to Tab.3.12. A Pivoting algorithm again gives the same results as the variable bandwidth Choleski algorithm. In

Table 3.10: Storage and other parameters for different elements

element type	θ (degree)	M	N	BW	matrix dimension	storage (bytes)	Max errors (%)	
							R	L
iso	180	16	45	9	303×1	33928	10.10	2.09
sim1	60	174	85	9	611×1	55604	9.75	8.06
sim2	60	90	175	29	3158×1	170384	14.06	6.45
sim3	60	66	289	61	9628×1	454104	14.30	6.14
sim4	60	66	517	105	27845×1	1230332	14.14	5.81
sim5	60	54	661	161	50056×1	2214940	13.70	5.59
sim6	60	54	955	229	99610×1	4335336	13.43	5.35

this case the loss-energy method gives faulty results with isoparametric elements. The reason is that the two centre triangular isoparametric elements in Fig. 3.14(b) have 180° as their vertex angles.

Based on the above comparisons isoparametric elements are more efficient than simplex elements with respect to CPU time and memory storage within the same error limit.

Table 3.11: CPU time requirements for different elements

element type	matrix formation	matrix factorization	solution	loss-energy method	others	total CPU time
iso	1.2 s (28.2%)	0.5 s (10.6%)	0.2 s (4.6%)	1.7 s (38.7%)	0.8 s (17.8%)	4.4 s
sim1	1.0 s (18.3%)	0.9 s (16.7%)	0.4 s (6.8%)	1.3 s (25.5%)	1.7 s (32.7%)	5.3 s
sim2	1.1 s (8.9%)	6.2 s (48.2%)	1.3 s (10.3%)	2.2 s (17.3%)	2.0 s (15.2%)	12.8 s
sim3	2.1 s (4.5%)	32.7 s (71.9%)	3.7 s (8.2%)	3.7 s (8.2%)	3.3 s (7.2%)	45.5 s
sim4	4.8 s (2.6%)	154.0 s (83.2%)	10.9 s (5.9%)	7.9 s (4.3%)	7.6 s (4.1%)	185.2 s
sim5	8.6 s (2.0%)	367.5 s (87.1%)	18.4 s (4.4%)	11.1 s (2.6%)	16.1 s (3.8%)	421.7 s
sim6	17.2 s (1.5%)	1017.2 s (90.0%)	39.7 s (3.5%)	19.9 s (1.8%)	36.8 s (3.3%)	1130.8 s

Table 3.12: Storage and CPU time requirements for pivoting

element type	matrix dimension	storage (bytes)	CPU time	
			factorization	solution
iso	25×45	47080	0.6 s	0.3 s
sim1	25×85	79828	1.1 s	0.5 s
sim2	85×175	357856	11.8 s	2.2 s
sim3	181×289	1137000	66.9 s	6.6 s
sim4	313×517	3373948	333.0 s	23.1 s
sim5	481×661	6501100	897.6 s	44.1 s
sim6	685×955	13208376	2569.4 s	117.3 s

3.7 Summary

In this chapter shape functions are discussed for high-order simplex elements and for quadratic isoparametric elements. The integral matrices $[Q^{(1)}]$ and $[T_S]$ of the 5th and 6th order simplex elements are given in the exact integer form. This supplements the tables given in [7]. The general procedure for $[Z]$ calculations with FEM is also discussed.

$[Z]$ of a two-conductor SC coaxial cable is calculated by FEM with both simplex elements and isoparametric elements. Division factors for meshing SC cables are obtained through numerical tests. The results show that isoparametric elements are more efficient in the $[Z]$ calculation of SC coaxial cables than simplex elements. Under the same error limit isoparametric elements can have larger span angles; consequently, the FEM mesh has fewer elements and nodes. For large span angles the accuracy cannot be improved by increasing the order of the simplex elements. The results also show that the loss-energy method discussed in Section 2.5.2 takes a large amount of CPU time and gives the same results (up to eight digits) as the J_S method. In solving the final symmetric banded complex equations the partial pivotal element selection algorithm gives the same solutions as the variable bandwidth Choleski algorithm.

Chapter 4

Earth Region Reduction Technique for $[Z]$ Calculation with FEM

4.1 Introduction

Power cables may be buried directly in the earth or installed in ducts or tunnels underneath the earth surface. Being a conductor itself, the earth often serves as a return path for the unbalanced currents in the cable system. Undoubtedly, the earth has to be included in the parameter calculation of underground power cables.

The earth is generally represented as a uniform half space imperfect conductor for the parameter calculation of underground cables. With this assumption a formula for the impedance of a shallowly buried SC coaxial cable can be derived from the field distribution of a buried current filament by applying the perturbation concept. It is uncertain, however, whether this formula can be applied to other systems with different structures, such as tunnel installed cable systems. It is also uncertain where the perturbation concept becomes invalid as the earth penetration depth becomes smaller and smaller.

The above uncertainties can be studied by FEM. Because the earth region extends to infinity, it is impossible for FEM to solve the field in the whole region. Fortunately, the earth never appears as an independent conductor, and it always exists as a reference conductor in the cable system. Consequently, the field to be calculated in the earth is always created by a loop current between one of the conductors in the cable system and the earth, and is concentrated around the cable system. Therefore, a boundary can be set up in the earth for FEM at a location sufficiently far away from the cable, where the field becomes negligible, and FEM can then be used to calculate the parameters of the cable system together with the earth. Such a boundary is referred to as a field truncation boundary, and FEM with such a boundary shall be called "conventional FEM" here.

With the help of the penetration depth, the field truncation boundary for FEM can easily be established. In the earth the penetration depth can be very large in the low frequency range due to the poor conductivity of the earth. As a result, the FEM solution region becomes very large. More elements are needed to mesh such a solution region, and the computation time will increase. This is a weak point for the conventional FEM with the field truncation boundary.

There are several techniques for FEM to handle problems with infinitely large regions. Among them are the ballooning technique and the singular element technique. The ballooning technique can handle problems with regions of known Green's functions[45], but may be difficult to apply to the earth impedance calculation. The singular element technique assumes an approximate function representing the decay pattern of the field and creates infinitely long element sides to cover the infinitely large region by using singular shape functions. It is difficult to find suitable decay functions for this technique, although it is possible in principle to apply it to cable systems.

In this chapter, a technique is proposed to reduce the earth region when the earth penetration depth is large. It is based on the same perturbation concept used to derive the impedance formulas of directly buried SC coaxial cables from the field solution of a current filament. The boundary established by this technique has non-zero values, while the conventional field truncation boundary has zero values. The non-zero boundary values and the earth return current surrounded by such a boundary are calculated from the field solution of the equivalent current filament. The proposed technique creates a much smaller fixed solution region, and computation time can be saved if the earth return current is calculated only once. It is much easier to mesh a small region than a very large one.

For a deeply buried SC coaxial cable, the earth can be assumed to occupy the whole space, and the field in the earth can be solved theoretically. Therefore, such a cable is used first to study the division schemes and the locations of the field truncation boundary in the earth for the conventional FEM. The impedances of the cable are calculated by the FEM with the field truncation boundary and with the new proposed technique. The results are compared with those of analytical formulas. The comparisons show that the conventional FEM gives accurate results if the field truncation boundary is at a location three times the earth penetration depth away from the cable. For the new proposed technique, the accuracy of results depends on the ratios r_b/δ_e and r_e/δ_e. The parameters r_b and r_e are the boundary radius and inner earth radius, respectively. For r_e=24mm, accurate results can be obtained if $r_b/\delta_e \leq 0.2$.

The impedances of shallowly buried and tunnel installed SC coaxial cables are also calculated with the conventional FEM, as well as with the proposed technique. The numerical results show that $r_b \geq 12\delta_e$ is required for the conventional FEM. Comparisons with the conventional FEM for shallowly buried cables show that Pollaczek's formula gives noticeable errors when the earth penetration is small. The results of a tunnel installed cable show that Pollaczek's formula can also be applied to such a cable by using an approximate r_e if the earth penetration is large.

4.2 Analytical Formulas for $[Z]$ of Buried SC Coaxial Cables

For shallowly buried SC coaxial cables approximate formulas for the $[Z]$ calculation can be derived from the field solution of an equivalent current filament by applying the perturbation concept. For deeply buried SC coaxial cables, the earth can be assumed to occupy the whole space, and the corresponding fields become axisymmetrical. This leads to analytical formulas.

Fig. 4.1(a) shows a shallowly buried SC coaxial cable. In order to calculate $[Z]$ of the cable, the field distribution in the earth has to be found. The impedance formulas can be derived from the E value on the inner surface of the earth, on which point P sits as shown in Fig. 4.1(a). The earth always serves as a return path for the current unbalance in the cable, and the field inside the earth is caused by a loop current between the cable and the earth. This loop current is the sum of all the conductor currents in the cable.

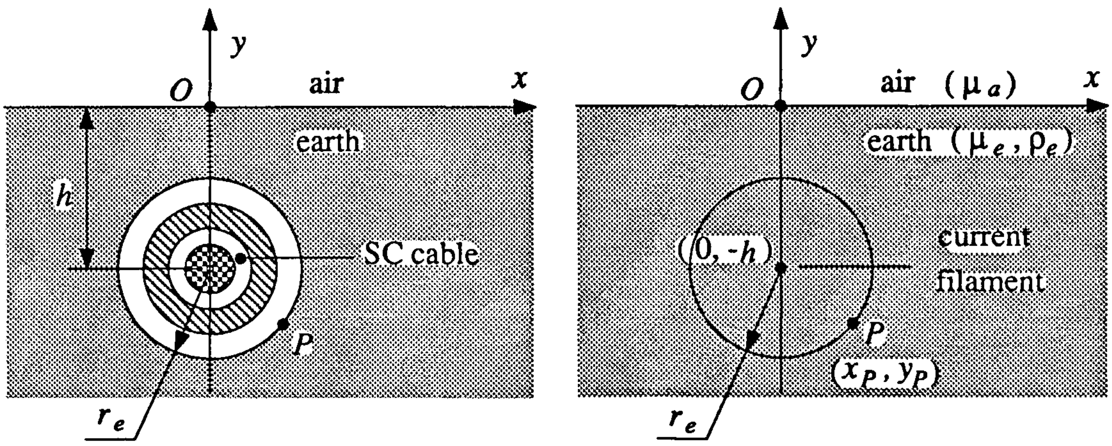

(a) real structure (b) equivalent current filament

Figure 4.1: A shallowly buried SC coaxial cable

No formula exists for finding the field distribution in the earth caused by the above loop current if the actual geometry of the cable is considered. To overcome this difficulty, an equivalent current filament shown in Fig. 4.1(b) is used to replace the original cable. The filament is located at the centre of the cable and is insulated from the earth. If the earth is assumed to be uniform in half space, with its surface being parallel to the buried current filament, the field distribution in the earth caused by the loop current between the filament and the earth can be solved analytically. Such field solutions were first given by Pollaczek [2] and later by Wedepohl *et al*[10].

Applying the assumptions made in Section 2.2 to the structure in Fig. 4.1(b), with

x-y axes as shown in the figure, the E field distributions are [2][10]

$$E_a = -\frac{j\omega\mu_a I}{\pi}\int_0^\infty \frac{e^{-y\alpha-h\sqrt{\alpha^2+1/p_e^2}}}{\alpha+\frac{\mu_a}{\mu_e}\sqrt{\alpha^2+1/p_e^2}}\cos(x\alpha)d\alpha \qquad y\geq 0 \tag{4.1}$$

$$E_e = -\frac{j\omega\mu_e I}{2\pi}\left(\mathrm{K}_0\left(\frac{D}{p_e}\right)-\mathrm{K}_0\left(\frac{D'}{p_e}\right)+\int_0^\infty \frac{2e^{(y-h)\sqrt{\alpha^2+1/p_e^2}}}{\frac{\mu_e}{\mu_a}\alpha+\sqrt{\alpha^2+1/p_e^2}}\cos(x\alpha)d\alpha\right) \qquad y\leq 0 \tag{4.2}$$

where

$$D = \sqrt{x^2+(y+h)^2} \tag{4.3}$$

$$D' = \sqrt{x^2+(y-h)^2} \tag{4.4}$$

$$p_e = \sqrt{\frac{\rho_e}{j\omega\mu_e}} \tag{4.5}$$

E_a and E_e are the E fields in the air and in the earth, respectively, and their detailed derivations are given in Appendix B. h is the burial depth of the cable. I is the current in the filament. p_e is the complex penetration depth in the earth. K_0 is the zero order second kind modified Bessel function. μ_a is the permeability of the air. μ_e and ρ_e are, respectively, the permeability and the resistivity of the earth.

The penetration depth in a conductor is a measure of the field attenuation in the conductor. It can be used to approximately find the region within which the most significant part of the field exists. For convenience, real penetration depth δ defined in (3.45) is often used which relates to p through $\delta=\sqrt{2}|p|$. Because the earth is a poor conductor, its penetration depth will be quite large, especially in the low frequency range. With $\mu_e = \mu_0$ and typical value of $\rho_e = 100\Omega$m for the earth, the real penetration depth in the earth δ_e is 5033 m at 1 Hz and 5.03 m at 1 MHz.

Based on the perturbation concept, the impedance formulas for shallowly buried SC coaxial cables can be derived from (4.2). Considering the large differences between the earth penetration depth and the dimensions of the cable structure, it is assumed that the field of the current filament in Fig. 4.1(b) would not be disturbed significantly if the filament were replaced by the original SC coaxial cable in Fig. 4.1(a). Therefore, $E_e(x_P, y_P)$, the E value at point P on the inner surface of the earth as shown in Fig. 4.1(a), can be calculated approximately from (4.2). The surface impedance at point P is defined as

$$\begin{aligned} Z_e &= -\frac{E_e(x_P, y_P)}{I} \\ &= -\frac{j\omega\mu_e}{2\pi}\left(\mathrm{K}_0\left(\frac{\sqrt{x_P^2+(y_P+h)^2}}{p_e}\right) - \mathrm{K}_0\left(\frac{\sqrt{x_P^2+(y_P-h)^2}}{p_e}\right) + \right. \\ &\quad \left. + \int_0^\infty \frac{2e^{(y_P-h)\sqrt{\alpha^2+1/p_e^2}}}{\frac{\mu_e}{\mu_a}\alpha + \sqrt{\alpha^2+1/p_e^2}} \cos(x_P\alpha)d\alpha\right) \end{aligned} \tag{4.6}$$

Strictly speaking, Z_e would be different at different locations on the inner surface of the earth. The differences, however, are very small, and can be ignored. If $x_P = r_e$ and $y_P = -h$, (4.6) becomes

$$Z_e = -\frac{j\omega\mu_e}{2\pi}\left(\mathrm{K}_0\left(\frac{r_e}{p_e}\right) - \mathrm{K}_0\left(\frac{\sqrt{r_e^2+4h^2}}{p_e}\right) + \int_0^\infty \frac{2e^{-2h\sqrt{\alpha^2+1/p_e^2}}}{\frac{\mu_e}{\mu_a}\alpha + \sqrt{\alpha^2+1/p_e^2}} \cos(r_e\alpha)d\alpha\right) \tag{4.7}$$

r_e is the inner surface radius of the earth. Z_e is also called "earth return impedance." Equation (4.7) was first derived by Pollaczek, and shall be called "Pollaczek's formula."

Once Z_e is known, $[Z]$ of a buried SC coaxial cable can be calculated with (2.68), except that Z_{EQ_K} in (2.72) has to be modified into

$$Z_{EQ_K} = Z_{B_K} + Z_{D_K} + Z_e \tag{4.8}$$

Z_e in (4.7) can be found by numerical integration. It should be noted from (2.69) and (2.70) that every element in matrix (2.68) has Z_{EQ_K} as one of its components. Therefore, Z_e must be added to every element in $[Z]$ of a SC coaxial cable.

If a SC coaxial cable is buried deeply in the earth ($h \gg \delta_e$), the earth can be assumed to occupy the whole space, and the field becomes axisymmetrical again. For such a case the earth becomes a coaxial conductor with infinite outer radius, and its inner surface impedance will be derived from (2.65) by letting $r_{B_k} \longrightarrow \infty$ and $r_{A_k} = r_e$. The resulting formula is

$$Z_e = \frac{\sqrt{j\omega\mu_e\rho_e}}{2\pi r_e}\frac{\mathrm{K}_0\left(r_e/p_e\right)}{\mathrm{K}_1\left(r_e/p_e\right)} \tag{4.9}$$

r_e is the inner surface radius of the earth. The above equation is to be used in (4.8) together with (2.68) to calculate $[Z]$ of deeply buried SC coaxial cables.

There are some uncertainties when applying the above formulas to the $[Z]$ calculation of practical underground cable systems. For example, for the tunnel installed SC coaxial cable shown in Fig. 1.1, (4.7) cannot be applied directly because r_e does not exist. Also, it is not clear how the tunnel structure will affect the impedance calculation with respect to the insulation within the tunnel. Similarly, Z_e for shallowly buried SC coaxial cables is derived by using an approximation with the perturbation concept, and it is uncertain when this concept is no longer applicable. These uncertainties can be studied numerically with FEM.

Before FEM is applied to the $[Z]$ calculation of a general underground cable system, it is first applied to the $[Z]$ calculation of a deeply buried SC coaxial cable, where the field can be found analytically. This case is used to study the division schemes in the earth and the locations of the field truncation boundary for FEM. It is also used to develop a new technique for reducing the earth region in FEM solutions in Section 4.4.

4.3 [Z] Calculation of Deeply Buried SC Coaxial Cables by Conventional FEM with a Field Truncation Boundary

It is assumed that the two-conductor SC coaxial cable in Fig. 3.9(a) is buried deeply in the earth as shown in Fig. 4.2(a). To calculate [Z] of the cable numerically by conventional FEM, a field truncation boundary located at r_b shown in Fig. 4.2(b) has to be established, which should enclose the most significant part of the field distribution. Because the earth is a very poor conductor, the division scheme for conductors discussed

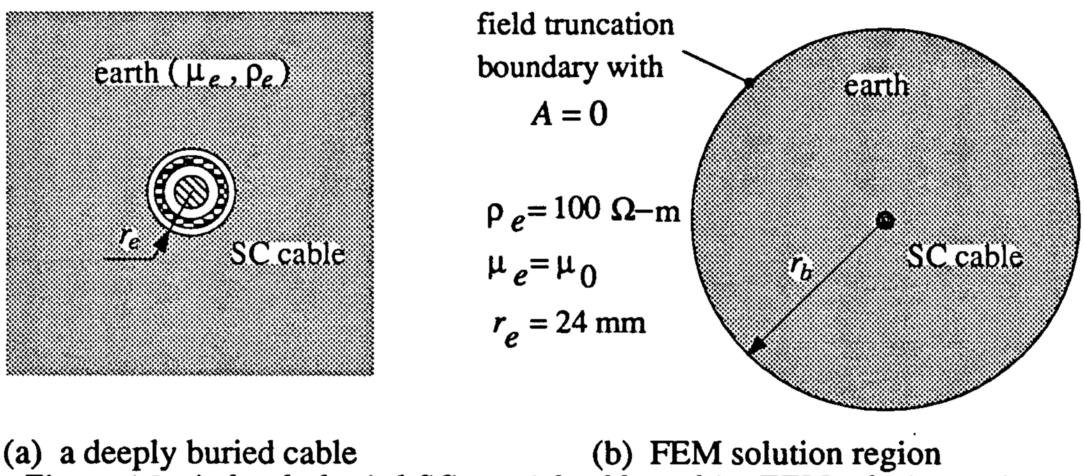

Figure 4.2: A deeply buried SC coaxial cable and its FEM solution region

in Section 3.6 is not applicable to the earth, and new division schemes need to be found. Two questions to be answered in this section are therefore: where to locate the field truncation boundary and how to mesh the earth.

For the system in Fig. 4.2(a) [Z] can be calculated analytically. Therefore, the numerical results from FEM can always be checked by comparing them with those from analytical formulas.

As the earth serves as a return path or as a reference conductor, the general FEM solution procedure discussed in Section 3.5 needs to be modified slightly. Assuming a system has $K+1$ conductors with the reference conductor being conductor $K+1$, [Z] will be a $K \times K$ matrix. To calculate the jth column of $[Z]$, a loop current I_j between the jth conductor and the reference conductor is used to excite the field. The jth element and the $(K+1)$th element of $[I]$ in (3.37) will be I_j and $-I_j$, respectively. Once the field is solved the elements in the jth column of $[Z]$ are given by the following formula with the J_S method

$$Z_{ij} = \frac{1}{I_j}(J_{S_i}/\sigma_i - J_{S_{K+1}}/\sigma_{K+1}) \qquad (i = 1, 2, \dots, K) \tag{4.10}$$

where J_{S_i} and $J_{S_{K+1}}$ are the source current densities in the ith and the reference conductors, respectively. σ_i and σ_{K+1} are the conductivities in the ith and the reference conductors, respectively. With the loss-energy method, $[Z]$ is given by

$$R_{ij} = \left\{ \sum_{k=1}^{K+1} \int_{S_{C_k}} \frac{J_{(ki)} J^*_{(kj)}}{\sigma} ds \right\} / (I_{R_i} I_{R_j} + I_{I_i} I_{I_j}) \qquad (i, j = 1, 2, \dots, K) \tag{4.11}$$

$$L_{ij} = \left\{ \sum_{k=1}^{K+1} \mathbf{Re} \left(\int_{S_{C_k}} A_{(ki)} J^*_{(kj)} ds \right) \right\} / (I_{R_i} I_{R_j} + I_{I_i} I_{I_j}) \quad (i, j = 1, 2, \dots, K) \tag{4.12}$$

where $J_{(ki)}$ and $A_{(ki)}$ are, respectively, the current density distribution and magnetic vector potential distribution caused by I_i, the loop current between the ith conductor and the reference conductor. For both methods the system has to be solved K times.

To locate the optimum boundary is to find the minimum r_b. For the system in Fig. 4.2 the earth current enclosed by r_b can be calculated analytically. If a loop current of $1+j0$ A is assumed between the cable and the earth, with typical resistivity and permeability values as shown in Fig. 4.2(b), the earth return current I_e from the analytical formula is shown in Fig. 4.3(a), as a function of r_b at 6kHz. δ_e is 64.97m at this frequency. Similar curves can be obtained for other frequencies. It can be seen that $I_{e_R} \approx 1$ A and $I_{e_I} \approx 0$ at $5\delta_e$. This means that the most significant part of the field is enclosed by a boundary at $5\delta_e$ for the deeply buried SC coaxial cable.

FEM is applied to calculate $[Z]$ of the system in Fig. 4.2 for different r_b. Isoparametric elements are used in the calculation, and the solution region is reduced to a wedged region

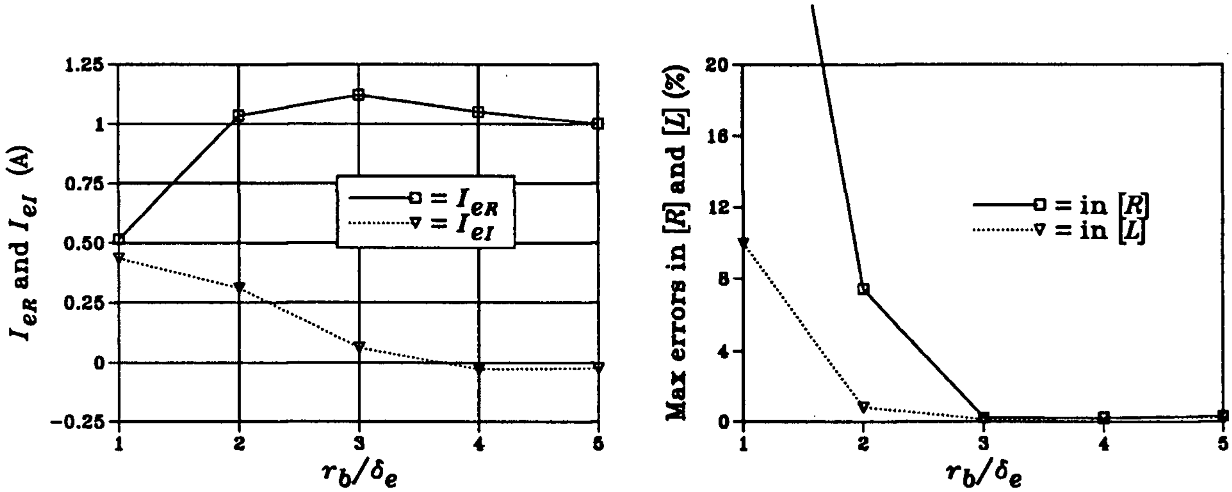

(a) enclosed earth current by r_b at 6kHz (b) max errors in $[R]$ and $[L]$

Figure 4.3: Earth return current and maximum errors in $[Z]$ for different r_b

similar to the one in Fig. 3.9(b) with $\theta = 6^o$ due to axial symmetry. Six frequencies are used: 6Hz, 60Hz, 600Hz, 6kHz, 60kHz, and 600kHz. To mesh the solution region, the division radii listed in Tab.3.5 are used for meshing the conductors, while the division pattern $10^n, 10^{n+\frac{1}{3}}, 10^{n+\frac{2}{3}}, 10^{n+1}$ discussed later in this section is used for meshing the earth. The maximum errors in R and L are plotted in Fig. 4.3(b). These maximum errors are selected from the errors in all the six elements of $[R]$ or $[L]$ at all the six frequencies. The figure shows that accurate results can be obtained for the deeply buried SC coaxial cable when r_b=$3\delta_e$.

For the same system, ρ_e is varied from 1000Ωm to 0.01Ωm, and the results show that the maximum errors in R and L always decrease to less than one percent when r_b=$3\delta_e$. Therefore, for $[Z]$ calculations of deeply buried SC coaxial cables, $3\delta_e$ can be used as the location of a field truncation boundary for the conventional FEM.

The optimum division in the earth means that the corresponding FEM mesh should achieve accurate results with the least possible number of elements and nodes. Due to the large difference between the size of the cable and the size of the earth region, it is impossible to have similar element sizes everywhere in the whole region. The general practice is to use element sizes similar to those in the cable to mesh the areas in the earth region next to the cable. When meshing the areas in the earth region away from the cable, the element sizes will be increased gradually to the boundary at r_b.

Several division radius patterns are tried out for isoparametric elements with different earth resistivities. These patterns use several division radii in each decade from 10^n to 10^{n+1}. These patterns are listed in Tab.4.1. The first earth division radius is r_e and the last one is $r_b=3\delta_e$. Between r_e and r_b, the earth is divided by division radii listed in Tab.4.1.

Table 4.1: Earth division radius patterns for isoparametric elements in the decade from 10^n to 10^{n+1}

pattern	division radii			
1	10^n	$10^{n+\frac{1}{3}}$	$10^{n+\frac{2}{3}}$	10^{n+1}
2	10^n	$10^{n+\frac{1}{2}}$	10^{n+1}	
3	10^n	$\frac{1}{3}\times 10^{n+1}$	$\frac{2}{3}\times 10^{n+1}$	10^{n+1}
4	10^n	$\frac{1}{2}\times 10^{n+1}$	10^{n+1}	
5	10^n	10^{n+1}		

The numerical results show that the first pattern in Tab.4.1 always achieves high accuracy. For the system in Fig. 4.2, the division radii in the earth given by this pattern at different frequencies are listed in Tab.4.2, and the resistances and inductances calculated

Table 4.2: Earth division radii for isoparametric elements

f (Hz)	division radii (m)								
6	0.024	0.0464	0.1	0.215	0.464	1	2.15	4.64	10	21.5
	46.4	100	215	464	1000	2150	4640	6164		
60	0.024	0.0464	0.1	0.215	0.464	1	2.15	4.64	10	21.5
	46.4	100	215	464	1000	1949				
600	0.024	0.0464	0.1	0.215	0.464	1	2.15	4.64	10	21.5
	46.4	100	215	464	616					
6000	0.024	0.0464	0.1	0.215	0.464	1	2.15	4.64	10	21.5
	46.4	100	195							
60000	0.024	0.0464	0.1	0.215	0.464	1	2.15	4.64	10	21.5
	46.4	61.6								
600000	0.024	0.0464	0.1	0.215	0.464	1	2.15	4.64	10	19.5

from the corresponding meshes are given in Tab.4.3, together with the values calculated by the analytical formulas. The solution region has $\theta = 6^o$.

Table 4.3: $[R]$ and $[L]$ of the deeply buried SC coaxial cable

f (Hz)	element	R (Ω/km)			L (mH/km)		
		R_{11}	R_{12}	R_{22}	L_{11}	L_{12}	L_{22}
6	ana	0.0447332	0.0059220	0.420388	2.41400	2.26152	2.25486
	iso	0.0447221	0.0059109	0.420377	2.41099	2.25853	2.25188
60	ana	0.100918	0.0592392	0.473695	2.18191	2.03126	2.02461
	iso	0.100821	0.0591056	0.473561	2.17968	2.02884	2.02219
600	ana	0.692750	0.594334	1.00774	1.92586	1.80098	1.79434
	iso	0.691494	0.593213	1.00662	1.92364	1.79882	1.79218
6000	ana	6.60507	6.11239	6.43395	1.67654	1.56891	1.56320
	iso	6.59130	6.09938	6.42073	1.67495	1.56733	1.56162
60000	ana	63.7665	60.9211	60.8546	1.41446	1.32596	1.32602
	iso	63.6482	60.8077	60.7478	1.41308	1.32461	1.32469
600000	ana	605.816	596.942	596.942	1.17633	1.09287	1.09287
	iso	604.401	595.578	595.578	1.17555	1.09210	1.09210

The first pattern is also tested with different earth resistivities and with different r_e, and the results show that overall errors in the frequency range from 0 to 1MHz for all the elements in $[R]$ and $[L]$ are less than 1%. The resistivities used in the study are 1000Ωm, 10Ωm, 1Ωm, 0.1Ωm, and 0.01Ωm, with the other parameters remaining the same. r_e is varied among the values: 50mm, 100mm, 250mm, 500mm, and 1000mm with ρ_e=100Ωm, while the other parameters remain the same. When r_e is larger than 50mm, additional division radii are needed for the insulation between the outer conductor of the cable and the earth. The first pattern listed in Tab.4.1 emerges as a good choice in meshing the insulation.

If a unit loop current is assumed for the system in Fig. 4.2 between the inner conductor of the cable and the earth, the corresponding J distributions in the earth calculated by FEM at different frequencies are shown in Fig. 4.4. The analytical J distributions in the earth are also plotted in the figure. Good agreements between the numerical solutions and the analytical solutions can be observed from the curves in the figure. The J distributions

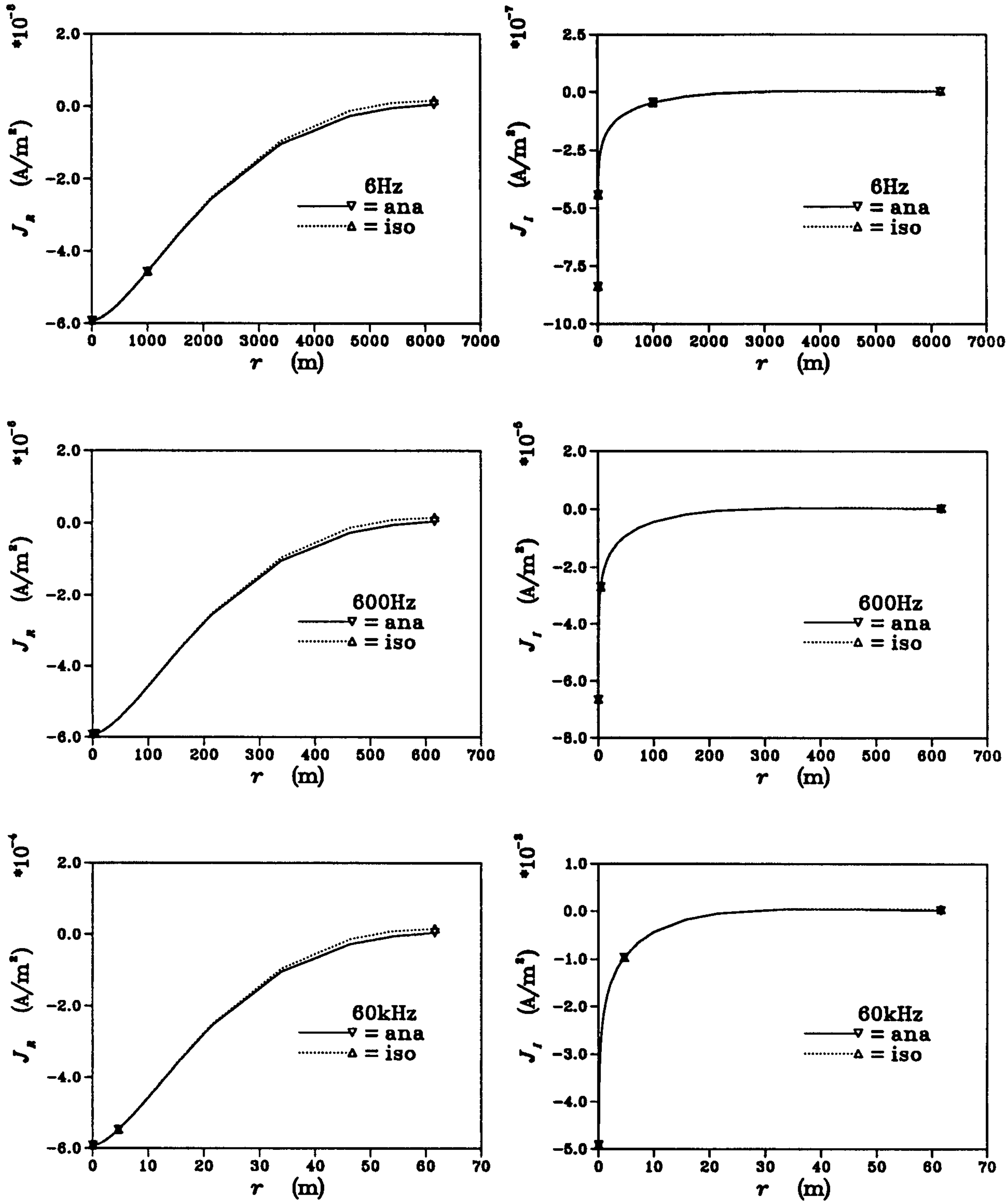

Figure 4.4: J distributions in the earth at different frequencies

in the conductors of the cable at corresponding frequencies remain almost the same as those plotted in Fig. 3.11 and Fig. 3.12 because both cases have the same conductor currents and the same conductor division radii.

The results also show that the errors in $[Z]$ are directly proportional to the errors in J on the inner surface of the earth. By definition the earth return impedance for a deeply buried SC coaxial cable is obtained by dividing the inner surface E of the earth by the earth current. Therefore, errors in the inner surface J of the earth will be directly reflected in the earth return impedance.

In meshing the solution region of the system in Fig. 4.2, different angles θ are used for the isoparametric elements and for the second order simplex elements. Based on the results at six frequencies (6Hz, 60Hz, 600Hz, 6kHz, 60kHz, and 600kHz), the overall errors with isoparametric elements at $\theta = 90^{\circ}$ are approximately 1.2% for R and 0.2% for L. The same accuracy can only be achieved with the second order simplex element at $\theta = 15^{\circ}$.

The J_S and the loss-energy methods for calculating $[Z]$ from the field solutions always give the same results (identical to 8 digits) for all cases used in this section.

It can be concluded from the results presented in this section that the impedances of deeply buried SC coaxial cables calculated by FEM with a field truncation boundary are sufficiently accurate provided that the boundary is at least $3\delta_e$ away from the cables and that the earth is meshed properly. This can serve as a guideline for choosing the field truncation boundaries of other types of underground cable systems where analytical solutions are not available for comparison purpose.

Though the earth division pattern $10^n, 10^{n+\frac{1}{3}}, 10^{n+\frac{2}{3}}, 10^{n+1}$ gives accurate results, the number of elements in the earth is quite large, especially in the low frequency range. This increases computation time. Also, the large difference between the size of the cable and the size of the earth region make it difficult to mesh the whole solution region unless a specific auto-mesh program is used. It is therefore worthwhile to search for ways of reducing the earth solution region. One such technique is proposed in the next section.

4.4 Earth Reduction Technique

In Section 4.2 the formulas for a shallowly buried SC coaxial cable are derived with two approximations: the cable structure will not disturb the field distribution of an equivalent filament current located at the centre of the cable, and the field inside the inner surface of the earth is still axisymmetrical. The second approximation ignores the influence of the earth on the field inside the SC coaxial cable. It also ignores the differences among the E values at different points on the inner surface of the earth.

These two approximations can be removed by applying FEM with field truncation boundary. Therefore, the influences of these approximations for shallowly buried SC coaxial cables can be studied. The method can also be used for underground cable systems with arbitrary structures, such as the tunnel installed SC coaxial cables shown in Fig. 1.1.

From the discussions and results in the preceding section, it is clear that the conventional FEM requires an earth solution region which is very large compared with the dimension of the cables. This increases computation time and creates problems for general auto-mesh programs in meshing such a large region as well as the details around the cable. To overcome these problems, a technique based on the perturbation concept is proposed to reduce the earth solution region.

If the earth penetration depth is much larger than the cable structure, the structure will only slightly disturb the field of a buried current filament located at the centre of the cable. Therefore, a small solution region can be used for FEM with non-zero boundary values and with partial earth return current enclosed by the boundary. The boundary values and the partial earth return current are calculated approximately from the E field solution of the filament. The E field solution of a deeply buried current filament can be derived analytically, while that of a shallowly buried current filament has been derived by Pollaczek[2] and Wedepohl *et al*[10].

In general, the boundary is set up at a distance which is large compared with the dimension of the cable structure. The resulting boundary will then only be located in the earth and the air. Assuming that E_b and A_b stand for the E and A values on the reduced boundary, respectively, the following equations are used in the solutions

$$A_b = -\frac{E_b}{j\omega} \qquad \text{in air} \tag{4.13}$$

$$A_b = -\frac{E_b}{j\omega} + \frac{1}{j\omega\sigma_e} J_S \qquad \text{in earth} \tag{4.14}$$

where J_S and σ_e are the source current density and conductivity in the earth, respectively. E_b is given by filament formulas and is proportional to the filament current. For a system of $K+1$ conductors with conductor $K+1$ as the reference conductor, if $[E_B]$ are the E_b values of boundary nodes in the FEM mesh, $[A_B]$ in (3.35) will become

$$[A_B] = -\frac{[E_B]}{j\omega} + \frac{[\mathbf{1}_V] J_{S_{K+1}}}{j\omega\sigma_{K+1}} \tag{4.15}$$

where $[\mathbf{1}_V]$ is a vector with N_B elements. If the boundary nodes are numbered such that the first N_{B_E} nodes are the boundary nodes in the earth, and the remaining $N_B - N_{B_E}$ nodes are in the air, the first N_{B_E} elements in $[\mathbf{1}_V]$ will be unity and the rest of the elements will be zero. $[A_B]$ becomes a partially known vector. $[I_{E_1}]$ and $[I_{E_2}]$ in (3.38) become

$$[I_{E_1}] = -[D_B]\left(-\frac{[E_B]}{j\omega} + \frac{[\mathbf{1}_V] J_{S_{K+1}}}{j\omega\sigma_{K+1}}\right) = [I_{E_3}] - [F_V] J_{S_{K+1}} \tag{4.16}$$

$$[I_{E_2}] = j\omega[G_C][F_B]^T\left(-\frac{[E_B]}{j\omega} + \frac{[\mathbf{1}_V] J_{S_{K+1}}}{j\omega\sigma_{K+1}}\right) = [I_{E_4}] + [S_{C_V}] J_{S_{K+1}} \tag{4.17}$$

where

$$\begin{aligned}
[I_{E_3}] &= [D_B][E_B]/(j\omega) \\
[I_{E_4}] &= -[G_C][F_B]^T[E_B] \\
[F_V] &= [D_B][\mathbf{1}_V]/(j\omega\sigma_{K+1}) \\
[S_{C_V}] &= [G_C][F_B]^T[\mathbf{1}_V]/\sigma_{K+1}
\end{aligned} \tag{4.18}$$

$[F_V]$ and $[S_{C_V}]$ are vectors. Putting $[I_{E_1}]$ and $[I_{E_2}]$ in (4.16) and (4.17) into (3.37) and moving $J_{S_{K+1}}$ terms to the left side produces

$$\begin{bmatrix} [D] & -[F_A] \\ [F_H] & [S_{C_A}] \end{bmatrix} \begin{bmatrix} [A_U] \\ [J_S] \end{bmatrix} = \begin{bmatrix} [I_{E3}] \\ [I] + [I_{E4}] \end{bmatrix} \tag{4.19}$$

$[F]$ becomes $[F_A]$ if $[F_V]$ is subtracted from its last column, and $[S_C]$ becomes $[S_{C_A}]$ if $[S_{C_V}]$ is subtracted from its last column. $[I]$ always corresponds to a loop current. For a loop current I_j between conductor j and the earth, the jth and $(K+1)$th elements in $[I]$ will be I_j and I_{ep}, respectively. I_{ep} is the partial earth return current enclosed by the reduced boundary. Once (4.19) is solved for the loop current, (4.10) will be used to find $[Z]$. The loss-energy method is not applicable here.

Although $[A_B]$ in (4.15) is only partially known due to unknown $J_{S_{K+1}}$ in the earth, the corresponding boundary nodes are still treated as having fixed boundary values. They do not appear in the final equations of the solution as shown by (4.19). Their values will be evaluated by (4.15) after solving for $J_{S_{K+1}}$.

For a deeply buried SC cable, the field solutions of both the original cable and the buried current filament have simple forms. Therefore, the proposed technique is first tested for such a cable. The cable shown in Fig. 4.2(a) is redrawn in Fig. 4.5(a), while the corresponding buried current filament is drawn in Fig. 4.5(b). $E_C(r)$ and $E_F(r)$ in Fig. 4.5 are the E fields associated with the cable and the filament, respectively. They

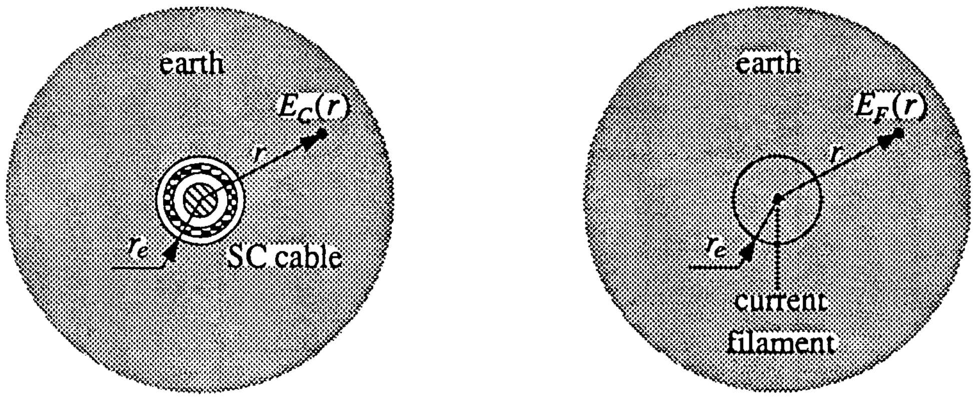

(a) original SC cable (b) current filament replacement

Figure 4.5: Replacing a deeply buried SC cable with a current filament

are given by

$$E_C(r) = -\frac{j\omega\mu_e I}{2\pi}\frac{\mathrm{K}_0(r/p_e)}{(r_e/p_e)\,\mathrm{K}_1(r_e/p_e)} \qquad r \geq r_e \tag{4.20}$$

$$E_F(r) = -\frac{j\omega\mu_e I}{2\pi}\mathrm{K}_0(r/p_e) \qquad r > 0 \tag{4.21}$$

I is the loop current between the cable or the filament and the earth. The partial earth return currents between radii r_e and r for both cases in Fig. 4.5 are

$$I_{ep_C}(r) = -I\left(1 - \frac{r\mathrm{K}_1(r/p_e)}{r_e\mathrm{K}_1(r_e/p_e)}\right) \qquad r \geq r_e \tag{4.22}$$

$$I_{ep_F}(r) = I_F(r) - I_F(r_e) = -\frac{I}{(r_e/p_e)\,\mathrm{K}_1(r_e/p_e)}\left(1 - \frac{r\mathrm{K}_1(r/p_e)}{r_e\mathrm{K}_1(r_e/p_e)}\right) \tag{4.23}$$

where

$$I_F(r) = I_{ep_C}(r)\big|_{r_e\to 0} = -I\left(1 - (r/p_e)\mathrm{K}_1(r/p_e)\right) \tag{4.24}$$

$I_F(r)$ is the earth return current enclosed by radius r with the filament. By defining a perturbation coefficient c_p as

$$c_p = \frac{r_e}{p_e}\mathrm{K}_1\left(\frac{r_e}{p_e}\right) \tag{4.25}$$

$E_C(r)$ and $I_{ep_C}(r)$ can be respectively related to $E_F(r)$ and $I_{ep_F}(r)$ as

$$E_C(r) = E_F(r)/c_p \qquad r \geq r_e \tag{4.26}$$

$$I_{epC}(r) \;=\; c_p I_{epP}(r) \qquad r \geq r_e \tag{4.27}$$

The values of c_p at different $|r_e/p_e|$ are plotted in Fig. 4.6. From Fig. 4.6 it can be seen that c_p is close to 1.0 when the earth penetration is large compared with r_e, since

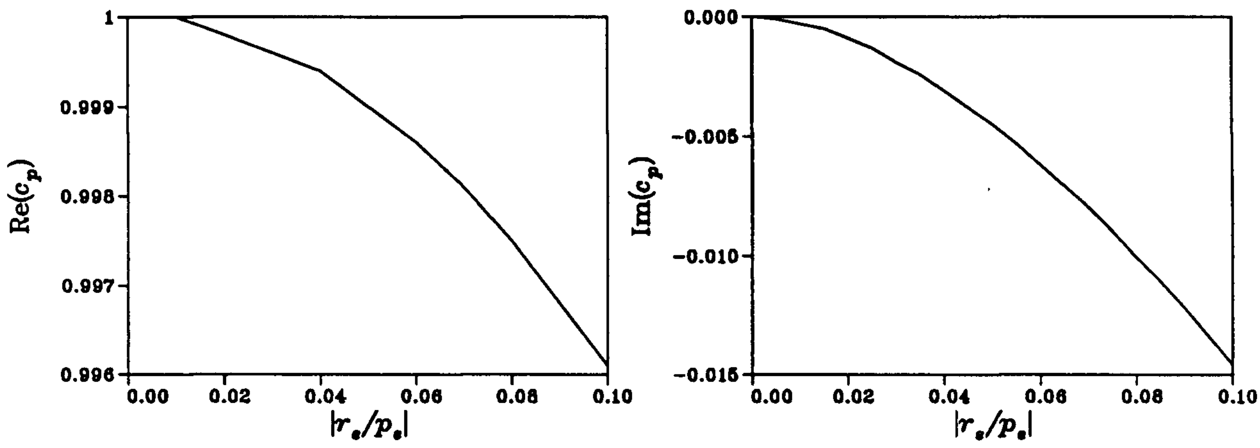

Figure 4.6: Perturbation coefficient c_p as a function of $|r_e/p_e|$

the influence of the cable structure on the field distribution in the earth of the filament becomes negligible in this case. This confirms the basic assumption on which the proposed technique is based. For $|r_e/p_e|$=0.02, f=1MHz, ρ_e=100Ωm, and $\mu_e=\mu_0$, $|p_e|$=3.56m and r_e=71.2mm.

By using the exact formulas in (4.20) and (4.22) to find $[E_B]$ in (4.18) and I_{ep} for $[I]$ in (4.19), $[Z]$ should become reasonably accurate. The impedances of the cable in Fig. 4.2 are calculated with reduced earth regions with exact E_b and I_{ep} for r_b=0.24m, 1m, 2.5m, 10m, and 25m, and the results are listed in Tab.4.4. The results show that accurate $[Z]$ is obtained in the low frequency range where $r_b \ll \delta_e$. When the frequency is high enough such that δ_e becomes comparable to r_b or even smaller than r_b, the final matrix of the equations becomes ill-conditioned, and the results becomes erroneous. This may be due to the fact that $[A_B]$ is an unknown vector for the deeply buried cable although it is treated technically as a known vector.

Different earth resistivities and r_e are tested for the above case with the r_b listed in Tab.4.4, and the numerical results show that the errors are less than 1% in $[R]$ for $r_b < \delta_e$ and in $[L]$ for $r_b < 2\delta_e$. ρ_e is varied among 1000Ωm, 10Ωm, 1Ωm, 0.1Ωm, and 0.01Ωm with r_e=24mm, while r_e is varied among 50mm, 100mm, 250mm, 500mm, 1000mm, and 2000mm with ρ_e=100Ωm.

Table 4.4: $[Z]$ of the deeply buried cable found from a reduced earth region

f (Hz)	r_b (m)	R (Ω/km) R_{11}	R_{12}	R_{22}	L (mH/km) L_{11}	L_{12}	L_{22}
6	ana	0.0447332	0.00592198	0.420388	2.41400	2.26152	2.25486
	0.24	0.0447332	0.00592198	0.420388	2.41323	2.26079	2.25413
	1.00	0.0447332	0.00592200	0.420388	2.41274	2.26028	2.25362
	2.50	0.0447332	0.00592198	0.420388	2.41247	2.26001	2.25336
	10.00	0.0447332	0.00592198	0.420388	2.41191	2.25945	2.25280
	25.00	0.0447332	0.00592198	0.420388	2.41164	2.25918	2.25253
60	ana	0.100918	0.0592392	0.473695	2.18191	2.03126	2.02461
	0.24	0.100954	0.0592391	0.473695	2.18138	2.03055	2.02390
	1.00	0.100955	0.0592392	0.473695	2.18086	2.03002	2.02337
	2.50	0.100955	0.0592393	0.473695	2.18059	2.02975	2.02310
	10.00	0.100955	0.0592391	0.473695	2.18003	2.02920	2.02254
	25.00	0.100955	0.0592392	0.473695	2.17976	2.02892	2.02227
600	ana	0.692750	0.594334	1.00774	1.92586	1.80098	1.79434
	0.24	0.692605	0.594326	1.00773	1.92508	1.80027	1.79362
	1.00	0.692607	0.594326	1.00773	1.92457	1.79975	1.79310
	2.50	0.692607	0.594326	1.00773	1.92430	1.79948	1.79283
	10.00	0.692606	0.594325	1.00773	1.92374	1.79892	1.79228
	25.00	0.692577	0.594295	1.00770	1.92347	1.79865	1.79200
6000	ana	6.60507	6.11239	6.43395	1.67654	1.56891	1.56320
	0.24	6.60474	6.11280	6.43415	1.67583	1.56821	1.56250
	1.00	6.60466	6.11274	6.43409	1.67530	1.56768	1.56197
	2.50	6.60467	6.11275	6.43410	1.67503	1.56741	1.56170
	10.00	6.60393	6.11204	6.43340	1.67448	1.56686	1.56115
	25.00	6.60439	6.11248	6.43383	1.67421	1.56659	1.56088
60000	ana	63.7665	60.9211	60.8546	1.41446	1.32596	1.32602
	0.24	63.7597	60.9191	60.8592	1.41369	1.32523	1.32531
	1.00	63.7593	60.9189	60.8590	1.41317	1.32470	1.32478
	2.50	63.7588	60.9184	60.8585	1.41290	1.32443	1.32451
	10.00	63.7098	60.8736	60.8137	1.41235	1.32388	1.32396
	25.00	63.8667	61.0229	60.9630	1.41131	1.32287	1.32295
600000	ana	605.816	596.942	596.942	1.17633	1.09287	1.09287
	0.24	605.736	596.914	596.914	1.17559	1.09215	1.09215
	1.00	605.711	596.892	596.892	1.17507	1.09163	1.09163
	2.50	605.635	596.826	596.826	1.17480	1.09136	1.09136
	10.00	598.441	590.205	590.205	1.17388	1.09047	1.09047
	25.00	586.913	579.558	579.558	1.18241	1.09834	1.09834

The earth is meshed with the pattern 10^n, $10^{n+\frac{1}{3}}$, $10^{n+\frac{2}{3}}$, 10^{n+1}. The numerical results also show that the impedance errors are sensitive to E_b and I_{ep} and are proportional to the errors in J on the inner surface of the earth.

With the proposed technique, the exact E_b and I_{ep} for the reduced solution region are replaced by the approximate ones from the filament formulas in (4.21) and (4.23). Errors are introduced into E_b and I_{ep} by such a replacement as indicated by (4.26) and (4.27). It has been shown, however, that these errors become negligible if the earth penetration depth is much larger than the cable structure.

The impedances of the cable in Fig. 4.2 calculated with reduced regions with approximate E_b and I_{ep} from the filament field solutions for different r_b are given in Tab.4.5. I_{ep} is calculated by numerical integration based on $E_F(r)$. The FEM solution meshes are used for the numerical integration as well.

With r_e=24mm, the results show a similar pattern as with the exact E_b and I_{ep}: accurate impedances are obtained for the r_b listed in Tab.4.5 if δ_e is much larger than r_b, and erroneous impedances are obtained if δ_e is comparable with r_b. For the r_b listed in Tab.4.5, if the earth resistivity is varied among 1000Ωm, 10Ωm, 1Ωm, 0.1Ωm, and 0.01Ωm with the same r_e, the errors are less than 1% in $[R]$ for $r_b \leq 0.2\delta_e$ and in $[L]$ for $r_b \leq 0.5\delta_e$.

For the same δ_e, the larger the r_e, the larger the ratio r_e/δ_e, and the larger the errors in E_b and I_{ep} given by the filament formulas. Therefore, for a large r_e, the ratio r_e/δ_e has to be less than a certain value in order to achieve accurate results with the proposed technique. By varying r_e among 50mm, 100mm, 250mm, 500mm, 1000mm, and 2000mm with ρ=100Ωm, the results show that the errors are less than 1% in $[R]$ for $r_e/\delta_e \leq 0.012$, and in $[L]$ for $r_e/\delta_e \leq 0.055$.

The frequency range within which the proposed technique achieves high accuracy is mainly determined by the relationship between r_b and δ_e for small r_e, and by the relationship between r_e and δ_e for large r_e. For the cable with ρ=100Ωm, the ratio r_e/δ_e becomes more influential in determining the frequency range if $r_e \geq 250$mm.

Table 4.5: $[Z]$ found with the proposed technique based on E_F

f	r_b	R (Ω/km)			L (mH/km)		
(Hz)	(m)	R_{11}	R_{12}	R_{22}	L_{11}	L_{12}	L_{22}
6	ana	0.0447332	0.00592198	0.420388	2.41400	2.26152	2.25486
	0.24	0.0447332	0.00592197	0.420388	2.41322	2.26079	2.25413
	1.00	0.0447332	0.00592198	0.420388	2.41274	2.26028	2.25362
	2.50	0.0447332	0.00592198	0.420388	2.41247	2.26001	2.25336
	10.00	0.0447332	0.00592198	0.420388	2.41191	2.25945	2.25280
	25.00	0.0447332	0.00592198	0.420388	2.41164	2.25918	2.25253
60	ana	0.100918	0.0592392	0.473695	2.18191	2.03126	2.02461
	0.24	0.100954	0.0592391	0.473695	2.18138	2.03055	2.02390
	1.00	0.100955	0.0592391	0.473695	2.18086	2.03002	2.02337
	2.50	0.100955	0.0592391	0.473695	2.18059	2.02975	2.02310
	10.00	0.100955	0.0592391	0.473695	2.18003	2.02920	2.02254
	25.00	0.100955	0.0592391	0.473695	2.17976	2.02893	2.02227
600	ana	0.692750	0.594334	1.00774	1.92586	1.80098	1.79434
	0.24	0.692605	0.594326	1.00773	1.92508	1.80027	1.79362
	1.00	0.692607	0.594326	1.00773	1.92457	1.79975	1.79310
	2.50	0.692607	0.594326	1.00773	1.92430	1.79948	1.79283
	10.00	0.692606	0.594324	1.00773	1.92374	1.79892	1.79228
	25.00	0.692575	0.594292	1.00770	1.92347	1.79866	1.79201
6000	ana	6.60507	6.11239	6.43395	1.67654	1.56891	1.56320
	0.24	6.60480	6.11285	6.43420	1.67583	1.56821	1.56250
	1.00	6.60470	6.11278	6.43414	1.67530	1.56768	1.56197
	2.50	6.60472	6.11280	6.43415	1.67503	1.56741	1.56170
	10.00	6.60399	6.11210	6.43345	1.67448	1.56686	1.56115
	25.00	6.60443	6.11252	6.43387	1.67421	1.56659	1.56088
60000	ana	63.7665	60.9211	60.8546	1.41446	1.32596	1.32602
	0.24	63.7646	60.9237	60.8638	1.41369	1.32522	1.32530
	1.00	63.7643	60.9235	60.8637	1.41317	1.32470	1.32478
	2.50	63.7633	60.9226	60.8627	1.41290	1.32443	1.32451
	10.00	63.7145	60.8780	60.8181	1.41235	1.32388	1.32396
	25.00	63.8656	61.0218	60.9617	1.41132	1.32287	1.32295
600000	ana	605.816	596.942	596.942	1.17633	1.09287	1.09287
	0.24	606.086	597.237	597.237	1.17556	1.09213	1.09213
	1.00	606.059	597.214	597.214	1.17504	1.09160	1.09160
	2.50	605.980	597.146	597.146	1.17477	1.09133	1.09133
	10.00	598.766	590.504	590.504	1.17386	1.09045	1.09045
	25.00	586.921	579.565	579.566	1.18240	1.09833	1.09833

If r_e=500mm with ρ=100Ωm, the minimum δ_e will be 41.7m, and the corresponding frequency is $f=\rho_e/(\pi\mu_e\delta_e^2)\approx$15kHz. Therefore, the frequency range for the proposed technique is from 1Hz to 15kHz, and r_b is assigned a fixed value, say 2.5m, for this frequency range. For the conventional FEM, $r_b \geq 3\delta_e$ is required for the deeply buried SC cable, and the corresponding r_b for the above frequency range will be from 15,100m to 125m. Thus the proposed technique achieves the goal of reducing the earth solution region in the low frequency range in this case.

4.5 [Z] Calculations of Shallowly Buried SC Coaxial Cables with FEM

In this section the conventional FEM and the proposed technique discussed in the preceding section are applied to the [Z] calculation of shallowly buried SC coaxial cables. The impedances from Pollaczek's formula are compared against those from the FEM for different earth resistivities and for different r_e. The impedances of a SC cable with an arbitrary structure are also calculated with FEM and with Pollaczek's formula.

The numerical results show that for the conventional FEM a solution region with $r_b \geq 12\delta_e$ will give reasonably accurate results. Based on the comparison with the conventional FEM it is shown that accurate results can be obtained with the proposed technique for different ρ_e and r_e. Good agreements are observed among the field distributions around the cable from the conventional method, from the proposed technique, and from the approximate analytical solution. The comparisons between Pollaczek's formula and the FEM show that accurate results are obtained with Pollaczek's formula when r_e/δ_e is small. For r_e=24mm, the maximum differences between the results from Pollaczek's formula and those from the FEM are less than 1% in R if $r_e/\delta_e \leq 0.03$ and in L if $r_e/\delta_e \leq 0.095$. For r_e=1000mm, the maximum differences are less than 1% in R if $r_e/\delta_e \leq 0.018$ and in L if $r_e/\delta_e \leq 0.154$. The numerical results for the cable with an arbitrary structure show that Pollaczek's formula can still be used with an approximate r_e.

4.5.1 Determination of the solution region for the conventional FEM in $[Z]$ calculations of shallowly buried cables

With a shallowly buried SC coaxial cable, there is no exact field solution which could be used as a comparison base. The solution region for the conventional FEM is, therefore, determined by an iterative procedure. The boundary radius r_b will be increased gradually, and the difference between results from two consecutive iterations should become smaller as r_b becomes larger. This difference is used as a criterion in the solution region determination. When the earth penetration is large, Pollaczek's formula (4.7) could also be used as a reference in the solution region determination.

It is assumed that the SC coaxial cable shown in Fig. 3.9 is buried 1.5m beneath the earth surface. Therefore, h=1.5m and r_e=24mm in Fig. 4.1(a). It is also assumed that ρ_e=100Ωm and $\mu_e=\mu_0$. Once r_b is chosen, the earth is divided with the isoparametric elements in the pattern 10^n, $10^{n+\frac{1}{3}}$, $10^{n+\frac{2}{3}}$, 10^{n+1} discussed in Section 4.3. The mesh for $r_b=2\delta_e$ at 6kHz is shown in Fig. 4.7.

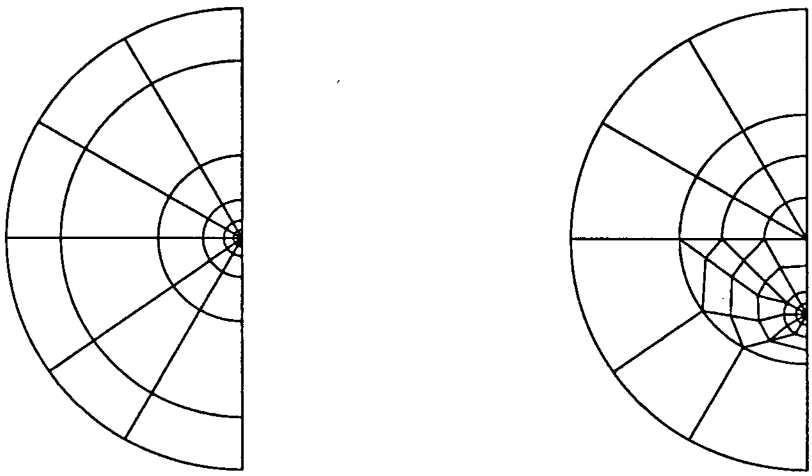

(a) entire mesh (b) detailed mesh around the cable

Figure 4.7: FEM mesh at 6kHz for $r_b=2\delta_e$

The impedances calculated with r_b being equal to $5\delta_e$, $10\delta_e$, and $15\delta_e$, and with

Pollaczek's formula are listed in Tab.4.6. It can be seen that for $[L]$ there is a good agreement between the results from the conventional FEM and from Pollaczek's formula at $r_b=5\delta_e$. For $[R]$ good agreement exists at $r_b=15\delta_e$.

Table 4.6: $[Z]$ of the shallowly buried SC coaxial cable from the conventional FEM

f (Hz)	r_b	R (Ω/km)			L (mH/km)		
		R_{11}	R_{12}	R_{22}	L_{11}	L_{12}	L_{22}
6	$5\delta_e$	0.0445242	0.00570694	0.420238	2.50775	2.35534	2.34869
	$10\delta_e$	0.0446705	0.00585330	0.420384	2.50897	2.35656	2.34990
	$15\delta_e$	0.0447053	0.00588803	0.420419	2.50916	2.35675	2.35010
	Pollaczek	0.0447405	0.00592928	0.420395	2.51380	2.36132	2.35467
60	$5\delta_e$	0.0989151	0.0571899	0.471710	2.27548	2.12469	2.11803
	$10\delta_e$	0.1004902	0.0587650	0.473285	2.27677	2.12598	2.11932
	$15\delta_e$	0.1008098	0.0590845	0.473605	2.27695	2.12615	2.11950
	Pollaczek	0.1011468	0.0594682	0.473924	2.28130	2.13064	2.12399
600	$5\delta_e$	0.677598	0.579357	0.992824	2.01881	1.89399	1.88734
	$10\delta_e$	0.692109	0.593867	1.007335	2.01996	1.89514	1.88849
	$15\delta_e$	0.695547	0.597305	1.010773	2.02014	1.89532	1.88867
	Pollaczek	0.699820	0.601403	1.014809	2.02392	1.89904	1.89240
6000	$5\delta_e$	6.59260	6.10068	6.42211	1.76564	1.65802	1.65231
	$10\delta_e$	6.74617	6.25425	6.57568	1.76670	1.65908	1.65337
	$15\delta_e$	6.77707	6.28515	6.60658	1.76683	1.65921	1.65350
	Pollaczek	6.81484	6.32215	6.64371	1.77047	1.66284	1.65713
60000	$5\delta_e$	67.3478	64.5070	64.4471	1.49249	1.40402	1.40410
	$10\delta_e$	68.6650	65.8243	65.7643	1.49300	1.40453	1.40461
	$15\delta_e$	68.9727	66.1319	66.0720	1.49306	1.40458	1.40466
	Pollaczek	69.3549	66.5095	66.4430	1.49589	1.40739	1.40745
600000	$5\delta_e$	698.632	689.808	689.808	1.22252	1.13908	1.13908
	$10\delta_e$	709.490	700.667	700.667	1.22201	1.13856	1.13856
	$15\delta_e$	711.493	702.670	702.670	1.22186	1.13842	1.13842
	Pollaczek	714.613	705.740	705.740	1.22453	1.14107	1.14107

The earth return current enclosed by the boundary is calculated from E_e in (4.2) with numerical integration over the FEM mesh, and its real and imaginary parts are plotted in Fig. 4.8(a). A loop current of $1+j0$ A is assumed between the centre conductor of the cable and the earth. Comparing with Fig. 4.3 for the deeply buried SC cable, the earth current approaches its final value of $1+j0$ much slower as r_b increases. In Fig. 4.8(b) is the plot of the maximum differences. The maximum differences between the $[Z]$ calculated with $r_b=n\delta_e$ and the $[Z]$ calculated with $r_b=(n\text{-}1)\delta_e$ is defined as the nth maximum difference. It is taken from all the elements in $[Z]$ in the frequency range from 1Hz to

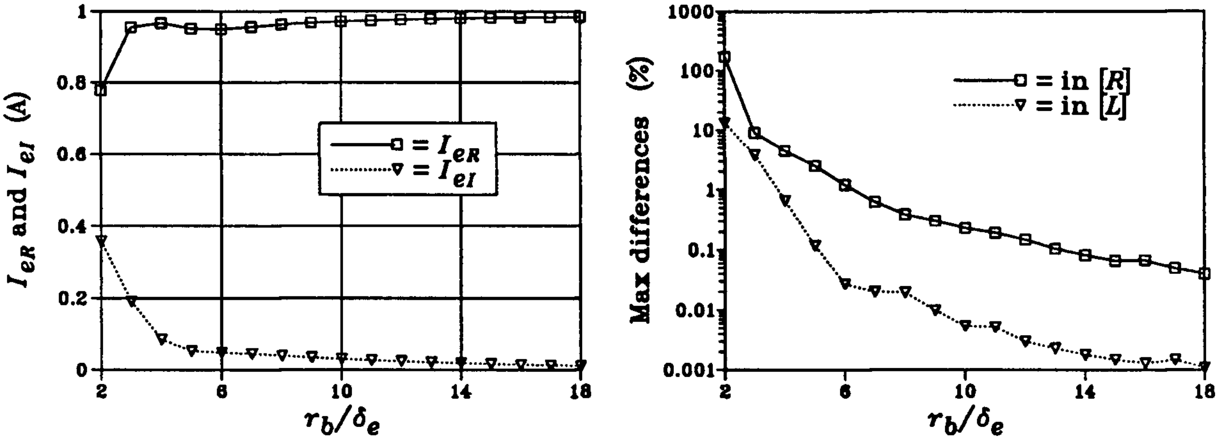

(a) enclosed earth current by r_b at 6kHz (b) max differences in $[R]$ and $[L]$

Figure 4.8: Earth return current and maximum differences in $[Z]$ for different r_b

1MHz. Fig. 4.8 shows that the maximum difference in $[R]$ decreases slowly. It reaches 0.07% at r_b=15δ_e. The maximum difference in $[L]$ reaches 0.027% even at r_b=6δ_e.

If the nth maximum difference is defined as the one between r_b=$(n$-$3)\delta_e$ and r_b=$n\delta_e$ and if 0.5% is chosen as the threshold value of the maximum difference in $[R]$ for stopping the iteration, r_b=12δ_e will be the iteration result because the maximum difference in $[R]$ is 0.55% at 12δ_e and .27% at 15δ_e. The numerical results show that the maximum difference in $[R]$ between 12δ_e and 15δ_e maintains the value 0.27% at different ρ_e and r_e. For ρ_e=100Ωm and r_e=24mm, the differences between the results found with the FEM having r_b=12δ_e and those found with Pollaczek's formula are less than 1.1% in $[R]$ and less than 0.25% in $[L]$ in the frequency range from 1Hz to 1MHz. Therefore, for the conventional FEM, a solution region with r_b $\geq$12δ_e will give reasonably accurate impedances for the shallowly buried SC cables.

4.5.2 Application of the proposed technique to $[Z]$ calculations of shallowly buried SC cables

The proposed technique discussed in Section 4.4 is applied to the same cable used in the preceding subsection with h=1.5m, r_e=24mm, ρ_e=100Ωm, and $\mu_e=\mu_0$. Four different r_b are used: 2.5m, 5m, 10m, and 25m. The meshes are similar to those in Fig. 4.7.

The impedances found with the proposed technique at different r_b are listed in Tab.4.7. "conventional" in the table represents the results found with the conventional FEM, and "Pollaczek" represents the results given by Pollaczek's formula. Good agreement can be observed among the three approaches. The partial earth return current I_{ep} used in the calculations at 60Hz, 6kHz, and 600kHz are listed in Tab.4.8. They correspond to a $1+j0$ A loop current between the cable and the earth.

If the earth return current is $1+j0$ A at 6kHz, the corresponding E field distributions in the air and the earth, given by (4.1) and (4.2), respectively, are plotted in Fig. 4.9. It can be seen that E is very smooth, except that it becomes singular at the location of the equivalent current filament. This smoothness makes the numerical integration easier. For the same earth current and frequency, the corresponding J contour lines in the earth from the three approaches are plotted in Fig. 4.10. "proposed" represents the results found with the proposed technique with r_b=5m, and "analytical" represents the results derived from (4.2). The plotting area is 2.5m by 3.5m. Good agreement in the J distributions among the three approaches can be observed from Fig. 4.10.

The efficiency of the proposed technique is compared with that of the conventional FEM. For the above calculations, storage and CPU time requirements for the proposed technique with r_b=5m are listed in Tab.4.9 and Tab.4.10, respectively. The CPU time is taken from a VAX-750. I_{ep} represents the time in calculating the earth return current with numerical integration. M, N, and BW are the same as in Subsection 3.6.2.

Table 4.7: $[Z]$ of the shallowly buried SC coaxial cable from the proposed technique

f (Hz)	r_b (m)	R (Ω/km) R_{11}	R_{12}	R_{22}	L (mH/km) L_{11}	L_{12}	L_{22}
6	conventional	0.0447186	0.00590137	0.420432	2.50922	2.35681	2.35015
	2.5	0.0447465	0.00592928	0.420460	2.51230	2.35989	2.35323
	5	0.0447465	0.00592928	0.420460	2.51207	2.35966	2.35300
	10	0.0447465	0.00592928	0.420460	2.51172	2.35931	2.35266
	25	0.0447465	0.00592928	0.420460	2.51144	2.35903	2.35238
	Pollaczek	0.0447405	0.00592928	0.420395	2.51380	2.36132	2.35467
60	conventional	0.100950	0.0592246	0.473745	2.27700	2.12620	2.11955
	2.5	0.101193	0.0594680	0.473988	2.28000	2.12921	2.12255
	5	0.101193	0.0594680	0.473988	2.27977	2.12898	2.12232
	10	0.101193	0.0594680	0.473988	2.27943	2.12863	2.12198
	25	0.101193	0.0594681	0.473988	2.27915	2.12835	2.12170
	Pollaczek	0.101147	0.0594682	0.473924	2.28130	2.13064	2.12399
600	conventional	0.696866	0.598624	1.01209	2.02019	1.89537	1.88872
	2.5	0.699635	0.601394	1.01486	2.02243	1.89761	1.89096
	5	0.699635	0.601394	1.01486	2.02220	1.89738	1.89073
	10	0.699636	0.601394	1.01486	2.02185	1.89703	1.89039
	25	0.699640	0.601399	1.01487	2.02157	1.89675	1.89011
	Pollaczek	0.699820	0.601403	1.01481	2.02392	1.89904	1.89240
6000	conventional	6.79056	6.29865	6.62008	1.76687	1.65925	1.65354
	2.5	6.81436	6.32245	6.64388	1.76903	1.66142	1.65570
	5	6.81438	6.32246	6.64389	1.76880	1.66119	1.65547
	10	6.81443	6.32251	6.64394	1.76846	1.66084	1.65513
	25	6.81482	6.32290	6.64433	1.76818	1.66056	1.65485
	Pollaczek	6.81484	6.32215	6.64371	1.77047	1.66284	1.65713
60000	conventional	69.0895	66.2488	66.1888	1.49306	1.40459	1.40467
	2.5	69.3455	66.5047	66.4448	1.49441	1.40594	1.40602
	5	69.3470	66.5063	66.4463	1.49418	1.40571	1.40579
	10	69.3523	66.5115	66.4516	1.49383	1.40536	1.40544
	25	69.3739	66.5332	66.4732	1.49350	1.40503	1.40511
	Pollaczek	69.3549	66.5095	66.4430	1.49589	1.40739	1.40745
600000	conventional	712.336	703.512	703.512	1.22179	1.13835	1.13835
	2.5	714.293	705.469	705.469	1.22308	1.13964	1.13964
	5	714.421	705.597	705.597	1.22284	1.13940	1.13940
	10	714.270	705.447	705.447	1.22235	1.13891	1.13891
	25	713.826	705.003	705.003	1.22215	1.13871	1.13871
	Pollaczek	714.613	705.740	705.740	1.22453	1.14107	1.14107

Table 4.8: I_{ep} found with numerical integrations for the proposed technique

f (Hz)		Re(I_{ep}) and Im(I_{ep}) (p.u.) r_b=2.5m	r_b=5m	r_b=10m	r_b=25m
60	Re(I_{ep})	0.583064×10^{-5}	0.233561×10^{-4}	0.936563×10^{-4}	0.589085×10^{-3}
	Im(I_{ep})	0.486857×10^{-4}	0.174161×10^{-3}	0.603340×10^{-3}	0.302400×10^{-2}
6000	Re(I_{ep})	0.598188×10^{-3}	0.241264×10^{-2}	0.973100×10^{-2}	0.598538×10^{-1}
	Im(I_{ep})	0.314763×10^{-2}	0.105046×10^{-1}	0.324944×10^{-1}	0.125884
600000	Re(I_{ep})	0.641595×10^{-1}	0.233091	0.646749	1.005062
	Im(I_{ep})	0.130791	0.310736	0.434091	0.895586×10^{-1}

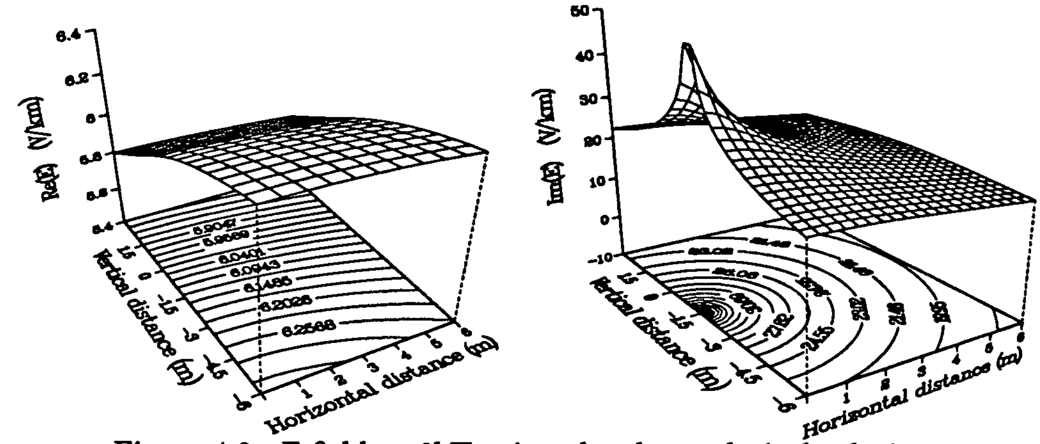

Figure 4.9: E field at 6kHz given by the analytical solution

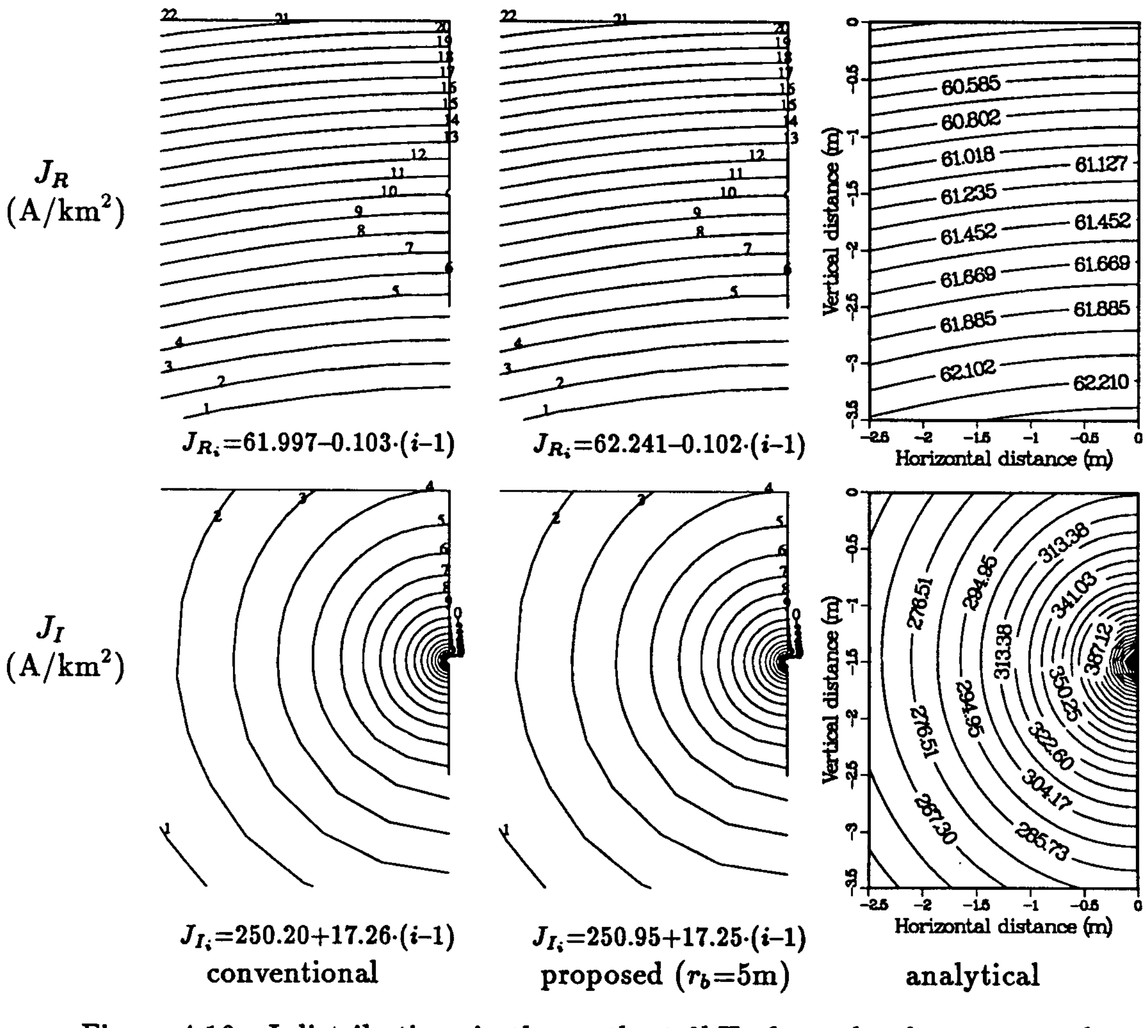

Figure 4.10: J distributions in the earth at 6kHz from the three approaches

Table 4.9: Storage and other parameters for the proposed technique (r_b=5m)

f (Hz)	M	N	BW	matrix dimension	storage (bytes)
60	283	88	36	4351×1	302064
6k	343	106	36	5356×1	365976
600k	403	124	36	6361×1	429888

Table 4.10: CPU time requirements for the proposed technique (r_b=5m)

f (Hz)	matrix formation	matrix factorization	solution	others	I_{ep}	total	total–I_{ep}
60	6.8 s (8.6%)	9.9 s (12.4%)	8.0 s (10.1%)	4.2 s (5.3%)	50.4 s (63.5%)	79.3 s	28.9 s
6k	8.7 s (9.9%)	11.8 s (13.4%)	7.7 s (8.7%)	5.1 s (5.7%)	55.1 s (62.3%)	88.4 s	33.3 s
600k	10.1 s (11.3%)	13.8 s (15.4%)	8.1 s (9.1%)	5.8 s (6.5%)	51.8 s (57.8%)	89.6 s	37.8 s

For the conventional FEM with r_b=12δ_e, the storage and CPU time requirements for the same problem are listed in Tab.4.11 and Tab.4.12, respectively.

Table 4.11: Storage and other parameters for the conventional FEM (r_b=12δ_e)

f (Hz)	M	N	BW	matrix dimension	storage (bytes)
60	463	142	32	9196× 1	507600
6k	463	142	32	9196× 1	509328
600k	463	142	33	9259× 1	512064

Tab.4.9–Tab.4.12 indicate that less storage is needed for the proposed technique than for the conventional FEM due to a smaller solution region. As the frequency becomes large, the storage requirement becomes similar for both approaches. The total CPU time with the proposed technique is much higher than with the conventional FEM. On average, about 60% of the total time is spent on the I_{ep} calculation. As long as the earth parameters ρ_e, μ_e, and r_e, as well as the locations of the equivalent current filaments do not change, I_{ep} only needs to be calculated once. By deducting the time for calculating I_{ep} from the total CPU time, the proposed technique will require less CPU time than the conventional FEM.

Table 4.12: CPU time requirements for the conventional FEM (r_b=12δ_e)

f (Hz)	matrix formation	matrix factorization	solution	others	total
60	11.3 s (25.8%)	21.9 s (50.0%)	4.1 s (9.4%)	6.5 s (14.7%)	43.8 s
6k	11.6 s (27.0%)	20.7 s (48.4%)	4.0 s (9.3%)	6.5 s (15.2%)	42.8 s
600k	11.9 s (27.2%)	21.3 s (48.8%)	3.9 s (9.0%)	6.5 s (15.0%)	43.6 s

If ρ_e is varied with r_e remaining at 24mm, the maximum differences between the results from the conventional FEM and from the proposed technique are listed in Tab.4.13. They are chosen from all the elements in $[Z]$ in the frequency range from 1Hz to 1MHz.

Table 4.13: Maximum differences in $[Z]$ with the proposed technique at different ρ_e

ρ_e	r_b=2.5m		r_b=5m		r_b=10m		r_b=25m	
(Ωm)	in R	in L	in R	in L	in R	in L	in R	in L
1000	1.05%	0.15%	1.05%	0.14%	1.05%	0.13%	1.05%	0.12%
100	1.05%	0.15%	1.05%	0.14%	1.05%	0.12%	1.05%	0.11%
10	1.05%	0.14%	1.05%	0.13%	1.05%	0.12%	1.05%	0.10%
1	1.02%	0.14%	1.02%	0.13%	1.02%	0.11%	1.02%	0.09%
0.1	1.02%	0.13%	1.02%	0.12%	1.02%	0.10%	1.02%	0.08%

If r_e is varied with ρ_e remaining at 100Ωm, the corresponding maximum differences are listed in Tab.4.14

Table 4.14: Maximum differences in $[Z]$ with the proposed technique at different r_e

r_e	r_b=2.5m		r_b=5m		r_b=10m		r_b=25m	
(mm)	in R	in L	in R	in L	in R	in L	in R	in L
50	1.05%	0.15%	1.05%	0.14%	1.05%	0.12%	1.05%	0.11%
100	1.05%	0.15%	1.05%	0.14%	1.05%	0.12%	1.05%	0.11%
250	1.52%	0.15%	1.23%	0.14%	1.13%	0.13%	1.05%	0.11%
500	4.11%	0.62%	2.89%	0.53%	1.91%	0.45%	1.23%	0.15%
1000	—	—	7.99%	1.72%	4.56%	1.42%	2.20%	0.48%

From the results presented in this subsection it can be seen that for small r_e/δ_e accurate impedances of shallowly buried SC cables can be obtained with the proposed technique. With this technique, the solution region in the earth becomes small and fixed. In contrast, the solution region with the conventional FEM varies with the frequency in order to save time, and becomes very large at low frequencies. Small regions are easier to mesh than larger ones. The proposed technique takes more CPU time compared to the conventional FEM, but if I_{ep} is calculated only once, it will require less time.

4.5.3 Comparisons between analytical results and FEM results for shallowly buried SC cables

The conventional FEM is used to investigate the errors of Pollaczek's formula under different conditions. With the same assumption that the cable in Fig. 3.9(a) is buried 1.5m beneath the earth, the impedances of the cable are calculated with both the conventional FEM and Pollaczek's formula for different ρ_e and r_e. The maximum differences between the impedances from the two approaches are listed in Tab.4.15, within the frequency range of 1Hz to 1MHz.

Table 4.15: Maximum differences in $[Z]$ with Pollaczek's formula at different ρ_e

ρ_e	r_e=24mm		r_e=100mm		r_e=250m		r_e=1000mm	
(Ωm)	in R	in L	in R	in L	in R	in L	in R	in L
1000	0.48%	0.22%	0.48%	0.22%	0.64%	0.24%	4.35%	0.26%
100	0.48%	0.24%	0.97%	0.22%	2.80%	0.23%	13.35%	2.20%
10	0.48%	0.25%	3.28%	0.25%	8.85%	1.57%	16.49%	8.50%
1	2.56%	0.24%	12.36%	2.91%	20.29%	8.22%	172.49%	9.71%
0.1	9.66%	3.29%	20.34%	15.98%	47.96%	15.47%	14394.04%	9.66%

Tab.4.15 indicates that large discrepancies between the two approaches appear mainly in $[R]$. For $[L]$ the overall differences for the listed combinations of ρ_e and r_e are less than 20%.

If ρ_e, μ_e, and r_e are fixed, there is generally a frequency beyond which the differences become larger than a specified tolerance value. This frequency shall be called "threshold frequency." For a 1% tolerance, the threshold frequencies for different ρ_e and r_e are listed in Tab.4.16. By converting the threshold frequencies together with the corresponding ρ_e, μ_e, and r_e into a parameter r_e/δ_e, it is found out that for a given r_e, this parameter r_e/δ_e

is almost constant for different ρ_e. With r_e=24mm, r_e/δ_e is 0.0213 in $[R]$ and 0.0674 in $[L]$. This means that if $r_e/\delta_e \leq 0.0213$, the differences between Pollaczek's formula and FEM are less than 1%. r_e/δ_e related to each r_e is listed at the bottom of Tab.4.16.

Table 4.16: Threshold f with Pollaczek's formula for maximum differences≤1%

ρ_e	r_e=24mm		r_e=100mm		r_e=250m		r_e=1000mm	
(Ωm)	in R	in L	in R	in L	in R	in L	in R	in L
1000	> 1MHz	> 1MHz	> 1MHz	> 1MHz	> 1MHz	> 1MHz	60kHz	> 1MHz
100	> 1MHz	> 1MHz	> 1MHz	> 1MHz	100kHz	> 1MHz	6kHz	400kHz
10	> 1MHz	> 1MHz	100kHz	> 1MHz	10kHz	400kHz	600Hz	40kHz
1	200kHz	> 1MHz	10kHz	200kHz	1kHz	40kHz	60Hz	4kHz
0.1	20kHz	200kHz	1kHz	20kHz	100Hz	4kHz	6Hz	400Hz
r_e/δ_e	0.02133	0.06744	0.01987	0.08886	0.01571	0.09935	0.01539	0.12566

For a 10% tolerance the threshold frequencies are shown in Tab.4.17, and for a 30% tolerance the threshold frequencies are shown in Tab.4.18.

Table 4.17: Threshold f with Pollaczek's formula for maximum differences≤10%

ρ_e	r_e=24mm		r_e=100mm		r_e=250m		r_e=1000mm	
(Ωm)	in R	in L	in R	in L	in R	in L	in R	in L
1000	> 1MHz	> 1MHz	> 1MHz	> 1MHz	> 1MHz	> 1MHz	> 1MHz	> 1MHz
100	> 1MHz	> 1MHz	> 1MHz	> 1MHz	> 1MHz	> 1MHz	400kHz	> 1MHz
10	> 1MHz	> 1MHz	> 1MHz	> 1MHz	> 1MHz	> 1MHz	40kHz	> 1MHz
1	> 1MHz	> 1MHz	600kHz	> 1MHz	100kHz	> 1MHz	4kHz	> 1MHz
0.1	> 1MHz	> 1MHz	60kHz	400kHz	10kHz	100kHz	400Hz	> 1MHz
r_e/δ_e	—	—	0.15391	0.39738	0.15708	0.49673	0.12566	—

Table 4.18: Threshold f with Pollaczek's formula for maximum differences≤30%

ρ_e	r_e=24mm		r_e=100mm		r_e=250m		r_e=1000mm	
(Ωm)	in R	in L	in R	in L	in R	in L	in R	in L
1000	> 1MHz	> 1MHz	> 1MHz	> 1MHz	> 1MHz	> 1MHz	> 1MHz	> 1MHz
100	> 1MHz	> 1MHz	> 1MHz	> 1MHz	> 1MHz	> 1MHz	> 1MHz	> 1MHz
10	> 1MHz	> 1MHz	> 1MHz	> 1MHz	> 1MHz	> 1MHz	> 1MHz	> 1MHz
1	> 1MHz	> 1MHz	> 1MHz	> 1MHz	> 1MHz	> 1MHz	400kHz	> 1MHz
0.1	> 1MHz	> 1MHz	> 1MHz	> 1MHz	800kHz	> 1MHz	40kHz	> 1MHz
r_e/δ_e	—	—	—	—	1.40496	—	1.25664	—

From the results presented in this subsection, it can be concluded that Pollaczek's formula for the self impedances of shallowly buried SC cables gives reasonably accurate results for ρ_e in the range of 1000Ωm to 1Ωm, and for r_e in the range of 24mm to 250mm, within the frequency range of 1Hz to 1MHz.

4.5.4 $[Z]$ calculations for a cable layout of arbitrary structure

It is assumed that the cable in Fig. 3.9(a) is located in an tunnel as shown in Fig. 4.11(a), with h=1.5m, h_2=0.25m, w=0.5m, ρ_e=1Ωm, and μ_e=μ_0. The impedances of the cable are calculated with the conventional FEM and with the proposed technique. As there is no definite r_e here, Pollaczek's formula is used with two approximate r_e of 250mm and 500mm. r_b=5m is used with the proposed technique and the corresponding FEM mesh at 600kHz is shown in Fig. 4.11(b).

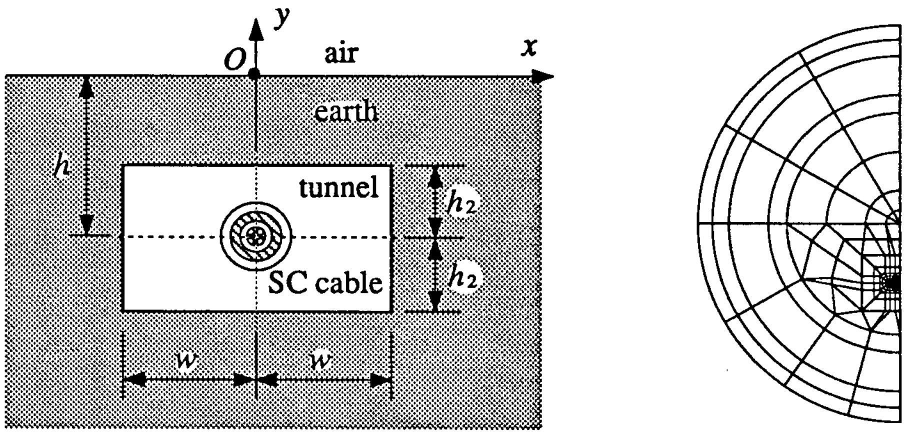

(a) cable layout (b) FEM mesh at 600kHz (r_b=5m)
Figure 4.11: The layout of a tunnel installed cable and the FEM mesh at 600kHz

The impedances found with three approaches are listed in Tab.4.19. "Pollaczek1" represents the results from Pollaczek's formula with r_e=250mm, and "Pollaczek2" represents the results with r_e=500mm. Tab.4.19 indicates that for small r_e/δ_e, Pollaczek's formula gives results which are almost independent of r_e. The maximum differences between the proposed technique and the conventional FEM are 4.37% in $[R]$ and 0.91% in $[L]$ from 1Hz to 1MHz. The maximum differences between Pollaczek's formula and

Table 4.19: [Z] of the tunnel installed cable from three approaches

f (Hz)	approach	R (Ω/km)			L (mH/km)		
		R_{11}	R_{12}	R_{22}	L_{11}	L_{12}	L_{22}
6	conventional	0.0447930	0.00597572	0.420506	2.04825	1.89584	1.88918
	proposed	0.0448095	0.00599228	0.420523	2.05020	1.89779	1.89113
	Pollaczek1	0.0448038	0.00599263	0.420459	2.05154	1.89906	1.89241
	Pollaczek2	0.0448038	0.00599255	0.420458	2.05154	1.89906	1.89241
60	conventional	0.102843	0.0611180	0.475638	1.81237	1.66158	1.65492
	proposed	0.103030	0.0613047	0.475825	1.81420	1.66341	1.65675
	Pollaczek1	0.103012	0.0613333	0.475789	1.81533	1.66467	1.65802
	Pollaczek2	0.103005	0.0613260	0.475781	1.81533	1.66467	1.65802
600	conventional	0.741197	0.642955	1.05642	1.54492	1.42010	1.41345
	proposed	0.745902	0.647661	1.06113	1.54557	1.42075	1.41410
	Pollaczek1	0.748330	0.649913	1.06332	1.54678	1.42191	1.41526
	Pollaczek2	0.747710	0.649293	1.06270	1.54680	1.42193	1.41528
6000	conventional	7.39506	6.90314	7.22457	1.26626	1.15864	1.15293
	proposed	7.50986	7.01794	7.33937	1.26433	1.15671	1.15100
	Pollaczek1	7.66821	7.17553	7.49709	1.26433	1.15670	1.15099
	Pollaczek2	7.61851	7.12583	7.44739	1.26459	1.15696	1.15125
60000	conventional	61.1415	58.3008	58.2408	0.97484	0.88637	0.88645
	proposed	60.5850	57.7442	57.6843	0.96679	0.87832	0.87840
	Pollaczek1	68.8430	65.9976	65.9311	0.95450	0.86600	0.86606
	Pollaczek2	65.5297	62.6843	62.6177	0.95774	0.86923	0.86930
600000	conventional	362.441	353.617	353.617	0.79508	0.71164	0.71164
	proposed	355.463	346.639	346.639	0.79609	0.71264	0.71264
	Pollaczek1	506.977	498.103	498.103	0.72688	0.64342	0.64342
	Pollaczek2	361.874	353.000	353.000	0.75557	0.67211	0.67211

the conventional FEM are 30.87% in [R] and 14.25% in [L] with r_e=250mm, and are 14.88% in [R] and 6.95% in [L] with r_e=500mm. If ρ_e is 100Ωm, the maximum differences become 5.23% in [R] and 0.42% in [L] with r_e=250mm, and become 4.18% in [R] and 0.38% in [L] with r_e=500mm. These results suggest that the impedances of a cable layout of arbitrary structures can still be calculated with Pollaczek's formula by using an approximate r_e.

For a loop current of $1+j0$ A at 600kHz between the centre conductor of the cable and the earth, the J contours found with the proposed technique and with the conventional FEM are plotted in Fig. 4.12. The plotted area is 2m horizontally by 2.5m vertically. Fig. 4.12 shows good agreement between the field distributions of the proposed technique and of the conventional FEM. It also shows that the tunnel structure does not have a strong impact on the field distribution, although small deformations can be observed in J_R near the tunnel.

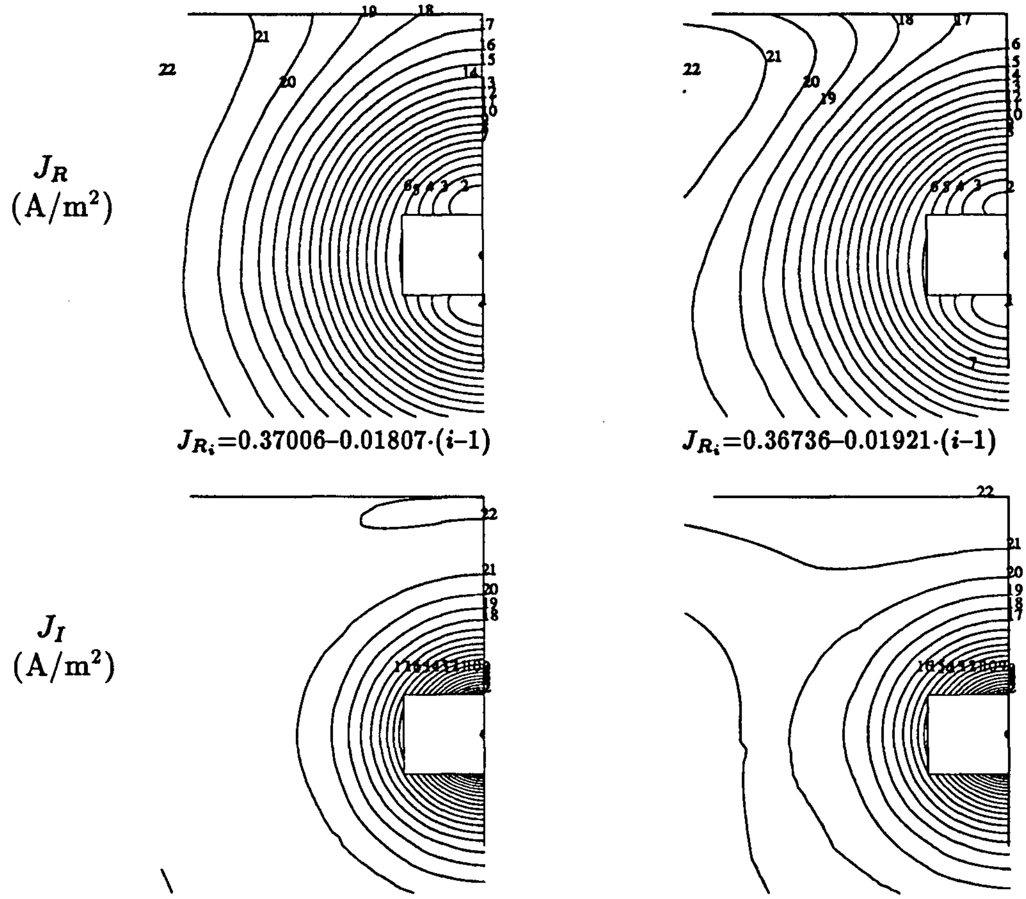

J_{R_i}=0.37006–0.01807·(i–1) J_{R_i}=0.36736–0.01921·(i–1)

J_{I_i}=0.83914–0.04282·(i–1) J_{I_i}=0.84298–0.04604·(i–1)
conventional proposed (r_b=5m)

Figure 4.12: J distributions in the earth at 600kHz from the FEM

4.6 Summary

In this chapter, a technique is proposed to reduce the earth region when the earth penetration depth is large. Good agreements are observed for the calculated impedances and for the field distributions between the conventional FEM and the proposed technique. The solution region is small and independent of frequency, which helps in the meshing process. The comparisons show that the proposed technique requires less CPU time than the conventional FEM if partial earth return currents are calculated only once.

The conventional FEM and the proposed technique are applied to deeply and shallowly buried cables and tunnel installed cables. In the impedance calculation of deeply buried SC coaxial cables, accurate results can be obtained with the conventional FEM if $r_b > 3\delta_e$. With the proposed technique, accurate results are obtained if r_b/δ_e is small at small r_e, or if r_e/δ_e is small at large r_e. For r_e=24mm, the errors of the proposed technique are less than 1% compared with the conventional FEM if $r_b/\delta_e \leq 0.2$.

In the impedance calculation of shallowly buried and tunnel installed SC coaxial cables, $r_b \geq 12\delta_e$ is required for the conventional FEM. Comparisons with Pollaczek's formula for the shallowly buried cables show that there are discrepancies with the conventional FEM when the earth penetration is small. For typical ranges of ρ_e and r_e, however, the discrepancies are reasonably small. With ρ_e varying between 1000Ωm to 1Ωm and with r_e varying between 24mm to 250mm, the maximum discrepancies are less than 21% in [R] and less than 9% in [L]. The field solutions of a tunnel installed cable show that arbitrary structures inside the earth do not have a strong influence on the field distribution. Pollaczek's formula can still be applied to find impedances of such a cable by using an approximate r_e.

Chapter 5

Admittance Calculation with Finite Element Method

5.1 Introduction

If the insulating materials in a multiconductor system have complicated geometries, then $[Y]$ of the system cannot be calculated analytically. Instead, numerical methods have to be used. In general, shunt conductances among conductors are ignored. Therefore, the task of the $[Y]$ calculation is simplified into a $[C]$ calculation.

According to the assumptions given in Section 2.2, only surface charges exist, and the parallel conductors have uniform cross section longitudinally. This simplifies the capacitance calculation into a two-dimensional steady-state electric field solution problem. The solution region is set up by removing all the regions inside conductors from the solution region in the $[Z]$ calculation.

Several numerical methods could be applied, including BEM and FEM. Because the steady-state electric field solution is a special case of the quasi steady-state magnetic field solution, most of the FEM techniques for solving the magnetic field can be applied directly to solve the electric field. The corresponding software can easily be adapted to handle the electric field solution. Therefore, only FEM is used in this thesis.

In this chapter the general procedures for applying FEM to the steady-state electric field solution are first discussed. The energy method and the surface charge method to calculate the capacitances from the field solutions are derived next. The general form of $[C]$ for SC coaxial cables is also given. The results of the $[C]$ calculation of a SC coaxial cable by FEM show that isoparametric elements are better than simplex elements in this case.

5.2 Principal Equation and FEM solution

The assumption that there is no volume charge inside the conductors is justified in [10], based on the equation

$$\nabla \cdot \mathbf{E} = \frac{\rho}{\epsilon} = \frac{1}{\sigma}\nabla \cdot \mathbf{J} = -\frac{1}{\sigma}\frac{d\rho}{dt} \tag{5.1}$$

where ϵ is permittivity, ρ is volume charge density, and σ is conductivity. It is pointed out in [10] that, as $\rho = \rho_0 e^{-(\sigma/\epsilon)t}$, any charges introduced into a conductor will dilute themselves to the surface with a time constant of ϵ/σ. For a poor conducting earth with $\rho_e = 1000\ \Omega$m, the corresponding time constant is still a very small value in the order of 10^{-8} s. In cable related transient studies, the smallest time step is typically in the order of 10^{-6} s. Compared to the above time constant, such a time step is large enough to ensure that there is no volume charge inside the conductors.

Because the charges are on the conductor surfaces only and there is no field inside the conductors, the solution region for the electric field will be composed of insulations bounded partly by conductor surfaces. Introducing the scalar potential ϕ as

$$\mathbf{E} = -\nabla\phi \tag{5.2}$$

the following Laplace equation can be derived

$$\epsilon\nabla^2\phi = 0 \tag{5.3}$$

This is the governing equation describing the electric field. The boundary conditions are still Dirichlet boundary conditions on Γ_0 and homogeneous Neumann boundary conditions on Γ_1.

ϕ also appeared in the $[Z]$ calculation. In that case, ϕ is the longitudinal potential in conductors which is caused by applied conductor currents. It is constant in the transverse direction in each conductor. In the $[C]$ calculation, however, ϕ represents the transverse potential function caused by voltages applied on the conductor surfaces.

Comparing the governing equations (5.3) in the $[C]$ calculation with (2.17) in the $[Z]$ calculation, it can be seen that (2.17) will be reduced to the same form as (5.3) if there is no conductor region. With suitable boundary conditions, the real part of the A solution for (2.17) will be the ϕ solution for (5.3). That is the reason why the steady-state electric field solution is a special case of the quasi steady-state magnetic field solution.

With FEM, ϕ is assumed as

$$\phi = \sum_{n=1}^{N_T} \phi_n \varphi_n \tag{5.4}$$

where ϕ_n is the value of ϕ at FEM node n, and N_T and φ_n are the same as before. With the same procedure as discussed in Chapter 2, the following algebraic equation can be derived

$$[U][\phi] = [\mathbf{0}] \tag{5.5}$$

where

$$[\phi] = [\phi_1, \phi_2, \ldots, \phi_{N_T}]^T \tag{5.6}$$

$$U_{mn} = \int_{S_R} \epsilon \nabla\varphi_m \cdot \nabla\varphi_n ds \quad (m = 1, 2, \ldots, N; n = 1, 2, \ldots, N_T) \tag{5.7}$$

S_R and N remain the same as before, and ϵ is the permittivity. By dividing S_R into elements and assuming that ϕ has the following form in element E_i

$$\phi = \sum_{n=1}^{N_{B_i}} \phi_n^{E_i} \varphi_n^{E_i} ds \quad \text{in} \quad S_{E_i} \tag{5.8}$$

where $\phi_n^{E_i}$ is the node value of ϕ in the element, the integral U_{mn} in S_{E_i} becomes

$$U_{mn}^{E_i} = \epsilon_{E_i} \int_{S_{B_i}} \nabla\varphi_m^{E_i} \cdot \nabla\varphi_n^{E_i} ds \tag{5.9}$$

where $m = 1, 2, \ldots, N_{E_i}$ excluding boundary nodes, $n = 1, 2, \ldots, N_{E_i}$, and i=1,2,...,M. N_{E_i} and M remain the same as before. Obviously, all the discussions and formulas in Chapter 2 and Chapter 3 referring to the formulation of $[U]$ for different elements and to the solution of the final algebraic equations are applicable here, provided that $\frac{1}{\mu}$ is replaced by ϵ.

5.3 $[C]$ Calculation from the Field Solutions

$[C]$ can easily be calculated from the solved potential field distribution under specific boundary conditions. Similar to the $[Z]$ calculation, there are two methods for finding $[C]$: the energy method and the surface charge method.

Before discussing these two methods, the capacitances of a multiconductor system are first defined: $C_{s_{i0}}$ is the direct capacitance per unit length between conductor i and the reference conductor, and $C_{m_{ij}}$ is the direct mutual capacitance per unit length between conductors i and j. These capacitances are shown in Fig. 5.1.

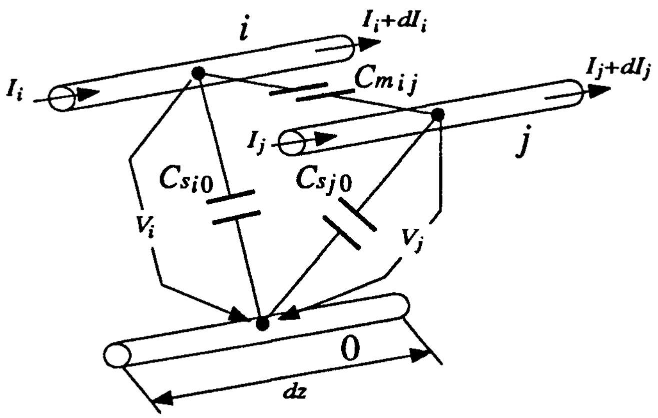

Figure 5.1: Direct capacitances for multiconductor systems

For conductor i shown in Fig. 5.1, the following equation is derived

$$I_i - (j\omega C_{s_{i0}} dz)V_i - \sum_{\substack{k=1 \\ k \neq i}}^{K} (j\omega C_{m_{ik}} dz)(V_i - V_k) = I_i + dI_i \tag{5.10}$$

or

$$-\frac{dI_i}{dz} = j\omega(C_{s_{i0}} + \sum_{\substack{k=1 \\ k \neq i}}^{K} C_{m_{ik}})V_i - j\omega \sum_{\substack{k=1 \\ k \neq i}}^{K} C_{m_{ik}} V_k = j\omega \sum_{k=1}^{K} C_{ik} V_k \tag{5.11}$$

where C_{ik} is the element in $[C]$, which is related to the direct capacitances by

$$C_{ii} = C_{s_{i0}} + \sum_{\substack{k=1 \\ k \neq i}}^{K} C_{m_{ik}} \qquad (i = 1, 2, \ldots, K) \tag{5.12}$$

$$C_{ik} = -C_{m_{ik}} \qquad (i, k = 1, 2, \ldots, K; k \neq i) \tag{5.13}$$

For the complete system, (5.11) has the matrix form

$$-\frac{d[I]}{dz} = j\omega[C][V] \tag{5.14}$$

This equation is essentially (2.2) provided that $[G]$ is ignored. (5.12) and (5.13) are used in the energy method to find $[C]$ from the field solutions.

5.3.1 The energy method

With this method, the electric energy stored in the field under specific boundary conditions is calculated, and the elements of $[C]$ are derived from the energy. Once the potential distribution is known, the following equation is used to find the electric energy from the field

$$\begin{aligned} W_{E_P} &= \frac{1}{2}\int_{S_R} \epsilon \mathbf{E} \cdot \mathbf{E} ds = \frac{1}{2}\int_{S_R} \epsilon \nabla\varphi \cdot \nabla\varphi ds \\ &= \frac{1}{2}\sum_{i=1}^{M} \epsilon_{E_i} [\phi^{E_i}]^T [U^{E_i}][\phi^{E_i}] \end{aligned} \tag{5.15}$$

where

$$[\phi^{E_i}] = [\phi_1^{E_i}, \phi_2^{E_i}, \ldots, \phi_{N_{Bi}}^{E_i}]^T \tag{5.16}$$

$[\phi^{E_i}]$ is the node value vector of ϕ in element E_i. ϵ_{E_i} is the permittivity in E_i.

Fig. 5.2 shows the cross section of the conductor system in Fig. 5.1. From circuit analysis, if $V_i = V_0 \neq 0$ and $V_j = 0$ $(j = 1, 2, \ldots, K; j \neq i)$, the stored electric energy is

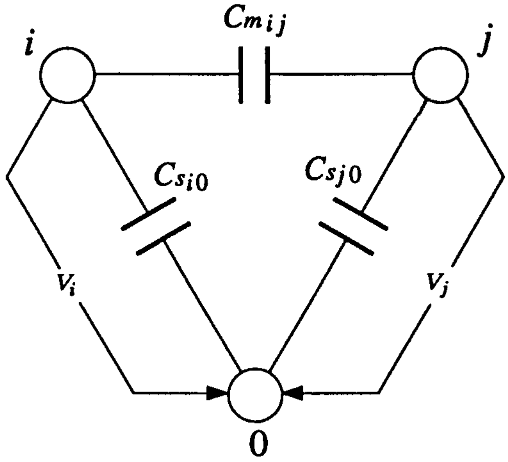

Figure 5.2: Direct capacitances under DC condition

given by

$$W_{E_C}^{ii} = \frac{1}{2} C_{si0} V_0^2 + \frac{1}{2} \sum_{\substack{k=1 \\ k \neq i}}^{K} C_{m_{ik}} V_0^2 = \frac{1}{2} C_{ii} V_0^2 \tag{5.17}$$

For these conductor voltage conditions, the corresponding boundary conditions in the field solution are that all potentials at the boundary nodes on the surface of conductor i are V_0 and that the potentials at the rest of the boundary nodes are zero. If the energy calculated from the potential distribution is represented by $W_{E_P}^{ii}$, C_{ii} becomes

$$C_{ii} = \frac{2 W_{E_P}^{ii}}{V_0^2} \tag{5.18}$$

By assuming $V_i = V_j = V_0 \neq 0$ and $V_k = 0$ $(k = 1, 2, \ldots, K; k \neq i; k \neq j)$, the stored electric energy from circuit analysis becomes

$$
\begin{aligned}
W_{E_C}^{ij} &= \frac{1}{2}C_{s_{i0}}V_0^2 + \frac{1}{2}\sum_{\substack{k=1 \\ k \neq i}}^{K} C_{m_{ik}}V_0^2 - \frac{1}{2}C_{m_{ij}}V_0^2 \\
&+ \frac{1}{2}C_{s_{j0}}V_0^2 + \frac{1}{2}\sum_{\substack{k=1 \\ k \neq j}}^{K} C_{m_{ik}}V_0^2 - \frac{1}{2}C_{m_{ij}}V_0^2 \\
&= \frac{1}{2}(C_{ii} + C_{jj} + 2C_{ij})V_0^2
\end{aligned}
\tag{5.19}
$$

For the field solution, the potentials at the boundary nodes on the surfaces of conductors i and j are V_0. The potentials at the rest of the boundary nodes are zero. If $W_{E_F}^{ij}$ represents the stored energy in the field, C_{ij} will be

$$
C_{ij} = \frac{W_{E_F}^{ij}}{V_0^2} - \frac{C_{ii}}{2} - \frac{C_{jj}}{2} \tag{5.20}
$$

As the system is linear, the field needs to be solved only K times, with one conductor surface having non-zero potential each time. From these K solutions, $W_{E_F}^{ii}$ is calculated and C_{ii} is evaluated. By superimposing two solutions, $W_{E_F}^{ij}$ and C_{ij} can then be found.

This method is simple, and the potential distribution solved by FEM is used directly to find $[C]$. One interpretation of FEM for the Laplace equation is that FEM trys to find a solution that will minimize the energy in the field. Therefore, $[C]$ calculated with the energy method should always be slightly larger than the exact value, unless the solution itself is exact.

5.3.2 The surface charge method

With this method, $[C]$ is found from the surface charges per unit length on the conductors under specific boundary conditions. The surface charges are calculated from the integration of **D** along the contours of the conductors.

From electrostatic field analysis, the surface charges per unit length on the conductors in Fig. 5.2 are related to $[C]$ through the following equation

$$[q] = [C][V] \tag{5.21}$$

where

$$[q] = [q_1, q_2, \ldots, q_K]^T \tag{5.22}$$

q_i is the surface charge per unit length on conductor i. $[V]$ is the same as before. If $V_i = V_0 \neq 0$ and $V_j = 0$ $(j = 1, 2, \ldots, K; j \neq i)$, the elements of the ith column in $[C]$ can be found from the corresponding surface charges as

$$C_{ji} = \frac{q_j}{V_0} \qquad (j = 1, 2, \ldots, K) \tag{5.23}$$

q_j is given by

$$q_j = \int_{\Gamma_{C_j}} \mathbf{D} \cdot \mathbf{dl} = \int_{\Gamma_{C_j}} \pm|\mathbf{D}|\sqrt{dx^2 + dy^2} \tag{5.24}$$

where Γ_{C_j} is the periphery of the cross-section area of the jth conductor. $\mathbf{dl}$ is an integral element with a direction normal to Γ_{C_j}. The plus and minus signs in the above formula are related to the direction of $\mathbf{D}$. $|\mathbf{D}|$ is calculated from

$$|\mathbf{D}| = \epsilon|\mathbf{E}| = \epsilon|\nabla\phi| = \epsilon\sqrt{\left(\frac{\partial\phi}{\partial x}\right)^2 + \left(\frac{\partial\phi}{\partial y}\right)^2} \tag{5.25}$$

The system of equations needs to be solved K times, with one conductor surface having non-zero potential each time.

In order to evaluate the integral (5.24) in a simplex element, the vertices are numbered in the same way as shown in Fig. 3.1. Three possible combinations can be obtained by permuting three node numbers: (1,2,3), (2,3,1), and (3,1,2). (m, n, o) is used to represent these three combinations.

Assuming that the integral (5.24) in element E_i is along the side from vertices m to n on which $\zeta_o = 0$ and $d\zeta_o = 0$, the corresponding integral Δq can be derived as

$$\Delta q = \epsilon_{E_i}\sqrt{(x_n - x_m)^2 + (y_n - y_m)^2}\int_0^1 \pm\sqrt{\left(\frac{\partial\phi}{\partial x}\right)^2 + \left(\frac{\partial\phi}{\partial y}\right)^2}\, d\zeta_n \qquad (5.26)$$

and

$$\begin{aligned}
\frac{\partial\phi}{\partial x} &= \sum_{j=1}^{N_{E_i}} \phi_j^{E_i}\frac{\partial\varphi_j^{E_i}}{\partial x} = \sum_{j=1}^{N_{E_i}} \phi_j^{E_i}\left(\frac{\partial\varphi_j^{E_i}}{\partial\zeta_m}\frac{\partial\zeta_m}{\partial x} + \frac{\partial\varphi_j^{E_i}}{\partial\zeta_n}\frac{\partial\zeta_n}{\partial x}\right) \\
&= \frac{1}{2S_{E_i}}\sum_{j=1}^{N_{E_i}} \phi_j^{E_i}\left((y_n - y_o)\frac{\partial\varphi_j^{E_i}}{\partial\zeta_m} + (y_o - y_m)\frac{\partial\varphi_j^{E_i}}{\partial\zeta_n}\right) &(5.27)\\
\frac{\partial\phi}{\partial y} &= \frac{1}{2S_{E_i}}\sum_{j=1}^{N_{E_i}} \phi_j^{E_i}\left((x_o - x_n)\frac{\partial\varphi_j^{E_i}}{\partial\zeta_m} + (x_m - x_o)\frac{\partial\varphi_j^{E_i}}{\partial\zeta_n}\right) &(5.28)\\
\frac{\partial\varphi_j^{E_i}}{\partial\zeta_m} &= \frac{\partial P_{jm}(N_p,\zeta_m)}{\partial\zeta_m}P_{jn}(N_p,\zeta_n)\frac{\partial P_{jo}(N_p, 1-\zeta_m-\zeta_n)}{\partial\zeta_m} &(5.29)\\
\frac{\partial\varphi_j^{E_i}}{\partial\zeta_n} &= P_{jm}(N_p,\zeta_m)\frac{\partial P_{jn}(N_p,\zeta_n)}{\partial\zeta_n}\frac{\partial P_{jo}(N_p, 1-\zeta_m-\zeta_n)}{\partial\zeta_n} &(5.30)
\end{aligned}$$

where P_{jm}, P_{jn}, and P_{jo} are given by (3.5) and (3.6). $\frac{\partial\phi}{\partial x}$ and $\frac{\partial\phi}{\partial y}$ in (5.27) and (5.28) can also be expressed in terms of $\frac{\partial\varphi_j^{E_i}}{\partial\zeta_n}$ and $\frac{\partial\varphi_j^{E_i}}{\partial\zeta_o}$ or in terms of $\frac{\partial\varphi_j^{E_i}}{\partial\zeta_o}$ and $\frac{\partial\varphi_j^{E_i}}{\partial\zeta_m}$, if (5.29) and (5.30) are modified correspondingly.

In order to simplify the calculation of $\frac{\partial\varphi_j^{E_i}}{\partial\zeta_m}$ and $\frac{\partial\varphi_j^{E_i}}{\partial\zeta_n}$, $P_m(N_p,\zeta)$ is changed into real polynomial form

$$P_m(N_p,\zeta) = \frac{1}{d_m}\sum_{i=0}^{m} a_{mi}\zeta^i \qquad (5.31)$$

in which d_m is the common denominator. a_{mi} is the polynomial coefficient. d_m and a_{mi} are associated with order N_p and with m, and they are listed for order 1 to 6 in Tab.5.1.

As $\frac{\partial\phi}{\partial x}$ and $\frac{\partial\phi}{\partial y}$ can be found for any given $(\zeta_m, \zeta_n, \zeta_o)$ from (5.27) to (5.30), Δq in (5.26) can now be evaluated by applying the Gaussian quadrature discussed in Section 3.3.1.

Table 5.1: d_m and a_{mi} in $P_m(N_p,\zeta) = \frac{1}{d_m}\sum_{i=0}^{m} a_{mi}\zeta^i$

N_p	m	d_m	a_{m0}	a_{m1}	a_{m2}	a_{m3}	a_{m4}	a_{m5}	a_{m6}
1	0	1	1						
	1	1	0	1					
2	0	1	1						
	1	1	0	2					
	2	1	0	-1	2				
3	0	1	1						
	1	1	0	3					
	2	2	0	-3	9				
	3	2	0	2	-9	9			
4	0	1	1						
	1	1	0	4					
	2	1	0	-2	8				
	3	3	0	4	-24	32			
	4	3	0	-3	22	-48	32		
5	0	1	1						
	1	1	0	5					
	2	2	0	-5	25				
	3	6	0	10	-75	125			
	4	24	0	-30	275	-750	625		
	5	24	0	24	-250	875	-1250	625	
6	0	1	1						
	1	1	0	6					
	2	1	0	-3	18				
	3	1	0	2	-18	36			
	4	2	0	-3	33	-108	108		
	5	5	0	6	-75	315	-540	324	
	6	10	0	-10	137	-675	1530	-1620	648

For isoparametric elements, dx, dy, $\frac{\partial\phi}{\partial x}$, and $\frac{\partial\phi}{\partial y}$ in element E_i can be derived as

$$\begin{bmatrix} dx \\ dy \end{bmatrix} = \begin{bmatrix} \frac{\partial x}{\partial v} & \frac{\partial x}{\partial \nu} \\ \frac{\partial y}{\partial v} & \frac{\partial y}{\partial \nu} \end{bmatrix} \begin{bmatrix} dv \\ d\nu \end{bmatrix} = \left[J_a^{E_i}\right]^T \begin{bmatrix} dv \\ d\nu \end{bmatrix} \tag{5.32}$$

$$\begin{bmatrix} \frac{\partial\phi}{\partial x} \\ \frac{\partial\phi}{\partial y} \end{bmatrix} = \begin{bmatrix} \frac{\partial}{\partial x} \\ \frac{\partial}{\partial y} \end{bmatrix} [\beta][\phi^{E_i}] = [D^{E_i}][\phi^{E_i}] \tag{5.33}$$

where $[J_a^{E_i}]$ and $[D^{E_i}]$ are given by (3.22) and (3.25), respectively. $[\beta]$ is given by (3.19) for quadrilateral isoparametric elements, or by (3.28) for triangular isoparametric elements.

If the integration within a quadrilateral element is along the side from local nodes 1 to 2 as shown in Fig. 3.5, $\nu = -1$ and $d\nu = 0$, and from (5.32)

$$\begin{bmatrix} \frac{dx}{dv} \\ \frac{dy}{dv} \end{bmatrix} = \left[J_a^{E_i}\right]^T \begin{bmatrix} 1 \\ 0 \end{bmatrix} \tag{5.34}$$

The corresponding integral Δq becomes

$$\Delta q = \epsilon_{E_i} \int_{-1}^{1} \pm\sqrt{\left(\frac{dx}{dv}\right)^2 + \left(\frac{dy}{dv}\right)^2} \sqrt{\left(\frac{\partial \phi}{\partial x}\right)^2 + \left(\frac{\partial \phi}{\partial y}\right)^2} dv \tag{5.35}$$

Once the local coordinates of sampling points for the numerical integration are known along this side, $\frac{\partial\phi}{\partial x}$, $\frac{\partial\phi}{\partial y}$, $\frac{dx}{dv}$, and $\frac{dy}{dv}$ are calculated from (5.33) and (5.34), respectively, and Δq from (5.35). For integrations along the other sides, similar formulas can be derived.

If the integration is within a triangular element along the side from local nodes 1 to 2 as shown in Fig. 3.6, $\nu = -v + 1$; therefore,

$$\begin{bmatrix} \frac{dx}{dv} \\ \frac{dy}{dv} \end{bmatrix} = \left[J_a^{E_i}\right]^T \begin{bmatrix} 1 \\ \frac{d\nu}{dv} \end{bmatrix} = \left[J_a^{E_i}\right]^T \begin{bmatrix} 1 \\ -1 \end{bmatrix} \tag{5.36}$$

with Δq having the same form as in (5.35).

The concept of this method is very simple; however, the software implementation is rather complicated compared with the energy method. Although ϕ is continuous in FEM solutions, $\mathbf{E}$ is not. This may introduce errors in $[C]$.

5.4 $[C]$ Calculation of SC Coaxial Cables

In this section the capacitances of SC coaxial cables are obtained, and the results are compared with those from analytical formulas.

5.4.1 General form of $[C]$ for SC coaxial cables

The same notations will be used as in Section 2.6 or as shown in Fig. 2.4. For the SC cable shown in Fig. 2.4 there are K insulations. The kth insulation is between conductors

k and k+1, and the capacitance per unit length related to the insulation is

$$C_{IN_k} = \frac{2\pi\epsilon_k}{\ln\left(\frac{r_{A_{k+1}}}{r_{B_k}}\right)} \qquad (k = 1, 2, \ldots, K) \tag{5.37}$$

where ϵ_k is the permittivity of the kth insulation. The general form of $[C]$ for SC coaxial cables, which only has three diagonals[10], is

$$[C] = \begin{bmatrix} C_1^d & C_2^{od} & & & & \\ C_2^{od} & C_2^d & C_3^{od} & & & 0 \\ & C_3^{od} & C_3^d & C_4^{od} & & \\ & & \ddots & \ddots & \ddots & \\ & 0 & & C_{K-1}^{od} & C_{K-1}^d & C_K^{od} \\ & & & & C_K^{od} & C_K^d \end{bmatrix} \tag{5.38}$$

where

$$\begin{aligned} C_1^d &= C_{IN_1} \\ C_k^d &= C_{IN_{k-1}} + C_{IN_k} \qquad (k = 2, 3, \ldots, K) \\ C_k^{od} &= -C_{IN_{k-1}} \qquad (k = 2, 3, \ldots, K) \end{aligned} \tag{5.39}$$

5.4.2 [C] calculation of a SC coaxial cable by FEM

$[C]$ of the SC coaxial cable shown in Fig. 3.9 is calculated by FEM. As shown in the figure, ϵ_r=1 is assumed for both insulations. The solution region is similar to Fig. 3.9(b), except that the two conductor regions are removed.

As in the $[Z]$ calculation, the span angle θ and the division radii will affect the results. When studying the influence of division radii on $[C]$, a small θ is used. In Tab.5.2 five different radius divisions are listed. As the solution region is made up by two disconnected insulation regions, the division radii for each division scheme are listed for these two regions separately.

Table 5.2: Radius divisions in $[C]$ calculation of the SC coaxial cable

division	division radii (mm)									
	inner insulation					outer insulation				
division1	12	18				22	24			
division2	12	15	18			22	23	24		
division3	12	14	16	18		22	22.7	23.3	24	
division4	12	13	15	17	18	22	22.3	23	23.7	24
division5	12	12.3	17.7	18		22	22.1	23.9	24	

The results of the $[C]$ calculation are given in Tab.5.3 for different division schemes with $\theta = 1^{o}$. Values from the analytical formula (5.38) are also included in the table. It can be seen that, with all division schemes, the capacitances calculated by the energy method have four digit accuracy for all types of elements except the first order simplex element. With this method, the calculated values for C_{12} and C_{21} are the same as $-C_{11}$. The capacitances calculated by the surface charge method depend on division scheme. C_{12} is the same as $-C_{11}$ and C_{21} is slightly different from C_{12} due to different integration surfaces in the surface charge calculation.

It can be seen from Tab.5.3 that for simplex elements higher order methods give more accurate results, at the expense of more nodes and of longer computation time. For all the division schemes, the 3rd order simplex element seems to be an optimum choice, since the results are not improved significantly by further increasing the order of the element.

For the numerical integration in the surface charge method the number of sampling points in the Gaussian quadrature can easily be decided for a simplex element. For a N_pth order simplex element, with ϕ being a polynomial function of order N_p, E calculated from ϕ by differentiation will be a polynomial function of order $N_p - 1$. Therefore, the number of sampling points will be $((N_p + 1)/2)$, truncated to the nearest integer. For isoparametric elements, the results do not change very much after the number of sampling points goes beyond five.

Tab.5.3 shows that different radius division schemes will mostly affect the results

Table 5.3: [C] of a two-conductor SC coaxial cable

	element	Energy Method (μF/km)		Surface charge method (μF/km)		
		C_{11} ($-C_{12}$, $-C_{21}$)	C_{22}	C_{11} ($-C_{12}$)	C_{21}	C_{22}
analytical		0.137017	0.775503	0.137017	-0.137017	0.775503
division1	iso	0.137037	0.775523	0.133333	-0.133333	0.771014
	sim2	0.137039	0.775533	0.133337	-0.133337	0.771034
	sim3	0.137018	0.775507	0.136559	-0.137476	0.775724
	sim4	0.137017	0.775505	0.136963	-0.136963	0.775439
	sim5	0.137017	0.775504	0.136999	-0.137035	0.775278
	sim6	0.137017	0.775504	0.137014	-0.137014	0.775487
division2	iso	0.137018	0.775504	0.135886	-0.136261	0.774537
	sim1	0.137503	0.776107	0.122225	-0.150004	0.774416
	sim2	0.137019	0.775509	0.135882	-0.136274	0.774382
	sim3	0.137017	0.775505	0.136932	-0.137069	0.775334
	sim4	0.137017	0.775504	0.137001	-0.137026	0.775290
	sim5	0.137017	0.775504	0.137004	-0.137029	0.775312
	sim6	0.137017	0.775504	0.137004	-0.137029	0.775346
division3	iso	0.137017	0.775503	0.136476	-0.136701	0.775082
	sim1	0.137236	0.775784	0.126680	-0.145309	0.773857
	sim2	0.137018	0.775507	0.136467	-0.136719	0.774854
	sim3	0.137017	0.775505	0.136978	-0.137045	0.775232
	sim4	0.137017	0.775504	0.137000	-0.137035	0.775239
	sim5	0.137017	0.775504	0.137000	-0.137036	0.775291
	sim6	0.137017	0.775504	0.137000	-0.137036	0.775349
division4	iso	0.137017	0.775503	0.136871	-0.136942	0.775409
	sim1	0.137178	0.775717	0.131691	-0.141097	0.775312
	sim2	0.137017	0.775505	0.136852	-0.136976	0.774867
	sim3	0.137017	0.775504	0.136987	-0.137053	0.774995
	sim4	0.137017	0.775504	0.136988	-0.137053	0.775182
	sim5	0.137017	0.775504	0.136987	-0.137052	0.775321
	sim6	0.137017	0.775504	0.136989	-0.137048	0.775380
division5	iso	0.137029	0.775515	0.137015	-0.137022	0.775506
	sim1	0.138374	0.777170	0.136666	-0.139537	0.776884
	sim2	0.137029	0.775517	0.136955	-0.137140	0.774046
	sim3	0.137017	0.775504	0.136938	-0.137119	0.775028
	sim4	0.137017	0.775504	0.136948	-0.137091	0.775356
	sim5	0.137017	0.775504	0.136966	-0.137064	0.775324
	sim6	0.137017	0.775504	0.136981	-0.137049	0.775392

from the surface charge method. If the potentials of the centre conductor and on the outmost boundary in Fig. 3.9(b) are zero, and the potential of the second conductor is 1 V, the corresponding surface $|\mathbf{E}|$ calculated by FEM with isoparametric elements are given in Tab.5.4. The table shows that a closer division radius towards the boundary

Table 5.4: Surface $|\mathbf{E}|$ for different divisions with isoparametric elements

	$\|\mathbf{E}(r)\|$ (V/mm)			
	r=12 mm	r=18 mm	r=22 mm	r=24 mm
analytical	0.205525	0.137017	0.522398	0.478865
division1	0.200000	0.133333	0.521739	0.478261
division2	0.203829	0.136261	0.522226	0.478720
division3	0.204713	0.136701	0.522312	0.478795
division4	0.205306	0.136943	0.522381	0.478852
division5	0.205522	0.137023	0.522396	0.478863

will improve the surface $\mathbf{E}$ results and consequently improve the accuracy of the surface charge method, as indicated in Tab.5.3.

When θ varies, the FEM mesh will be changed. If the whole circular region in Fig. 3.9(a) is considered, different θ will create different numbers of nodes and numbers of elements. The relative errors of numerical results compared with those given by the analytical formula are plotted in Fig. 5.3 for isoparametric elements and for the 3rd order simplex element. In the figure, EM stands for the energy method and SCM for the surface charge method. iso and sim3 are the same as before. It can be seen that isoparametric elements produce accurate results even at very large span angles, while the 3rd order simplex element only produces accurate results at small span angles. For other orders the results are similar. Therefore, isoparametric elements are more computation efficient, as less computation time will be required by fewer nodes and fewer elements in the FEM mesh.

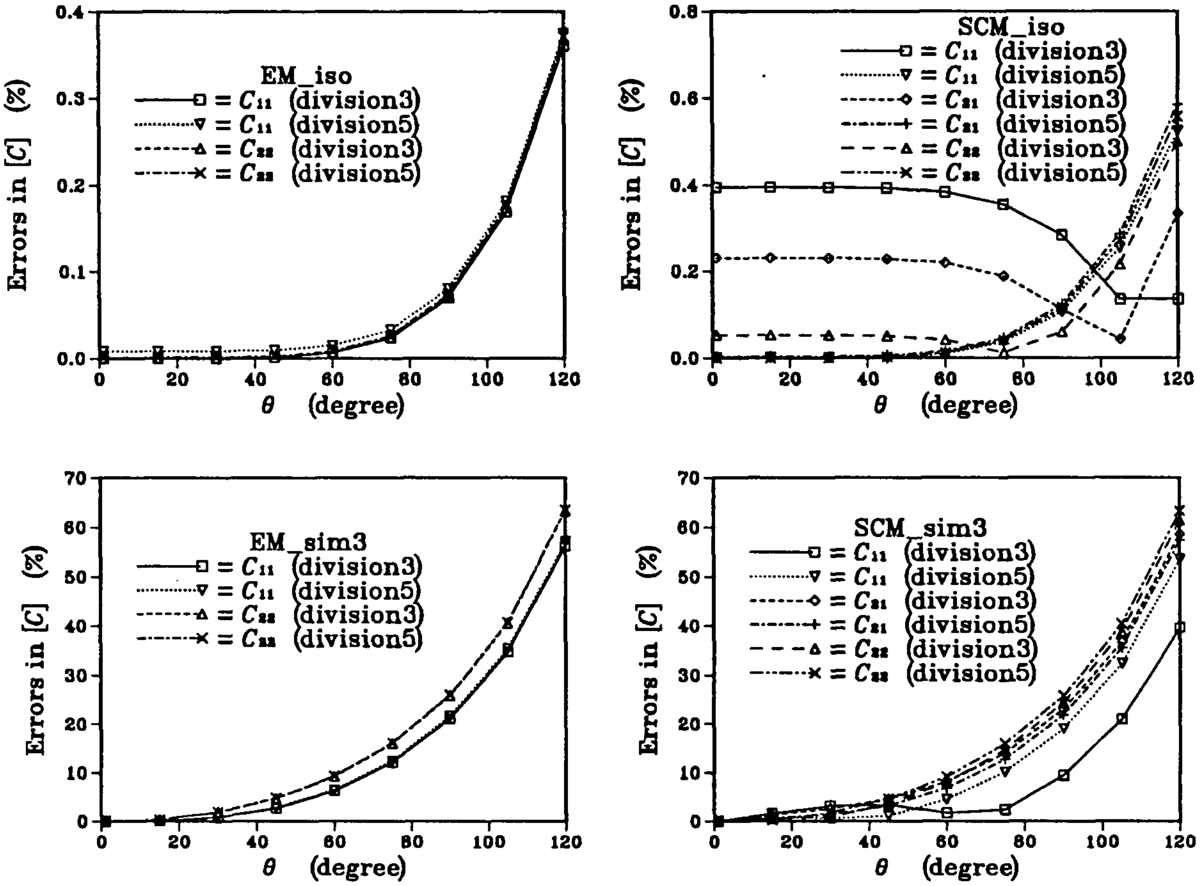

Figure 5.3: Errors in $[C]$ calculation of a SC coaxial cable for different span angles

5.5 Summary

In this chapter general procedures for solving the electrostatic field with FEM are discussed. The energy method and the surface charge method for calculating $[C]$ from the field solutions are derived. The energy method is simple and easy to implement compared with the surface charge method.

Both methods are applied to the SC cable shown in Fig. 3.9. For this case the results show that isoparametric elements achieve higher accuracy with fewer elements and nodes in the FEM mesh than simplex elements. The results also show that the energy method has less stringent requirements on the mesh, and has higher accuracy than the surface charge method. For isoparametric elements a division radius close to the conductor surface will improve the $[C]$ results found by the surface charge method, while for simplex elements similar improvements can be achieved by increasing the radial divisions.

Chapter 6

Case Studies in $[Z]$ and $[C]$ Calculations

6.1 Introduction

There are analytical formulas for the calculation of parameters of most types of power cables. These formulas are generally derived with certain approximations. For example, the impedance formulas of PT cables are derived by replacing the conductors inside the pipe with current filaments located at the centres of the conductors. By applying FEM, the parameters can be calculated without some of these approximations. This provides a way of verifying the validity of analytical formulas.

In this chapter, FEM is applied to the $[Z]$ calculation of buried or tunnel installed multiphase SC cables, of PT cables, of sector-shaped cables, and of stranded conductors. Capacitances of PT cables and sector-shaped cables are also calculated with FEM. The numerical results of $[Z]$ and $[C]$ are compared with those from the analytical formulas.

The comparisons show that for buried multiphase SC cables, accurate self and mutual impedances can be obtained with Pollaczek's formula. For tunnel installed SC cables, reasonably accurate self and mutual impedances can still be obtained with Pollaczek's formula. With PT cables, the analytical formulas may introduce errors at high frequencies due to neglected proximity effects. For sector-shaped cables, FEM results are compared with those from an approximate analytical formula recently suggested by Ametani[40]. Discrepancies are observed. For stranded conductors, comparisons are made among the results found with FEM, the subdivision method, the GSW formula, and Borges da Silva's formula. These comparisons show that close agreement is obtained between FEM results and the GSW formula if a factor of 1.6 is used in the formula instead of 2.25. Good agreement exists between FEM results and Borges da Silva's formula.

6.2 $[Z]$ Calculations of Buried or Tunnel Installed Multiphase Cable Systems

In Section 4.5 the impedances of a single phase cable are calculated, where mutual impedances only exist between the conductors within the cable. For multiphase cable systems, the mutual impedances among the conductors of different phases must be calculated as well. To use the formula (4.6) for the impedance between two phases, $(0,h)$ and (x_P,y_P) are assumed to correspond to the locations of the two phases, respectively.

In this section, the impedances of two 230kV three-phase SC cable systems are calculated with (4.6), with the conventional FEM, and with the proposed technique. Each phase consists of a two-conductor SC cable, as shown in Fig. 6.1(a). One system is buried as shown in Fig. 6.1(b), and the other is installed in a tunnel as shown in Fig. 6.1(c). The FEM meshes around the cables at 60Hz are given in Fig. 6.2. As there are six conductors

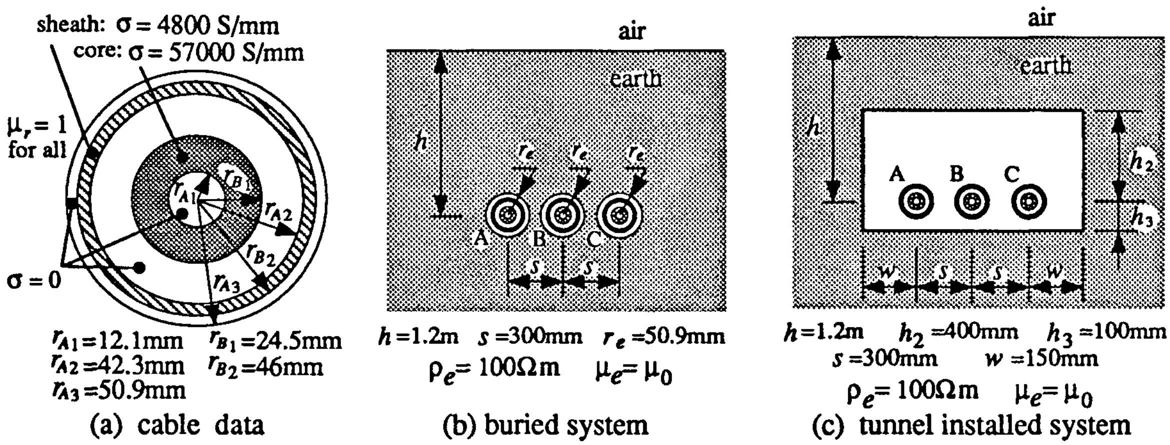

Figure 6.1: 230kV three-phase cable systems

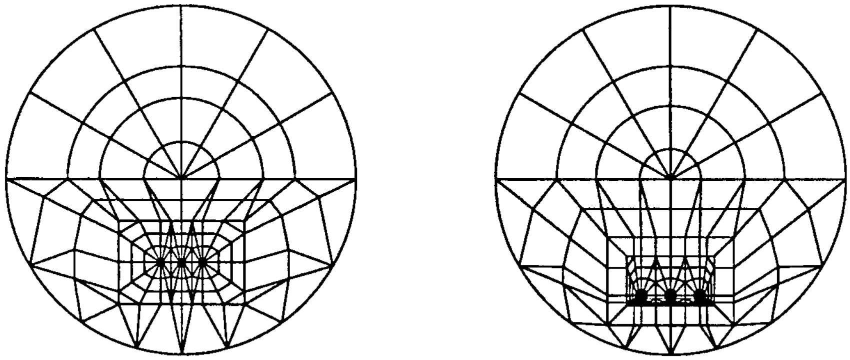

(a) buried cable system (b) tunnel installed cable system
Figure 6.2: Meshes around the cables at 60Hz for the two systems

in each system, the final $[Z]$ has the form of

$$[Z] = \begin{bmatrix} [Z_{\mathrm{AA}}] & [Z_{\mathrm{AB}}] & [Z_{\mathrm{AC}}] \\ [Z_{\mathrm{AB}}] & [Z_{\mathrm{BB}}] & [Z_{\mathrm{BC}}] \\ [Z_{\mathrm{AC}}] & [Z_{\mathrm{BC}}] & [Z_{\mathrm{CC}}] \end{bmatrix} \tag{6.1}$$

Subscripts A, B, and C represent the phases. All submatrices are 2×2 matrices, and $[Z_{\mathrm{AA}}]$, $[Z_{\mathrm{BB}}]$, and $[Z_{\mathrm{CC}}]$ are symmetric. The sheath conductor is numbered after the core conductor in each phase.

The impedances of the buried cable system are listed in Tab.6.1 and Tab.6.2. Because the meshes are symmetrical with respect to the center cable, $[Z_{\mathrm{AA}}]=[Z_{\mathrm{CC}}]$ and $[Z_{\mathrm{AB}}]=[Z_{\mathrm{BC}}]$. With Pollaczek's formula, it is assumed that $[Z_{\mathrm{AA}}]=[Z_{\mathrm{BB}}]=[Z_{\mathrm{CC}}]$, that all four elements in $[Z_{\mathrm{AB}}]$ are the same, and that all four elements in $[Z_{\mathrm{AC}}]$ are the same. Tab.6.1 and Tab.6.2 confirm that these assumptions are reasonably accurate for the given $\rho_e=100\Omega\mathrm{m}$. The tables show that the differences between the results from Pollaczek's formula and from FEM are small at low frequencies, but noticeable at high frequencies. Good agreement is observed between the conventional FEM and the proposed technique. The maximum differences between Pollaczek's formula and the

Table 6.1: $[Z_{AA}]([Z_{CC}])$ and $[Z_{BB}]$ of the buried three-phase cable system

f (Hz)			R (Ω/km) R_{11}	R_{12}	R_{22}	L (mH/km) L_{11}	L_{12}	L_{22}
60	$[z_{AA}]$	conv.	0.0748300	0.0597006	0.262705	2.10829	1.96073	1.95793
		prop.	0.0749538	0.0598244	0.262829	2.11098	1.96342	1.96062
	$[z_{BB}]$	conv.	0.0750753	0.0599458	0.262950	2.10904	1.96147	1.95868
		prop.	0.0751972	0.0600678	0.263072	2.11172	1.96416	1.96137
	Pollaczek		0.0745183	0.0594093	0.262382	2.12015	1.97267	1.96988
6000	$[z_{AA}]$	conv.	6.37885	6.16838	6.33678	1.61213	1.49146	1.48897
		prop.	6.39170	6.18123	6.34963	1.61402	1.49335	1.49086
	$[z_{BB}]$	conv.	6.38720	6.17672	6.34512	1.61034	1.48967	1.48718
		prop.	6.39999	6.18952	6.35792	1.61225	1.49158	1.48909
	Pollaczek		6.37657	6.16547	6.33386	1.62790	1.50717	1.50468
600000	$[z_{AA}]$	conv.	694.949	691.010	691.011	1.09676	0.98654	0.98654
		prop.	696.979	693.041	693.041	1.09769	0.98747	0.98747
	$[z_{BB}]$	conv.	694.819	690.880	690.881	1.09482	0.98460	0.98460
		prop.	696.919	692.980	692.981	1.09576	0.98554	0.98554
	Pollaczek		698.287	694.327	694.327	1.11182	1.00154	1.00154

Table 6.2: $[Z_{AB}]([Z_{BC}])$ and $[Z_{AC}]$ of the buried three-phase cable system

f (Hz)			R (Ω/km) R_{11}	R_{12}	R_{21}	R_{22}	L (mH/km) L_{11}	L_{12}	L_{21}	L_{22}
60	$[z_{AB}]$	conv.	0.05944	0.05944	0.05944	0.05944	1.586	1.586	1.586	1.586
		prop.	0.05957	0.05957	0.05957	0.05957	1.589	1.589	1.589	1.589
		Poll.	0.05940				1.589			
	$[z_{AC}]$	conv.	0.05895	0.05895	0.05895	0.05895	1.449	1.449	1.449	1.449
		prop.	0.05908	0.05908	0.05908	0.05908	1.452	1.452	1.452	1.452
		Poll.	0.05940				1.451			
6000	$[z_{AB}]$	conv.	6.085	6.085	6.085	6.085	1.120	1.120	1.120	1.120
		prop.	6.098	6.098	6.098	6.098	1.122	1.122	1.122	1.122
		Poll.	6.092				1.125			
	$[z_{AC}]$	conv.	6.066	6.066	6.066	6.066	0.989	0.989	0.989	0.989
		prop.	6.079	6.079	6.079	6.079	0.990	0.990	0.990	0.990
		Poll.	6.091				0.986			
600000	$[z_{AB}]$	conv.	685.9	685.9	685.9	685.9	0.622	0.622	0.622	0.622
		prop.	687.9	687.9	687.9	687.9	0.623	0.623	0.623	0.623
		Poll.	689.1				0.626			
	$[z_{AC}]$	conv.	679.9	679.9	679.9	679.9	0.492	0.492	0.492	0.492
		prop.	681.8	681.8	681.8	681.8	0.492	0.492	0.492	0.492
		Poll.	682.5				0.488			

conventional FEM are 1.8% in $[R]$ and 1.78% in $[L]$ from 1Hz to 1MHz, and the maximum differences between the proposed technique and the conventional FEM are 0.49% in $[R]$ and 0.18% in $[L]$ from 1Hz to 1MHz.

The impedances of the tunnel installed cable system are listed in Tab.6.3 and

Tab.6.4. r_e=300mm is used with Pollaczek's formula. Again, the differences between Pollaczek's formula and the conventional FEM become noticeable at high frequencies.

Table 6.3: $[Z_{AA}]([Z_{CC}])$ and $[Z_{BB}]$ of the tunnel installed three-phase cable system

f (Hz)			R (Ω/km) R_{11}	R_{12}	R_{22}	L (mH/km) L_{11}	L_{12}	L_{22}
60	$[Z_{AA}]$	conv.	0.0748252	0.0596958	0.262700	2.11131	1.96375	1.96096
		prop.	0.0749517	0.0598223	0.262827	2.11394	1.96637	1.96358
	$[Z_{BB}]$	conv.	0.0750711	0.0599417	0.262946	2.11116	1.96360	1.96080
		prop.	0.0751999	0.0600705	0.263075	2.11376	1.96620	1.96340
	Pollaczek		0.0745182	0.0594092	0.262382	2.12015	1.97267	1.96988
6000	$[Z_{AA}]$	conv.	6.37058	6.16010	6.32850	1.61540	1.49473	1.49224
		prop.	6.38852	6.17804	6.34644	1.61716	1.49649	1.49400
	$[Z_{BB}]$	conv.	6.37804	6.16757	6.33597	1.61276	1.49209	1.48960
		prop.	6.39624	6.18576	6.35416	1.61448	1.49381	1.49132
	Pollaczek		6.37618	6.16508	6.33347	1.62790	1.50717	1.50468
600000	$[Z_{AA}]$	conv.	675.093	671.155	671.155	1.10341	0.99319	0.99319
		prop.	685.630	681.692	681.692	1.10176	0.99154	0.99154
	$[Z_{BB}]$	conv.	672.579	668.641	668.641	1.10084	0.99061	0.99061
		prop.	683.822	679.884	679.884	1.09903	0.98881	0.98881
	Pollaczek		695.484	691.523	691.523	1.11193	1.00166	1.00166

Table 6.4: $[Z_{AB}]([Z_{BC}])$ and $[Z_{AC}]$ of the tunnel installed three-phase cable system

f (Hz)			R (Ω/km) R_{11}	R_{12}	R_{21}	R_{22}	L (mH/km) L_{11}	L_{12}	L_{21}	L_{22}
60	$[Z_{AB}]$	conv.	0.05944	0.05944	0.05944	0.05944	1.584	1.584	1.584	1.584
		prop.	0.05957	0.05957	0.05957	0.05957	1.587	1.587	1.587	1.587
		Poll.	0.05940				1.589			
	$[Z_{AC}]$	conv.	0.05894	0.05894	0.05894	0.05894	1.448	1.448	1.448	1.448
		prop.	0.05907	0.05907	0.05907	0.05907	1.450	1.450	1.450	1.450
		Poll.	0.05940				1.451			
6000	$[Z_{AB}]$	conv.	6.077	6.077	6.077	6.077	1.118	1.118	1.118	1.118
		prop.	6.095	6.095	6.095	6.095	1.120	1.120	1.120	1.120
		Poll.	6.092				1.125			
	$[Z_{AC}]$	conv.	6.060	6.060	6.060	6.060	0.987	0.987	0.987	0.987
		prop.	6.078	6.078	6.078	6.078	0.989	0.989	0.989	0.989
		Poll.	6.091				0.986			
600000	$[Z_{AB}]$	conv.	665.5	665.5	665.5	665.5	0.624	0.624	0.624	0.624
		prop.	676.0	676.0	676.0	676.0	0.622	0.622	0.622	0.622
		Poll.	689.1				0.626			
	$[Z_{AC}]$	conv.	661.4	661.4	661.4	661.4	0.494	0.494	0.494	0.494
		prop.	671.9	671.9	671.9	671.9	0.492	0.492	0.492	0.492
		Poll.	682.5				0.488			

The maximum differences are 4.81% in $[R]$ and 1.87% in $[L]$ from 1Hz to 1MHz. The maximum differences between the proposed technique and the conventional FEM are 2% in $[R]$ and 0.75% in $[L]$.

For both systems, the J distributions in the earth from the proposed technique and the conventional FEM are given in Fig. 6.3. In this distribution, a loop current of $1+j0$ A is assumed between the left phase and the earth at 600kHz. The field plotting area is 3m vertically by 3m horizontally. Comparing the fields of the buried cable system with the tunnel installed cable system shows that the tunnel structure does not have a significant influence on the field. Fig. 6.3 also indicates a good agreement between the fields from the proposed technique and the fields from the conventional FEM.

6.3 $[Z]$ and $[C]$ Calculations of PT Cables

6.3.1 The $[Z]$ calculation of PT cables

For the three-phase PT cable with SC coaxial cables inside, as shown in Fig. 1.1(a), it is very difficult, if not impossible, to obtain an analytical field solution. If the conductors inside the pipe are replaced by current filaments, however, the fields inside the pipe and within the pipe conductor can be solved analytically, and approximate impedance formulas can then be derived from the field solutions. The fields inside the pipe and within the pipe conductor were solved first by Tegopoulos *et al* in 1971[8], and the approximate formulas for the $[Z]$ calculation were developed first by Brown *et al* in 1976[13]. These formulas are widely used in cable parameter programs[23].

Several of the assumptions in the approximate formulas ignore factors which may influence the results of the $[Z]$ calculation. It is assumed that the fields within each SC coaxial cable inside the pipe remain cylindrical, to be able to use the formulas discussed in Section 2.6. This ignores the influence of the pipe and adjacent cables on the field

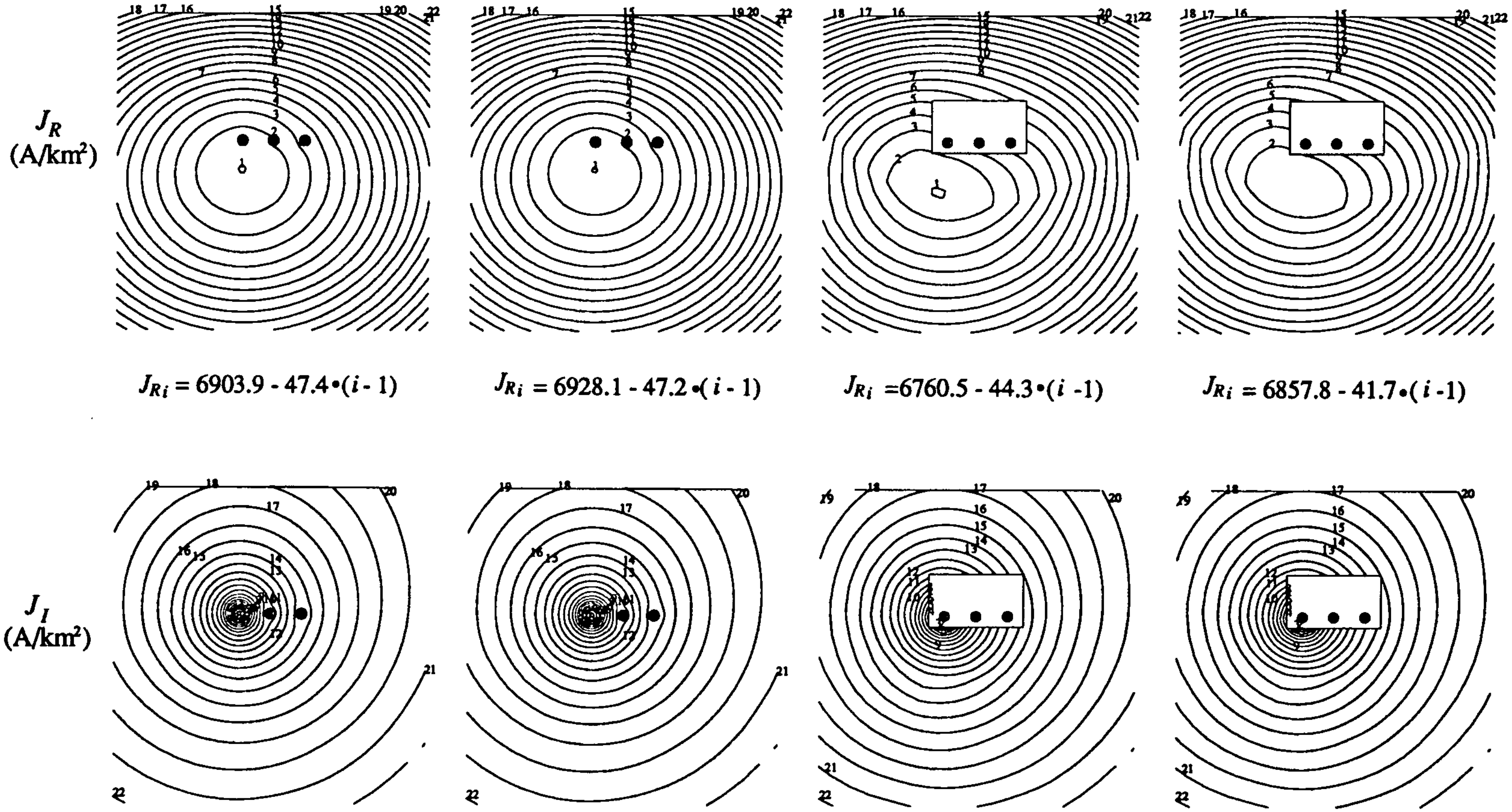

$J_{Ri} = 6903.9 - 47.4 \cdot (i - 1)$ $\quad$ $J_{Ri} = 6928.1 - 47.2 \cdot (i - 1)$ $\quad$ $J_{Ri} = 6760.5 - 44.3 \cdot (i - 1)$ $\quad$ $J_{Ri} = 6857.8 - 41.7 \cdot (i - 1)$

$J_{Ii} = 36453 - 1340 \cdot (i - 1)$ $\quad$ $J_{Ii} = 36486 - 1339 \cdot (i - 1)$ $\quad$ $J_{Ii} = 31626 - 1105 \cdot (i - 1)$ $\quad$ $J_{Ii} = 31563 - 1104 \cdot (i - 1)$

conventional proposed conventional proposed

(a) buried cable system (b) tunnel installed cable system

Figure 6.37 J distributions in the earth at 600 kHz with the earth current being $1+j0$ A distribution of the concerned cable. As the field solutions were derived for a loop current between a single current filament and the pipe, the influence of the other non-current carrying conductors on the field distributions inside the pipe and within the pipe conductor is ignored. The influence of the finite dimension of the current carrying conductor, which is replaced by a current filament for the formula derivation, is also ignored.

With FEM, these factors can be considered, and their effects of can be studied. A three-phase 230kV PT cable is given in Fig. 6.4. Each phase consists of a two-conductor SC cable as shown in Fig. 6.4(a). The non-linearity of the steel pipe is ignored, and a

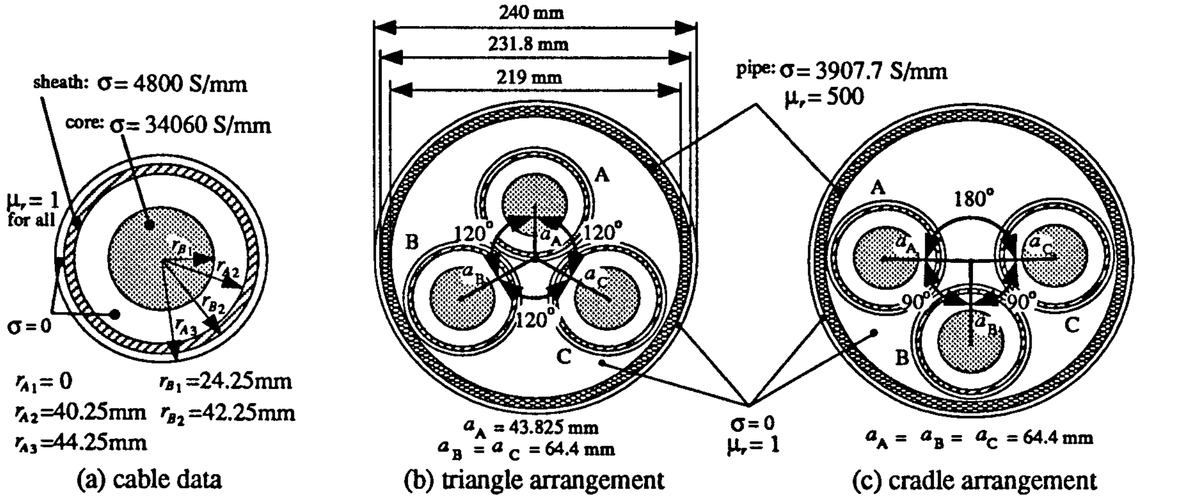

Figure 6.4: A 230kV PT cable system

constant μ_r=500 is assumed instead. Two arrangements of the SC cables inside the pipe are analyzed: the triangle arrangement and the cradle arrangement shown in Fig. 6.4(b) and (c), respectively. The meshes at 6kHz for both arrangements are plotted in Fig. 6.5. In the calculation, the pipe will be used as the return path, and the earth is not included. A=0 is assumed on the boundary in the meshes in Fig. 6.5. The structure of $[Z]$ is the same as in (6.1).

For the triangle arrangement the impedances are listed in Tab.6.5 and Tab.6.6. Due to symmetry, $[Z_{\rm BB}]$=$[Z_{\rm CC}]$ and $[Z_{\rm AB}]$=$[Z_{\rm AC}]$. "ana" in the tables stands for the results

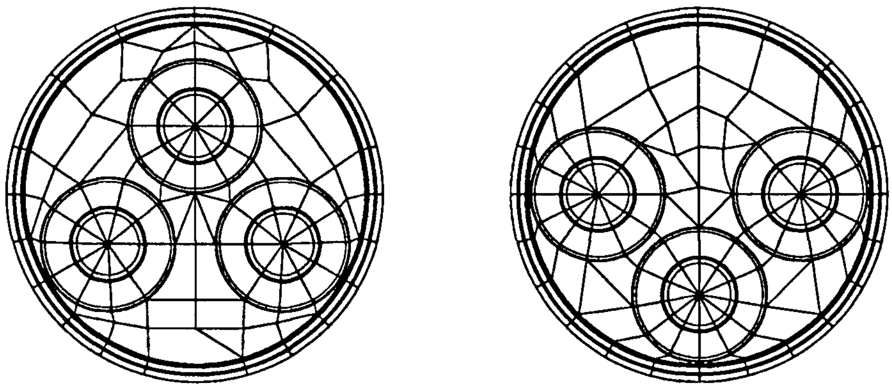

(a) triangle arrangement (b) cradle arrangement
Figure 6.5: Meshes for the PT cables at 6kHz

found with the analytical formulas[23]. Large differences are observed between the results from FEM and those formulas at high frequencies. The maximum differences are 88% in $[R]$ and 68% in $[L]$ from 1Hz to 1MHz.

As mentioned earlier in this section, the formulas ignore the influence of non-current carrying conductors on the field distributions inside the pipe and within the pipe conductor. To study this influence, a $1+j0$ A loop current is assumed between the sheath of the upper SC cable and the pipe. $|A|$ distributions caused by the loop current with or without two lower cables are plotted for 60Hz and 6kHz in Fig. 6.6. The corresponding $|J|$ distributions on the inner surface of the pipe are given in Fig. 6.7. The A contour lines represent the magnetic flux lines[34]. It can be seen in Fig. 6.6 that the distortion of the $|A|$ distribution caused by the presence of the two lower cables is severe at 6kHz but not severe at 60Hz. Similarly, the $|J|$ distribution at 6kHz on the inner surface of the pipe is altered greatly near the two lower cables if the two cables are present, while at 60Hz the $|J|$ distribution is only slightly affected by the lower cables. As reflected in the impedances in Tab.6.5 and Tab.6.6, the differences between the results from FEM and those from the analytical formulas are small at 60Hz ($\leq 3.1\%$) and large at 6kHz ($\leq 26.9\%$).

Table 6.5: $[Z_{AA}]$ and $[Z_{BB}]([Z_{CC}])$ of the PT cable with a triangle arrangement

f (Hz)			R (Ω/km) R_{11}	R_{12}	R_{22}	L (mH/km) L_{11}	L_{12}	L_{22}
60	$[Z_{AA}]$	FEM	0.282226	0.260819	0.662920	1.01507	0.86707	0.86545
		ana.	0.275526	0.254153	0.656159	1.03926	0.89132	0.88969
	$[Z_{BB}]$	FEM	0.285957	0.264551	0.666666	1.04822	0.90023	0.89862
		ana.	0.279190	0.257818	0.659823	1.07678	0.92884	0.92721
600	$[Z_{AA}]$	FEM	0.975600	0.916694	1.31873	0.48853	0.36789	0.36628
		ana.	0.908456	0.849402	1.25125	0.53731	0.41660	0.41498
	$[Z_{BB}]$	FEM	1.01266	0.953773	1.35584	0.50442	0.38378	0.38216
		ana.	0.977012	0.917958	1.31981	0.55370	0.43298	0.43137
6000	$[Z_{AA}]$	FEM	3.20001	3.00974	3.40539	0.29346	0.18268	0.18108
		ana.	3.20516	3.01413	3.40962	0.36005	0.24922	0.24762
	$[Z_{BB}]$	FEM	3.53022	3.33996	3.73563	0.29957	0.18879	0.18719
		ana.	3.89726	3.70623	4.10172	0.34546	0.23464	0.23304
60000	$[Z_{AA}]$	FEM	11.9585	10.6357	10.7013	0.23325	0.12740	0.12666
		ana.	12.4560	11.1361	11.2030	0.29353	0.18764	0.18691
	$[Z_{BB}]$	FEM	16.3469	15.0241	15.0897	0.22250	0.11665	0.11591
		ana.	16.3205	15.0007	15.0675	0.25717	0.15128	0.15055
600000	$[Z_{AA}]$	FEM	42.6742	38.1846	38.1927	0.20765	0.10516	0.10516
		ana.	41.3592	36.8655	36.8741	0.26805	0.16552	0.16552
	$[Z_{BB}]$	FEM	76.1295	71.6399	71.6480	0.18052	0.07803	0.07803
		ana.	56.6433	52.1496	52.1582	0.22257	0.12004	0.12004

Table 6.6: $[Z_{AB}]([Z_{AC}])$ and $[Z_{BC}]$ of the PT cable with a triangle arrangement

f (Hz)			R (Ω/km) R_{11}	R_{12}	R_{21}	R_{22}	L (mH/km) L_{11}	L_{12}	L_{21}	L_{22}
60	$[Z_{AB}]$	FEM	0.2498	0.2498	0.2498	0.2498	0.6857	0.6857	0.6857	0.6858
		ana.	0.2493	0.2493	0.2493	0.2493	0.6824	0.6824	0.6824	0.6824
	$[Z_{BC}]$	FEM	0.2479	0.2479	0.2479	0.2479	0.6470	0.6470	0.6470	0.6470
		ana.	0.2482	0.2482	0.2482	0.2482	0.6396	0.6396	0.6396	0.6396
600	$[Z_{AB}]$	FEM	0.7763	0.7764	0.7763	0.7764	0.2357	0.2357	0.2357	0.2357
		ana.	0.7611	0.7611	0.7611	0.7611	0.2357	0.2357	0.2357	0.2357
	$[Z_{BC}]$	FEM	0.7529	0.7528	0.7528	0.7528	0.2055	0.2055	0.2055	0.2055
		ana.	0.7425	0.7425	0.7425	0.7425	0.1988	0.1988	0.1988	0.1988
6000	$[Z_{AB}]$	FEM	2.506	2.506	2.506	2.506	0.0947	0.0947	0.0947	0.0947
		ana.	2.184	2.184	2.184	2.184	0.1069	0.1069	0.1069	0.1069
	$[Z_{BC}]$	FEM	2.372	2.372	2.372	2.372	0.0722	0.0722	0.0722	0.0722
		ana.	2.010	2.010	2.010	2.010	0.0782	0.0782	0.0782	0.0782
60000	$[Z_{AB}]$	FEM	8.729	8.729	8.729	8.729	0.0466	0.0466	0.0466	0.0466
		ana.	6.283	6.283	6.283	6.283	0.0711	0.0711	0.0711	0.0711
	$[Z_{BC}]$	FEM	7.696	7.696	7.696	7.696	0.0282	0.0282	0.0282	0.0282
		ana.	5.428	5.428	5.428	5.428	0.0474	0.0474	0.0474	0.0474
600000	$[Z_{AB}]$	FEM	33.58	33.58	33.58	33.58	0.0283	0.0283	0.0283	0.0283
		ana.	18.98	18.98	18.98	18.98	0.0604	0.0604	0.0604	0.0604
	$[Z_{BC}]$	FEM	25.92	25.92	25.92	25.92	0.0136	0.0136	0.0136	0.0136
		ana.	15.86	15.86	15.86	15.86	0.0386	0.0386	0.0386	0.0386

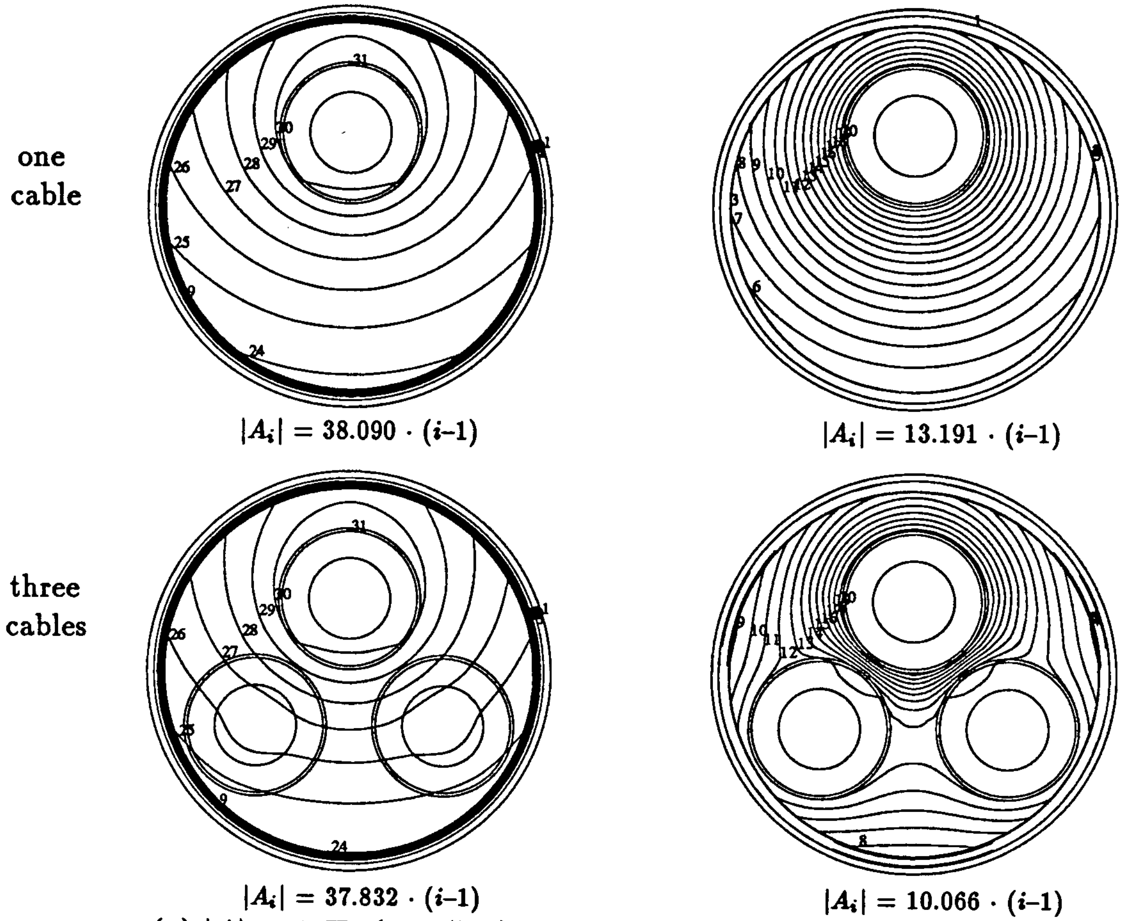

(a) $|A|$ at 60Hz (μsV/km) (b) $|A|$ at 6kHz (μsV/km)

Figure 6.6: $|A|$ distributions caused by the loop current at 60Hz and 6kHz

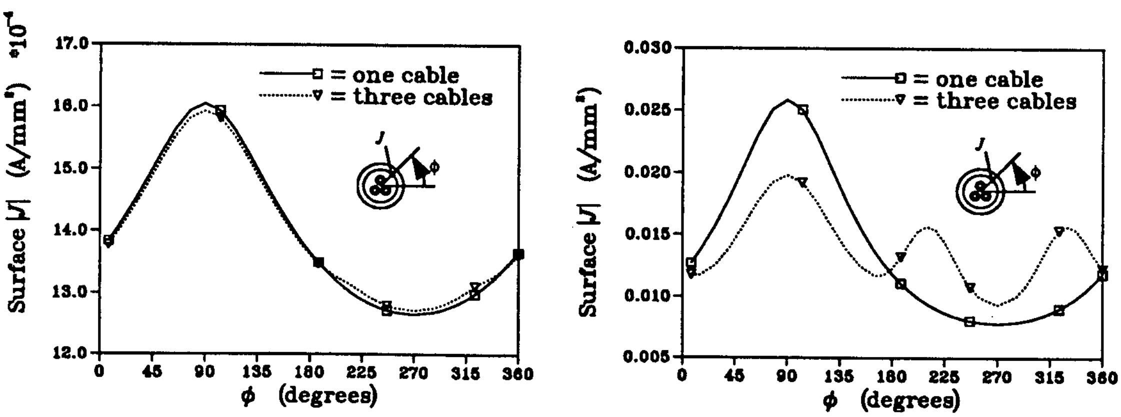

(a) surface $|J|$ at 60Hz (b) surface $|J|$ at 6kHz

Figure 6.7: $|J|$ on the inner surface of the pipe caused by the loop current

If only the upper cable is in the pipe, the maximum differences between the results from FEM and those from the formulas will be 15.79% in $[R]$ and 4.54% in $[L]$ from 1Hz to 1MHz. By decreasing the conductor radii of SC cables, the distances between the cables and the pipe will be increased, which is likely to decrease the errors. As a test case, if r_{B_1}=15mm, r_{A_2}=20mm, r_{B_2}=23mm, and r_{A_3}=25mm for the PT cable in Fig. 6.4(b) with the other parameters remaining the same, the maximum differences between the results from FEM and those from the formulas will be 13.46% in $[R]$ and 24.18% in $[L]$ from 1Hz to 1MHz. A similar PT cable was studied in reference[42]. The distances between the SC cables and the pipe in that case are larger than those in Fig. 6.4, but smaller than in the above test case. Accordingly, the differences between the results from FEM and those from the formulas lie also in the middle.

From the above discussions, it is concluded that the formulas for the impedance calculation of PT cables give accurate results in the low frequency range. They yield reasonably accurate results in the high frequency range if the cable dimensions are small compared with the dimension of the pipe and if the cables and the pipe are not too close to each other.

For the cradle arrangement, the impedances are listed in Tab.6.7 and Tab.6.8 with $[Z_{AA}]=[Z_{CC}]$ and $[Z_{AB}]=[Z_{BC}]$. The maximum differences between the results from FEM and those from the formulas are 81% in $[R]$ and 72% in $[L]$ from 1Hz to 1MHz.

6.3.2 The $[C]$ calculation of PT cables

$[C]$ matrices for the two arrangements are given in Tab.6.9 and Tab.6.10, respectively. They are calculated with FEM and with the analytical formulas[23]. Both the energy method and the surface charge method discussed in Section 5.3 are used to calculate the capacitances. ϵ_r=1 is used for all the regions. The meshes are similar to the ones in Fig. 6.5 except that the conductor regions are removed.

Table 6.7: $[Z_{AA}]([Z_{CC}])$ and $[Z_{BB}]$ of the PT cable with a cradle arrangement

f (Hz)			R (Ω/km) R_{11}	R_{12}	R_{22}	L (mH/km) L_{11}	L_{12}	L_{22}
60	$[z_{AA}]$	FEM	0.285638	0.264232	0.666324	1.04983	0.90185	0.90024
		ana.	0.279190	0.257818	0.659823	1.07678	0.92884	0.92721
	$[z_{BB}]$	FEM	0.287547	0.266144	0.668125	1.04277	0.89478	0.89317
		ana.	0.279190	0.257818	0.659823	1.07678	0.92884	0.92721
600	$[z_{AA}]$	FEM	1.01671	0.957819	1.35986	0.50716	0.38652	0.38491
		ana.	0.977012	0.917958	1.31981	0.55370	0.43298	0.43137
	$[z_{BB}]$	FEM	1.04002	0.981136	1.38306	0.49151	0.37087	0.36926
		ana.	0.977012	0.917958	1.31981	0.55370	0.43298	0.43137
6000	$[z_{AA}]$	FEM	3.65653	3.46628	3.86192	0.29510	0.18432	0.18272
		ana.	3.89726	3.70623	4.10172	0.34546	0.23464	0.23304
	$[z_{BB}]$	FEM	3.56767	3.37744	3.77298	0.27689	0.16611	0.16451
		ana.	3.89726	3.70623	4.10172	0.34546	0.23464	0.23304
60000	$[z_{AA}]$	FEM	16.2286	14.9059	14.9714	0.21712	0.11126	0.11053
		ana.	16.3205	15.0007	15.0675	0.25717	0.15128	0.15055
	$[z_{BB}]$	FEM	14.9878	13.6651	13.7305	0.20428	0.09843	0.09769
		ana.	16.3205	15.0007	15.0675	0.25717	0.15128	0.15055
600000	$[z_{AA}]$	FEM	73.0357	68.5463	68.5544	0.17656	0.07407	0.07407
		ana.	56.6433	52.1496	52.1582	0.22257	0.12004	0.12004
	$[z_{BB}]$	FEM	64.4238	59.9349	59.9430	0.16819	0.06570	0.06570
		ana.	56.6433	52.1496	52.1582	0.22257	0.12004	0.12004

Table 6.8: $[Z_{AB}]([Z_{BC}])$ and $[Z_{AC}]$ of the PT cable with a cradle arrangement

f (Hz)			R (Ω/km) R_{11}	R_{12}	R_{21}	R_{22}	L (mH/km) L_{11}	L_{12}	L_{21}	L_{22}
60	$[z_{AB}]$	FEM	0.2513	0.2513	0.2513	0.2513	0.7003	0.7003	0.7003	0.7003
		ana.	0.2508	0.2508	0.2508	0.2508	0.6981	0.6981	0.6981	0.6981
	$[z_{AC}]$	FEM	0.2446	0.2446	0.2446	0.2446	0.6115	0.6115	0.6115	0.6115
		ana.	0.2461	0.2461	0.2461	0.2461	0.5975	0.5975	0.5975	0.5975
600	$[z_{AB}]$	FEM	0.7972	0.7972	0.7972	0.7972	0.2426	0.2426	0.2426	0.2426
		ana.	0.7855	0.7855	0.7855	0.7855	0.2429	0.2429	0.2429	0.2429
	$[z_{AC}]$	FEM	0.7149	0.7149	0.7149	0.7149	0.1845	0.1845	0.1845	0.1845
		ana.	0.7071	0.7071	0.7071	0.7071	0.1689	0.1689	0.1689	0.1689
6000	$[z_{AB}]$	FEM	2.663	2.663	2.663	2.663	0.0940	0.0940	0.0940	0.0940
		ana.	2.351	2.351	2.351	2.351	0.1046	0.1046	0.1046	0.1046
	$[z_{AC}]$	FEM	2.218	2.218	2.218	2.218	0.0635	0.0635	0.0635	0.0635
		ana.	1.759	1.759	1.759	1.759	0.0622	0.0622	0.0622	0.0622
60000	$[z_{AB}]$	FEM	9.605	9.605	9.605	9.605	0.0407	0.0407	0.0407	0.0407
		ana.	6.832	6.832	6.832	6.832	0.0651	0.0651	0.0651	0.0651
	$[z_{AC}]$	FEM	7.024	7.024	7.024	7.024	0.0218	0.0218	0.0218	0.0218
		ana.	4.502	4.502	4.502	4.502	0.0374	0.0374	0.0374	0.0374
600000	$[z_{AB}]$	FEM	35.39	35.39	35.39	35.39	0.0208	0.0208	0.0208	0.0208
		ana.	20.51	20.51	20.51	20.51	0.0534	0.0534	0.0534	0.0534
	$[z_{AC}]$	FEM	21.59	21.59	21.59	21.59	0.0094	0.0094	0.0094	0.0094
		ana.	12.93	12.93	12.93	12.93	0.0302	0.0302	0.0302	0.0302

Table 6.9: $[C]$ of the PT cable with the triangle arrangement (μF/km)

$[C]$ found with FEM using energy method

0.109652	-0.109652	0	0	0	0
-0.109652	0.243091	0	-0.040218	0	-0.040218
0	0	0.109652	-0.109652	0	0
0	-0.040218	-0.109652	0.342047	0	-0.014692
0	0	0	0	0.109652	-0.109652
0	-0.040218	0	-0.014692	-0.109652	0.342052

$[C]$ found with FEM using surface charge method

0.109442	-0.109442	0	0	0	0
-0.109592	0.243030	0	-0.040217	0	-0.040217
0	0	0.109442	-0.109442	0	0
0	-0.040217	-0.109593	0.341983	0	-0.014692
0	0	0	0	0.109442	-0.109442
0	-0.040217	0	-0.014692	-0.109593	0.341988

$[C]$ found with analytical formulas

0.109795	-0.109795	0	0	0	0
-0.109795	0.209431	0	-0.039429	0	-0.039429
0	0	0.109795	-0.109795	0	0
0	-0.039429	-0.109795	0.243418	0	-0.022992
0	0	0	0	0.109795	-0.109795
0	-0.039429	0	-0.022992	-0.109795	0.243418

Table 6.10: $[C]$ of the PT cable with the cradle arrangement (μF/km)

$[C]$ found with FEM using energy method

0.109653	-0.109653	0	0	0	0
-0.109653	0.348885	0	-0.053153	0	-0.007603
0	0	0.109651	-0.109651	0	0
0	-0.053153	-0.109651	0.386509	0	-0.053166
0	0	0	0	0.109653	-0.109653
0	-0.007603	0	-0.053166	-0.109653	0.348895

$[C]$ found with FEM using surface charge method

0.109442	-0.109442	0	0	0	0
-0.109593	0.348820	0	-0.053152	0	-0.007603
0	0	0.109440	-0.109440	0	0
0	-0.053152	-0.109590	0.386443	0	-0.053165
0	0	0	0	0.109442	-0.109442
0	-0.007603	0	-0.053165	-0.109593	0.348831

$[C]$ found with analytical formulas

0.109795	-0.109795	0	0	0	0
-0.109795	0.243352	0	-0.057283	0	-0.007962
0	0	0.109795	-0.109795	0	0
0	-0.057283	-0.109795	0.267446	0	-0.057283
0	0	0	0	0.109795	-0.109795
0	-0.007962	0	-0.057283	-0.109795	0.243352

6.4 [Z] and [C] Calculations of Sector-Shaped Cables

6.4.1 The [Z] calculation of sector-shaped cables

There is no analytical formula for the impedance calculation of sector-shaped cables of the type on the right in Fig. 1.1(a). The sheath indicated in that figure may or may not exist. For a sector-shaped cable with a sheath, Ametani suggested that its impedances can be calculated approximately with the formulas for PT cables[40]. If L_C and S_C represent the contour length and cross-section area of a sector-shaped core conductor in Fig. 1.1(a), respectively, the conductor can be transformed into an equivalent circular conductor with its outer and inner radii as[40]

$$\text{outer radius} \qquad r_B = \frac{L_C}{2\pi} \tag{6.2}$$

$$\text{inner radius} \qquad r_A = \sqrt{r_B^2 - \frac{S_C}{\pi}} \tag{6.3}$$

Reference [40] did not mention, however, how to determine the position of the equivalent conductor inside the sheath.

The impedances of the sector-shaped cable in Fig. 6.8(a) are calculated with FEM and with the analytical formulas for PT cables using the equivalent radii. For one sector-shaped conductor, S_C=300mm^2 and L_C=70.834mm, with the equivalent radii being r_A=5.622mm and r_B=11.274mm. It is assumed that the three equivalent circular conductors are 13.1mm away from the center of the cable. The sheath is used as the return path and the earth is not considered. A=0 is assumed on the boundary located at r_4 in Fig. 6.8(a). The FEM mesh around the cable at 60kHz is plotted in Fig. 6.8(b).

The impedances of the cable are listed in Tab.6.11. Due to symmetry, Z_{11}=Z_{22}=Z_{33} and Z_{12}=Z_{13}=Z_{23}. "app" in the table represents the results found with the approximate formulas for PT cables using equivalent radii. For a loop current $1+j0$ A between the upper conductor and the sheath, with the upper conductor current being 1 A, the $|A|$

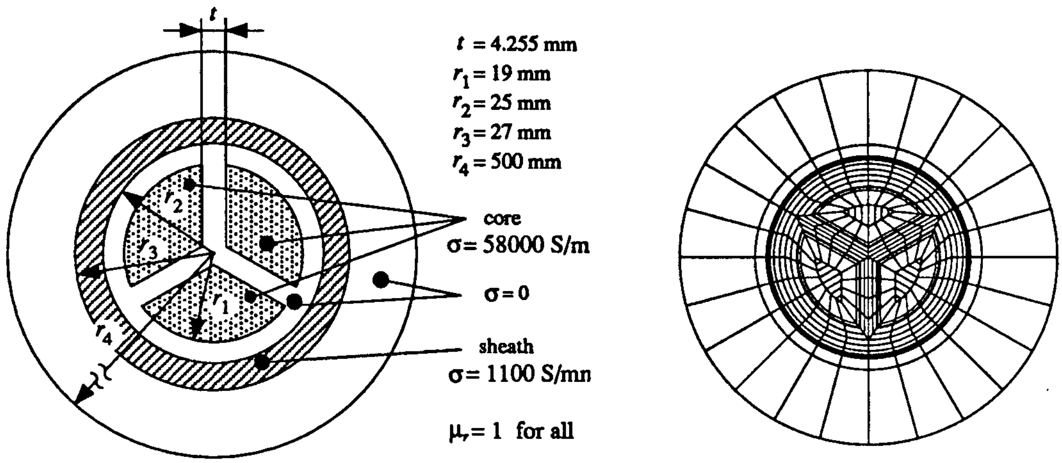

(a) cable data (b) FEM mesh around cable at 60kHz

Figure 6.8: A sector-shaped cable

distributions at 60Hz and 60kHz are given in Fig. 6.9(a) and (b), respectively. The plotting area is 100mm by 100mm.

Table 6.11: $[Z]$ of the sector-shaped cable

f (Hz)		R (Ω/km)		L (μH/km)	
		R_{11}	R_{12}	L_{11}	L_{12}
6	FEM	2.84006	2.78246	232.020	40.4454
	app	2.83996	2.78239	196.081	25.0563
60	FEM	2.84987	2.78317	220.673	40.1914
	app	2.84334	2.78105	191.259	27.3958
600	FEM	2.96756	2.78308	156.797	35.7225
	app	2.93723	2.75504	164.736	36.4771
6000	FEM	3.52505	2.69462	120.400	38.3245
	app	3.52328	2.58640	125.467	47.2753
60000	FEM	5.15051	2.88824	105.090	40.6921
	app	5.89100	2.22645	108.540	52.1332
600000	FEM	15.9166	8.82314	99.0031	38.0609
	app	18.8742	6.42831	100.191	51.1033

The results show that in the low frequency range the differences in $[R]$ between FEM and the formulas are very small because the equivalent circular conductor has the same cross-section area as a sector-shaped conductor. The differences in $[L]$, however, are very large at low frequencies because the magnetic field is not confined within the cable. This is clearly indicated by the $|A|$ distribution at 60Hz in Fig. 6.9(a). In the high frequency range, large differences in $[R]$ and in L_{12} can be observed, while the differences in L_{11}

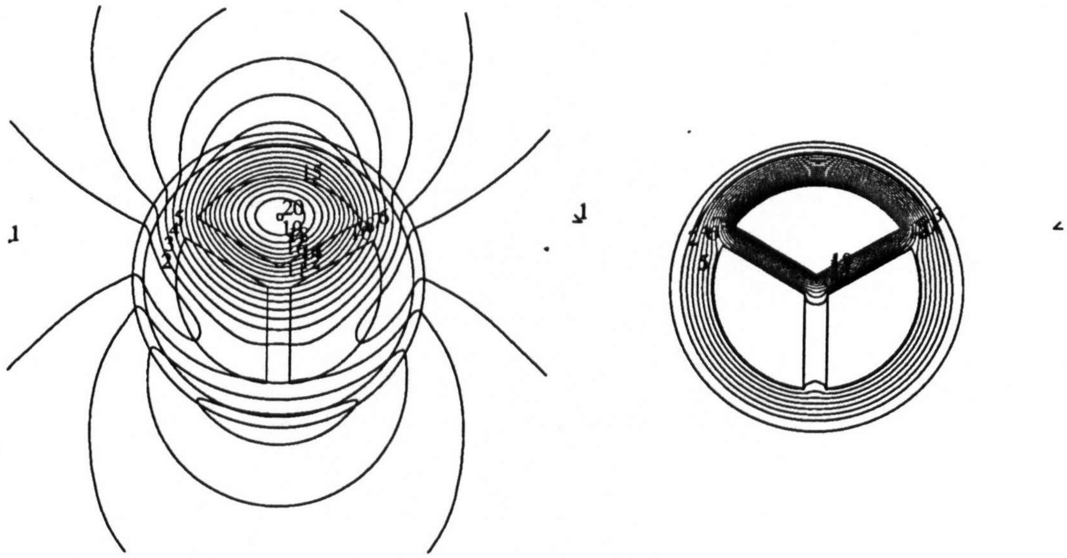

$|A_i| = 1.8777 + 14.298\cdot (i\text{–}1)$ $|A_i| = 0.04552 + 5.7462\cdot (i\text{–}1)$

(a) $|A|$ at 60Hz (μsV/km) (b) $|A|$ at 60kHz (μsV/km)

Figure 6.9: $|A|$ distribution in the sector-shaped cable caused by the loop current

become very small. The magnetic field becomes confined within the cable as shown by the $|A|$ distribution at 60kHz in Fig. 6.9(b). The maximum differences are 41.25% in $[R]$ and 62.11% in $[L]$ from 1Hz to 1MHz.

If the sheath is made of steel with high permeability μ_r, the magnetic field will be confined within the cable even at low frequencies, as seen in Fig. 6.6(a) in the preceding section. The formulas may give reasonably accurate results for $[L]$ in the low frequency range as well. If μ_r=500 for the sheath, the difference in $[L]$ between FEM and the formulas is less than 5% if the frequency is less than 2kHz, and the maximum differences are 23.86% in $[R]$ and 17.57% in $[L]$ from 1Hz to 1MHz.

6.4.2 The $[C]$ calculation of sector-shaped cables

Capacitances of the cable are calculated with FEM and with the formula for PT cables. The results are listed in Tab.6.12 for ϵ_r=1. If the potential of the upper conductor is 1V and the other conductors and the sheath have zero potentials, the potential distribution

Table 6.12: $[C]$ of the sector-shaped cable (μF/km)

method	$C_{11}(C_{22},C_{33})$	$C_{12}(C_{13},C_{23})$
FEM (energy method)	0.147049	-0.0401938
FEM (surface charge method)	0.147323	-0.0402814
analytical formula	0.181528	-0.0620687

found with FEM is plotted in Fig. 6.10. Fringe effects around the corners of the upper conductor can be observed. Because of numerical round-off errors, ϕ_i given in Fig. 6.10 starts from -0.000003 instead of zero.

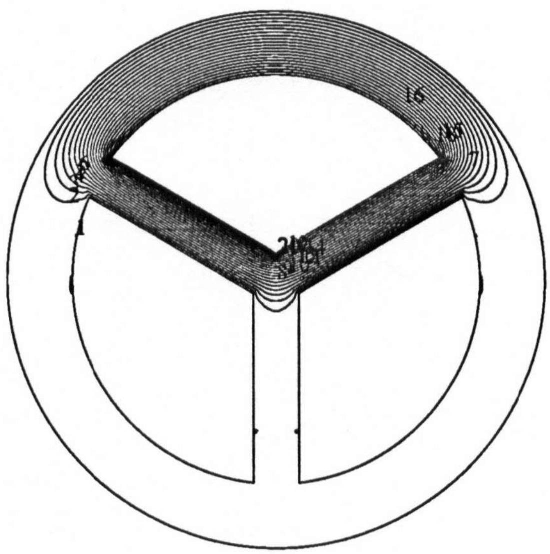

$\phi_i = -0.000003 + 0.05\cdot (i-1)$ V

Figure 6.10: Potential distribution in the sector-shaped cable

6.5 The Calculation of Internal Resistance of Stranded Conductors

Stranded conductors are used for overhead transmission lines. In such lines, the external inductance is much larger than the internal inductance of the conductors. The internal inductance is therefore ignored, or calculated approximately. However, the internal resistance of the conductors is of great importance. By ignoring the spiralling effect, the strands of a stranded conductor can be assumed as parallel circular subconductors. With such an assumption, analytical formulas can be derived for the calculation of the internal resistance of stranded conductors.

Galloway, Shorrocks, and Wedepohl derived the following formula in 1964 for the internal resistance in the high frequency range[4]

$$R_C = \frac{K_f}{\pi(2+n)r\delta\sigma} \tag{6.4}$$

where n is the number of the outer strands, r is the radius of the outer strands, δ is the real penetration depth defined in (3.45), σ is the conductivity of the stranded conductor, and K_f=2.25 is a factor found from measurements in an electrolytic tank. The formula shall be called the GSW formula for simplicity. Borges da Silva suggested in 1979 that a stranded conductor could be replaced with a circular conductor having an equivalent radius[21]. The internal resistance can then be calculated with the formula for the impedance calculation of circular conductors, using the equivalent radius given as

$$r_{eq} = r_e\left(0.92122679 - \frac{n}{4.3856939n^2 - 2.3071869n - 1.2479854}\right) \tag{6.5}$$

where r_e is the outer radius of the stranded conductor. n is the same as in (6.4). This method shall be called Borges da Silva's formula.

Arizon *et al* applied the conductor subdivision method to calculate the internal impedances of stranded conductors in 1987[38]. In that paper differences were reported between the results from the subdivision method and those from the GSW formula, which become small if K_f=1.6 is used in the formula instead of K_f=2.25.

With the assumption that the strands are parallel, FEM can be applied to the calculation of internal resistance of stranded conductors. A two-layer stranded conductor is given in Fig. 6.11(a). It is assumed that the conductor is surrounded by the air. A circular boundary away from the conductor is set up, with A=0 on the boundary. The real part of the impedance for such a single conductor system would be the internal resistance of the conductor. Due to symmetry, only one twelfth of the conductor is used in the FEM solution, as shown in Fig. 6.11(b). The FEM mesh around the conductor at 60kHz is plotted in Fig. 6.11(c).

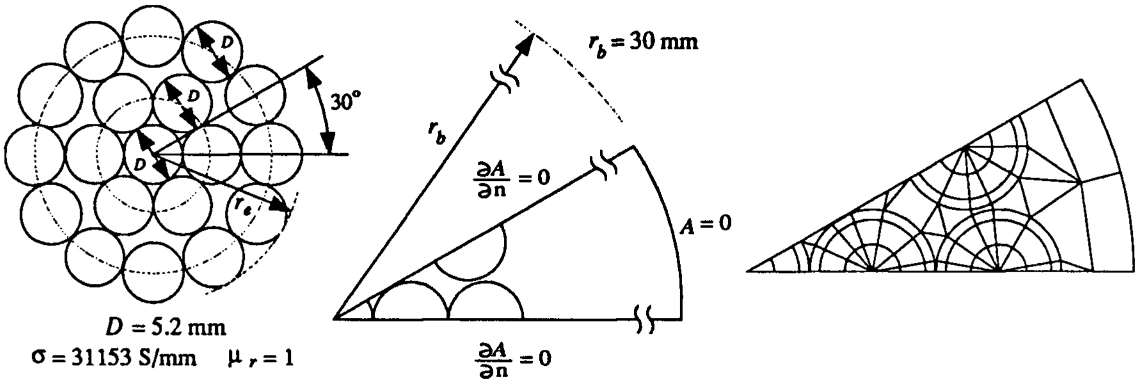

(a) data (b) solution region (c) FEM mesh at 60kHz (partial)

Figure 6.11: A two-layer stranded conductor

The internal resistance of the conductor in Fig. 6.11 is given in Tab.6.13. The maximum differences between the results from FEM and those from the other methods are

Table 6.13: The internal resistance of the two-layer stranded conductor

f (kHz)	R_C (Ω/km) FEM	GSW formula K_f=2.25	GSW formula K_f=1.6	subdivision method	Borges da Silva's formula
43	1.0446	1.4524	1.0328	1.3479	1.0215
80	1.4160	1.9811	1.4088	1.6305	1.3864
100	1.5905	2.2149	1.5751	1.8187	1.5479
130	1.7951	2.5254	1.7959	2.1126	1.7622
max diff with FEM		40.68%	1.13%	29.04%	2.68%

given at the bottom of Tab.6.13. With r_e=13mm and n=12, r_{eq}=11.7171mm is found from (6.5). It can be seen that differences between FEM and Borges da Silva's formula are small. There are large differences between FEM and the GSW formula with K_f=2.25. If K_f=1.6 is used in the GSW formula, the differences between FEM and the formula become insignificant, as shown in Tab.6.13.

If the current in the stranded conductor is 1 A, the $|J|$ distribution at 60Hz and 60kHz are plotted in Fig. 6.12. At 60Hz the currents are almost evenly distributed over

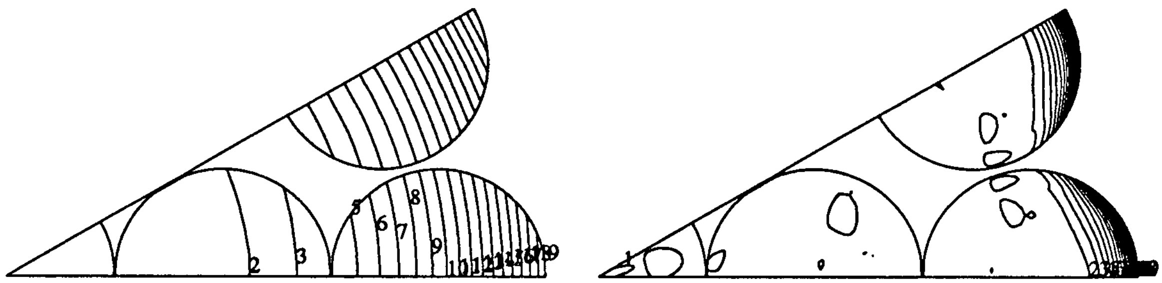

$|J_i| = 2455.8 + 8.21\cdot(i\text{–}1)$ $\qquad$ $|J_i| = 3520.7\cdot(i\text{–}1)$

(a) $|J|$ at 60Hz (A/m^2) $\qquad$ (b) $|J|$ at 60kHz (A/m^2)

Figure 6.12: $|J|$ distribution in the stranded conductor

the conductor, while at 60kHz a strong skin effect can be observed.

If the stranded conductor in Fig. 6.11(a) has only one layer, the corresponding internal resistance is given in Tab.6.14, for n=6, r_e=7.8mm, and r_{eq}=6.8578mm. The differences

Table 6.14: The internal resistance of the one-layer stranded conductor

f (kHz)	R_C (Ω/km)				
	FEM	GSW formula K_f=2.25	GSW formula K_f=1.6	subdivision method	Borges da Silva's formula
20	1.2436	1.7335	1.2327	1.7122	1.2246
43	1.7882	2.5418	1.8075	1.8466	1.7688
80	2.4094	3.4669	2.4654	2.4815	2.3920
100	2.7013	3.8761	2.7564	2.8160	2.6677
130	3.0466	4.4195	3.1427	3.2965	3.0338
max diff with FEM		45.06%	3.15%	37.68%	1.53%

are very small among the results of FEM, Borges da Silva's formula, and the GSW formula with K_f=1.6. Good agreement is observed between FEM and the conductor subdivision method for the listed frequencies, except at 20kHz. For three-layer and four-layer stranded conductors with the same D as in Fig. 6.11(a), n will be 18 and 24, respectively, and r_e will be 18.2mm and 23.4mm, respectively, with r_{eq}= 16.5286mm for the three-layer stranded conductor and r_{eq}= 21.3293mm for the four-layer stranded conductor. The internal resistance is listed in Tab.6.15 and Tab.6.16, respectively.

Table 6.15: The internal resistance of the three-layer stranded conductor

f (kHz)	R_C (Ω/km) FEM	GSW formula K_f=2.25	GSW formula K_f=1.6	Borges da Silva's formula
20	0.50658	0.69338	0.49307	0.49425
60	0.87271	1.2010	0.85403	0.84906
100	1.1174	1.5505	1.1025	1.0934
140	1.3169	1.8345	1.3045	1.2920
180	1.4950	2.0802	1.4792	1.4637
220	1.6610	2.2997	1.6353	1.6172
max diff with FEM		39.30%	2.67%	2.71%

Table 6.16: The internal resistance of the four-layer stranded conductor

f (kHz)	R_C (Ω/km) FEM	GSW formula K_f=2.25	GSW formula K_f=1.6	Borges da Silva's formula
20	0.39099	0.53337	0.37929	0.38133
60	0.67642	0.92383	0.65694	0.65630
100	0.86673	1.1927	0.84811	0.84563
140	1.0229	1.4112	1.0035	0.99951
180	1.1627	1.6001	1.1379	1.1326
220	1.2934	1.7690	1.2580	1.2515
max diff with FEM		37.95%	2.99%	3.24%

It should be noted that even though the GSW formula with a factor of 2.25 does not agree with the other methods, it does seem to come closer to field tests[20]. The reason may be that the factor 2.25 takes the spiralling effect into account.

6.6 Summary

In this chapter FEM is applied to the parameter calculation of buried or tunnel installed multiphase cables, of three-phase PT cables and sector-shaped cables, and of stranded conductors. The earth region reduction technique discussed in Chapter 4 is also used in the impedance calculation of buried or tunnel installed cables.

The results show that for typical earth resistivities Pollaczek's formula gives reasonably accurate self and mutual impedances for multiphase buried cables, and for tunnel installed cables using approximate inner earth radii. Good agreement between the proposed technique and the conventional FEM are shown by the results. For PT cables, the analytical formulas may introduce errors at high frequencies because the influence of non-current carrying conductors on the fields inside the pipe and within the pipe conductor are not considered in the formulas. For sector-shaped cables comparisons show that reasonably accurate self and mutual resistances can be obtained in the low frequency range with the formulas for PT cables by using equivalent core conductor radii suggested by Ametani. Accurate self and mutual inductances cannot be obtained in the low frequency range with the formulas if the sheath is non-magnetic or if there is no sheath. In the high frequency range, large differences between the results from FEM and those from the formulas for both resistances and inductances are observed. For the internal resistance of stranded conductors, good agreement is obtained among the results from FEM, Borges da Silva's formula, and the GSW formula with K_f=1.6. There is also Good agreement between the results from FEM and those from the conductor subdivision method for a one-layer stranded conductor at $f \geq 43$kHz. With respect to the factor in the GSW formula, good agreement was reported between the GSW formula with K_f=2.25 and field tests[20]. This may be due to the fact that the factor 2.25 takes the spiralling effect into account.

Chapter 7

Conclusions and Recommendations for Future Work

In this thesis, the finite element method (FEM) was applied to the parameter calculation of underground power cables. The parameters most often needed in power system analysis are the series impedances and shunt capacitances. The principal equations describing the quasi-magnetic fields and static electric fields were solved with FEM based on the Galerkin technique. Quadratic isoparametric elements as well as high-order simplex elements were studied. A technique based on the perturbation concept was proposed to reduce the solution region in the earth. The parameters of shallowly buried or tunnel installed multiphase single core (SC) cables, pipe-type (PT) cables, sector-shaped cables, and stranded conductors were calculated with FEM. The major conclusions are:

1. The J_S method and the loss-energy method derived in the thesis for the $[Z]$ calculation from the field solution gave the same results. The loss-energy method is time-consuming and requires a complete field solution. Much less computation is needed with the J_S method, and a complete field solution is not required.

2. Quadratic isoparametric elements proved to be more efficient than high-order simplex elements, in both the impedance calculation and the capacitance calculation. For the same error tolerance, isoparametric elements can have larger span angles. The low accuracy of simplex elements for large span angles cannot be improved by increasing the order of polynomials of the elements. Fewer elements are needed in meshing a circular region with isoparametric elements.

3. Accurate impedances could be obtained for deeply buried SC cables with the conventional FEM if the field truncation boundary is at least $3\delta_e$ away from the cables ($r_b \geq 3\delta_e$), and if the earth is divided with the pattern 10^n, $10^{n+\frac{1}{3}}$, $10^{n+\frac{2}{3}}$, 10^{n+1} in each decade in the radial direction. For shallowly buried SC cables, the iterative results showed that $r_b \geq 12\delta_e$ is required to make the differences in $[Z]$ from two consecutive steps less than 0.5%.

4. Good agreement was obtained between the proposed technique and the conventional FEM for shallowly buried SC cables. As shown in Section 4.5.2, for r_b=5m, with ρ_e=100Ωm and with r_e varying between 24mm and 1m, the maximum errors with the proposed technique are less than 8% in $[R]$ and less than 2% in $[L]$. The earth solution region is reduced significantly with the proposed technique in the low frequency range, and CPU time is saved if partial earth return currents required for the technique are calculated only once.

5. Comparisons between Pollaczek's formula and the FEM for a single-phase shallowly buried SC cable in Chapter 4 showed that accurate results were obtained with Pollaczek's formula when r_e/δ_e is small. For r_e=24mm, the maximum differences between the results from Pollaczek's formula and from the FEM are less than 1% in $[R]$ if $r_e/\delta_e \leq 0.03$ and in $[L]$ if $r_e/\delta_e \leq 0.095$. For large r_e/δ_e, the differences become large. With typical ranges of ρ_e and r_e, however, the maximum differences between the two approaches from 1Hz to 1MHz are reasonably small. With ρ_e varying between 1000Ωm to 1Ωm and with r_e varying between 24mm to 250mm, the maximum differences are less than 21% in $[R]$ and less than 9% in $[L]$. Results also showed that Pollaczek's formula could be applied to find the impedances of tunnel installed cables as well, if an approximate r_e is used. For typical earth resistivities, Pollaczek's formula gave reasonably accurate self and mutual impedances

for multiphase buried cables, and for tunnel installed cables with an approximate r_e.

6. For a PT cable, the magnetic flux distribution in the pipe and the current density distribution within the pipe conductor are significantly influenced by the presence of non-current carrying conductors at high frequencies. This influence is ignored in approximate formulas, which therefore produce noticeable errors at high frequencies.

7. For a sector-shaped cable with a magnetic sheath, the the analytical formulas suggested by Ametani produce reasonably accurate resistances and inductances in the low frequency range. If the sheath is non-magnetic or nonexistent, then the inductance has a large error. In the high frequency range, these formulas are too inaccurate.

8. For the calculation of the internal resistance of stranded conductors, the spiralling effect was ignored by assuming that all strands are in parallel. Close agreement was obtained among the results from FEM, Borges da Silva's formula, and the GSW formula with K_f=1.6, for stranded conductors with one to four layers. It has been reported, however, that the GSW formula with K_f=2.25 comes closer to field tests. This may be due to the fact that the factor 2.25 takes the spiralling effect into account. There was also good agreement between the results from FEM and those from the conductor subdivision method for a one-layer stranded conductor at $f \geq$43kHz.

9. For the capacitance calculation from the field solution, the energy method is simple and easy to implement. It has less stringent requirements on the mesh and has higher accuracy than the surface charge method. The surface charge method,

however, is faster, and its accuracy can be improved with a finer mesh near the conductor surfaces.

Future research could be conducted in the following areas:

1. The mesh should be automatically generated for cable geometries, for user-friendly interfaces with the FEM. The auto-mesh program developed for this project is not flexible enough, and is incomplete.

2. More field tests are needed to compare the calculated impedances against measured impedances.

3. If the conductance of insulating materials is available from tests and is to be considered as well, then the FEM should be modified to include it.

4. the FEM program could be used as a verification tool for developing simpler approximate formulas for PT cables, sector-shaped cables, and other types of cables.

References

[1] J. R. Carson, "Wave Propagation in Overhead Wires, with Ground Return," *Bell Syst. Tech. Jour.*, vol.5, 1926, pp.539-554.

[2] F. Pollaczek, "Uber das Feld einer unendlich langen wechselstromdurchflossenen Einfachleitung," *E.N.T.*, 1926, Band 3 (Heft 9), pp.339-360.

[3] S.A. Schelkunoff,"The Electromagnetic Theory of Coaxial Transmission Line and Cylindrical Shells," *Bell System Tech. Jour.*, vol.13, 1934, pp.522-579.

[4] R. H. Galloway, W. B. Shorrocks, and L. M. Wedepohl, "Calculation of Electrical Parameters for Short and Long Polyphase Transmission Lines," *Proc. IEE*, vol.111, Dec. 1964, pp.2051-2059.

[5] A. H. Stroud and Don Secrest, *Gaussian Quadrature Formulas.* Prentice-Hall, Inc., Englewood Cliffs, New Jersey, 1966.

[6] L. M. Wedepohl and S. E. T. Mohamed, "Multiconductor Transmission Lines — Theory of Natural Modes and Fourier Integral Applied to Transient Analysis," *Proc. IEE*, vol.116, Sept. 1969, pp.1553-1563.

[7] P. Silvester, "High-Order Polynomial Triangular Finite Elements for Potential Problems," *Int. J. Engng Sci.*, vol.7, 1969, pp.849-861.

[8] J. A. Tegopoulos and E. E. Kriezis, "Eddy Current Distribution in Cylindrical Shells of Infinite Length due to Axial Currents – Part II: Shells of Finite Thickness," *IEEE Trans. on PAS*, vol.PAS-90, May 1971, pp.1287-1294.

[9] E. Comellini, A. Invernizzi, and G. Manzoni, "A Computer Program for Determining Electrical Resistance and Reactance of any Transmission Line," *IEEE Trans. PAS*, vol.PAS-92, Jan./Feb. 1973, pp.308-314.

[10] L. M. Wedepohl and D. J. Wilcox, "Transient Analysis of Underground Power-Transmission Systems — System Model and Wave-Propagation Characteristics," *Proc. IEE*, vol.120, Feb. 1973, pp.253-260.

[11] H. C. Martin and G. F. Carey, *Introduction to Finite Element Analysis.* McGraw-Hill Book Company, 1973.

[12] M. V. K. Chari, "Finite Element Solution of the Eddy-Current Problem in Magnetic Structures," *IEEE Trans. PAS*, vol.PAS-93, Jan. 1974, pp.62-72.

[13] G. W. Brown and R. G. Rocamora, "Surge Propagation in Three-Phase Pipe-Type Cables. Part I – Unsaturated Pipe," *IEEE Trans. PAS*, vol. PAS-95, Jan./Feb. 1976, pp.89-95.

[14] M. V. K. Chari and Z. J. Csendes, "Finite Element Analysis of the Skin Effect in Current Carrying Conductors," *IEEE Trans. on Magnetics*, vol.MAG-13, Sept. 1977, p.1125-1127.

[15] A. Jennings, *Matrix Computation for Engineers and Scientists.* John Wiley & Sons Ltd., 1977.

[16] E. M. Deeley and E. E. Okon, " An Integral Method for Computing the Inductance and the A.C. Resistance of Parallel Conductors," *Intl. J. Numerical Method Eng.*, vol.12, 1978, pp.625-634.

[17] R. Lucas and S. Talukdar, "Advances in Finite Element Techniques for Calculating Cable Resistances and Inductances," *IEEE Trans. PAS*, vol.PAS-97, May/June 1978, pp.875-883.

[18] L. M. Wedepohl and A. E. Efthymiadis, "Wave Propagation in Transmission Lines over Lossy Ground: a New, Complete Field Solution," *Proc. IEE*, Vol.125, June 1978, pp.505-510.

[19] A. E. Efthymiadis and L. M. Wedepohl, "Propagation Characteristics of Infinitely-Long Single-Conductor Lines by the Complete Field Solution Method," *Proc. IEE*,

Vol.125, June 1978, pp.511-517.

[20] S. Cristina and M. D'Amore, "Propagation on Polyphase Lossy Lines: A New Parameter Sensitivity Model," *IEEE Trans. PAS*, vol.PAS-98, Jan./Feb. 1979, pp.35-44.

[21] J. F. Borges da Silva, "The Electrostatic Field Problem of Stranded and Bundle Conductors Solved by the Multipole Method," *Electricidade*, No.142, Mar./Apr. 1979, pp1-11.

[22] W. T. Weeks, L. L. Wu, M. F. McAllister, and A. Singh, "Resistive and Inductive Skin Effect in Rectangular Conductors," *IBM J. RES. DEVELOP.* vol.23, Nov. 1979, pp652-660.

[23] A. Ametani, "A General Formulation of Impedance of Cables," *IEEE Trans. PAS*, vol.PAS-99, May/June 1980, pp.902-909.

[24] J. M. Schneider and S. J. Salon, "A Boundary Integral Formulation of the Eddy Current Problem," *IEEE Trans. MAG*, vol.MAG-16, Sept. 1980, pp.1086-1088.

[25] W. D. Humpage, K. P. Wong, T. T. Nguyen, and D. Sutanto, "z-Transform Electromagnetic Transient Analysis in Power Systems," *Proc. IEE-C*, Vol.127, Nov. 1980, pp.370-378.

[26] A. Konrad, "The Numerical Solution of Steady-State Skin Effect Problems — An Integrodifferential Approach," *IEEE Trans. MAG*, vol.MAG-17, Jan. 1981, pp.1148-1152.

[27] E. L. Wachspress, "High-Order Curved Finite Elements," *Intl. J. Numerical Method Eng.*, vol.17, 1981, pp.735-745.

[28] A. Konrad, "Integrodifferential Finite Element Formulation of Two Dimensional Steady-State Skin Effect Problems," *IEEE Trans. MAG*, vol.MAG-18, Jan. 1982, pp.284-292.

[29] J. R. Marti, "Accurate Modelling of Frequency-Dependent Transmission Lines in Electromagnetic Transient Simulations," *IEEE Trans. PAS*, vol.PAS-101, Jan. 1982, pp.147-157.

[30] S. J. Salon and J. M. Schneider, "A Hybrid Finite Element-Boundary Integral Formulation of the Eddy Current Problem," *IEEE Trans. MAG*, vol.MAG-18, Mar. 1982, pp.461-466.

[31] J. Weiss and Z. J. Csendes, "A One-Step Finite Element Method for Multiconductor Skin Effect Problems," *IEEE Trans. on PAS*, vol.PAS-101, Oct. 1982, pp.3796-3803.

[32] J. Weiss, V. K. Garg, and E. Sternheim, "Eddy Current Loss Calculation in Multiconductor Systems," *IEEE Trans. MAG*, vol.MAG-19, Sept. 1983, pp.2207-2209.

[33] W. M. Rucker and K. R. Richter, "Calculation of Two-Dimensional Eddy Current Problems with the Boundary Element Method," *IEEE Trans. MAG*, vol.MAG-19, Nov. 1983, pp.2429-2432.

[34] P. P. Silvester and R. L. Ferrari, *Finite Elements for Electrical Engineers.* Cambridge University Press, 1983.

[35] S. J. Salon, "The Hybrid Finite Element-Boundary Element Method in Electromagnetics," *IEEE Trans. MAG*, vol.MAG-21, Sep. 1985, pp.1829-1834.

[36] J. Poltz and E. Kuffel, "Application of Boundary Element Techniques for 2D Eddy-Current Problems," *IEEE Trans. MAG*, vol.MAG-21, Nov. 1985, pp.2254-2256.

[37] P. E. Allaire, *Basics of the Finite Element Method — Solid Mechanics, Heat Transfer, and Fluid Mechanics.* Wm. C. Brown Publishers, Dubuque, Iowa, 1985.

[38] P. de Arizon and H. W. Dommel, "Computation of Cable Impedances Based on Subdivision of Conductors," *IEEE Trans. on Power Delivery*, vol.PWRD-2, Jan. 1987, pp.21-27.

[39] L. Marti, "Simulation of Transients in Underground Cables with Frequency-Dependent Modal Transformation Matrices," *IEEE Trans. on Power Delivery*, vol.PWRD-3, July 1988, pp.1099-1110.

[40] A. Ametani, "Further Improvements of CABLE CONSTANTS and An Investigation of Cable Problems," *EMTP NEWS*, vol.1, No.4, Dec. 1988, pp.4-14.

[41] S. Cristina and M. Feliziani, "A Finite Element Technique for Multiconductor Cable Parameters Calculation," *IEEE Trans. on Magnetics*, vol.MAG-25, July 1989, pp.2986-2988.

[42] Y. Yin and H. W. Dommel, "Calculation of Frequency-Dependent Impedances of Underground Power Cables with Finite Element Method," *IEEE Trans. on Magnetics*, vol.MAG-25, July 1989, pp.3025-3027.

[43] M. Rioual, "Measurements and Computer Simulation of Fast Transients through Indoor and Outdoor Substations," *IEEE Trans. on Power Delivery*, vol.PWRD-5, Jan. 1990, pp.117-123.

[44] A. Konrad and P. Silvester, "Triangular Finite Elements for the Generalized Bessel Equation of Order m," *Int. J. Numer. Meth. Eng.*, vol.7, 1973, pp.43-55.

[45] B. Engquist, A. Greenbaum, and W. D. Murphy, "Global Boundary Conditions and Fast Helmholtz Solvers," *IEEE Trans. on Magnetics*, vol.MAG-25, July 1989, pp.2804-2806.

Appendix A

Integral matrices $[Q^{(1)}]$ and $[T_S]$ of simplex elements

Table A.1: $[Q^{(1)}]$ and $[T_S]$ of the 1st order simplex element

(a) $[Q^{(1)}]$

common denominator = 2

0	symm.	
0	1	
0	-1	1

(b) $[T_S]$

common denominator = 12

2	symm.	
1	2	
1	1	2

Table A.2: $[Q^{(1)}]$ and $[T_S]$ of the 2nd order simplex element

(a) $[Q^{(1)}]$

common denominator = 6

0					
0	8		symm.		
0	-8	8			
0	0	0	3		
0	0	0	-4	8	
0	0	0	1	-4	3

(b) $[T_S]$

common denominator = 180

6					
0	32			symm.	
0	16	32			
-1	0	-4	6		
-4	16	16	0	32	
-1	-4	0	-1	0	6

Table A.3: $[Q^{(1)}]$ and $[T_S]$ of the 3rd order simplex element

(a) $[Q^{(1)}]$

common denominator = 80

0									
0	135					symm.			
0	-135	135							
0	-27	27	135						
0	0	0	-162	324					
0	27	-27	27	-162	135				
0	3	-3	3	0	-3	34			
0	0	0	0	0	0	-54	135		
0	0	0	0	0	0	27	-108	135	
0	-3	3	-3	0	3	-7	27	-54	34

(b) $[T_S]$

common denominator = 6720

76									
18	540					symm.			
18	270	540							
0	-189	-135	540						
36	162	162	162	1944					
0	-135	-189	-54	162	540				
11	0	27	18	36	27	76			
27	-135	-54	270	162	-135	18	540		
27	-54	-135	-135	162	270	0	-189	540	
11	27	0	27	36	18	11	0	18	76

Table A.4: $[Q^{(1)}]$ and $[T_S]$ of the 4th order simplex element

(a) $[Q^{(1)}]$ (common denominator = 1890)

0														
0	3968													
0	-3968	3968												
0	-1440	1440	4632											
0	0	0	-5376	10752								symm.		
0	1440	-1440	744	-5376	4632									
0	640	-640	-1248	1536	-288	3456								
0	0	0	768	-1536	768	-4608	10752							
0	0	0	768	-1536	768	1536	-7680	10752						
0	-640	640	-288	1536	-1248	-384	1536	-4608	3456					
0	-80	80	80	-160	80	240	-160	-160	80	705				
0	0	0	-128	256	-128	-256	256	256	-256	-1232	3456			
0	0	0	96	-192	96	192	-192	-192	192	884	-3680	5592		
0	0	0	-128	256	-128	-256	256	256	-256	-464	1920	-3680	3456	
0	80	-80	80	-160	80	80	-160	-160	240	107	-464	884	-1232	705

(b) $[T_S]$ (common denominator = 56700)

290														
160	2560													
160	1280	2560												
-80	-1280	-960	3168											
160	1280	1280	384	10752								symm.		
-80	-960	-1280	48	384	3168									
0	768	512	-1280	256	64	2560								
-160	256	-256	384	-1536	-768	1280	10752							
-160	-256	256	-768	-1536	384	-256	-1536	10752						
0	512	768	64	256	-1280	256	-256	1280	2560					
-27	0	-112	-80	-160	-12	160	160	-160	-112	290				
-112	512	256	-960	-256	64	1280	1280	256	512	160	2560			
-12	64	64	48	-768	48	-960	384	384	-960	-80	-1280	3168		
-112	256	512	64	-256	-960	512	256	1280	1280	0	768	-1280	2560	
-27	-112	0	-12	-160	-80	-112	-160	160	160	-27	0	-80	160	290

Table A.5: $[Q^{(1)}]$ and $[T_S]$ of the 5th order simplex element

(a) $[Q^{(1)}]$ (common denominator = 290304)

symm.

0																				
0	743750																			
0	-743750	743750																		
0	-405000	405000	1072500																	
0	0	0	-1150000	2300000																
0	405000	-405000	77500	-1150000	1072500															
0	260000	-260000	-523750	587500	-63750	892500														
0	0	0	293750	-587500	293750	-1106250	2512500													
0	0	0	293750	-587500	293750	300000	-1706250	2512500												
0	-260000	260000	-63750	587500	-523750	-86250	300000	-1106250	892500											
0	-98750	98750	237500	-287500	50000	-263125	346875	-121875	38125	577500										
0	0	0	-150000	300000	-150000	212500	-525000	412500	-100000	-818750	2050000									
0	0	0	12500	-25000	12500	112500	-112500	-112500	112500	393750	-1837500	2887500								
0	0	0	-150000	300000	-150000	-100000	412500	-525000	212500	-193750	800000	-1837500	2050000							
0	98750	-98750	50000	-287500	237500	38125	-121875	346875	-263125	41250	-193750	393750	-818750	577500						
0	11850	-11850	-20225	31250	-11025	-4600	-15625	31250	-11025	58725	-62500	-15625	31250	-11850	99402					
0	0	0	20625	-41250	20625	-14375	61250	-79375	32500	-83125	146250	14375	-135000	57500	-188125	577500				
0	0	0	-5000	10000	-5000	30000	-92500	95000	-32500	83125	-177500	1250	197500	-104375	172500	-745625	1282500			
0	0	0	-5000	10000	-5000	-32500	95000	-92500	30000	-104375	197500	1250	-177500	83125	-130625	570000	-1148750	1282500		
0	0	0	20625	-41250	20625	32500	-79375	61250	-14375	57500	-135000	14375	146250	-83125	58750	-272500	570000	-745625	577500	
0	-11850	11850	-11025	31250	-20225	-11025	31250	-15625	-4600	-11850	31250	-15625	-62500	58725	-11902	58750	-130625	172500	-188125	99402

(b) $[T_S]$ (common denominator = 19160064)

symm.

53244																				
45270	563500																			
45270	281750	563500																		
-36720	-367250	-281750	846000																	
34200	392500	392500	-55000	2700000																
-36720	-281750	-367250	113000	-55000	846000															
17730	295250	220750	-516500	195000	-52000	846000														
-37350	3750	-146250	202500	-600000	-210000	202500	2925000													
-37350	-146250	3750	-210000	-600000	202500	-22500	-450000	2925000												
17730	220750	295250	-52000	195000	-516500	108000	-22500	202500	846000											
-880	-152125	-95125	295250	-107500	-1750	-367250	3750	-52500	-55500	563500										
33700	-107500	30000	195000	450000	120000	-55000	-600000	150000	120000	392500	2700000									
24900	-52500	-52500	-22500	150000	-22500	-210000	-450000	-450000	-210000	-146250	-600000	2925000								
33700	30000	-107500	120000	450000	195000	120000	150000	-600000	-55000	30000	450000	-600000	2700000							
-880	-95125	-152125	-1750	-107500	295250	-55500	-52500	3750	-367250	-15750	30000	-146250	392500	563500						
4747	-880	13935	17730	33700	7940	-36720	-37350	24900	7940	45270	34200	-37350	33700	13935	53244					
13935	-95125	-15750	220750	30000	-55500	-281750	-146250	-52500	-1750	281750	392500	3750	-107500	-95125	45270	563500				
7940	-1750	-55500	-52000	120000	108000	113000	-210000	-22500	-52000	-281750	-55000	202500	195000	220750	-36720	-367250	846000			
7940	-55500	-1750	108000	120000	-52000	-52000	-22500	-210000	113000	220750	195000	202500	-55000	-281750	17730	295250	-516500	846000		
13935	-15750	-95125	-55500	30000	220750	-1750	-52500	-146250	-281750	-95125	-107500	3750	392500	281750	-880	-152125	295250	-367250	563500	
4747	13935	-880	7940	33700	17730	7940	24900	-37350	-36720	13935	33700	-37350	34200	45270	4747	-880	17730	-36720	45270	53244

Table A.6: $[Q^{(1)}]$ and $[T_S]$ of the 6th order simplex element

(a) $[Q^{(1)}]$ (common denominator = 92400)

symm.

0																											
0	283176																										
0	-283176	283176																									
0	-208656	208656	517185																								
0	0	0	-500580	1001160																							
0	208656	-208656	-16605	-500580	517185																						
0	176400	-176400	-377640	382320	-4680	552896																					
0	0	0	191160	-382320	191160	-584928	1253664																				
0	0	0	191160	-382320	191160	83808	-752544	1253664																			
0	-176400	176400	-4680	382320	-377640	-51776	83808	-584928	552896																		
0	-97524	97524	235467	-261144	25677	-288828	327780	-68796	29844	359505																	
0	0	0	-128628	257256	-128628	222480	-486864	306288	-41904	-462780	1100736																
0	0	0	-3888	7776	-3888	78408	-78408	-78408	78408	184842	-908496	1447308															
0	0	0	-128628	257256	-128628	-41904	306288	-486864	222480	-95364	365904	-908496	1100736														
0	97524	-97524	25677	-261144	235467	29844	-68796	327780	-288828	13797	-95364	184842	-462780	359505													
0	31752	-31752	-87966	103356	-15390	124488	-159192	50760	-16056	-114102	150552	-67392	39744	-8802	203256												
0	0	0	48114	-96228	48114	-106920	254664	-188568	40824	109350	-268272	250776	-134136	42282	-306180	816480											
0	0	0	3564	-7128	3564	25488	-118800	161136	-67824	23544	30240	-183384	181872	-52272	190728	-863136	1448064										
0	0	0	3564	-7128	3564	-67824	161136	-118800	25488	-52272	181872	-183384	30240	23544	-130032	554040	-1199664	1448064									
0	0	0	48114	-96228	48114	40824	-188568	254664	-106920	42282	-134136	250776	-268272	109350	52488	-253692	554040	-863136	816480								
0	-31752	31752	-15390	103356	-87966	-16056	50760	-159192	124488	-8802	39744	-67392	150552	-114102	-10260	52488	-130032	190728	-306180	203256							
0	-3528	3528	7497	-10332	2835	-3276	10080	-10332	3528	-8631	3276	12852	-10332	2835	24192	-30744	3276	10080	-10332	3528	29946						
0	0	0	-5670	11340	-5670	7992	-26136	28296	-10152	2322	10152	-39528	39312	-12258	-39960	84564	-30024	-55296	62208	-21492	-61056	203256					
0	0	0	-324	648	-324	-3672	19548	-28080	12204	8640	-38448	68364	-55944	17388	49950	-128790	70092	100224	-145314	53838	68634	-309474	597645				
0	0	0	1656	-3312	1656	-6624	6624	6624	-6624	-10296	51984	-83376	51984	-10296	-70056	168408	-98352	-98352	168408	-70056	-66748	305064	-661932	847232			
0	0	0	-324	648	-324	12204	-28080	19548	-3672	17388	-55944	68364	-38448	8640	53838	-145314	100224	70092	-128790	49950	42633	-205794	468288	-661932	597645		
0	0	0	-5670	11340	-5670	-10152	28296	-26136	7992	-12258	39312	-39528	10152	2322	-21492	62208	-55296	-30024	84564	-39960	-16344	84348	-205794	305064	-309474	203256	
0	3528	-3528	2835	-10332	7497	3528	-10332	10080	-3276	2835	-10332	12852	3276	-8631	3528	-10332	10080	3276	-30744	24192	2935	-16344	42633	-66748	68634	-61056	29946

(b) $[T_S]$ (common denominator = 504504000)

symm.

859908																											
955584	10668672																										
955584	5334336	10668672																									
-1022490	-8731800	-6667920	19652220																								
687960	9208080	9208080	-4263840	57970080																							
-1022490	-6667920	-8731800	4711770	-4263840	19652220																						
796320	8844192	6880608	-16369920	8195040	-3769920	25373440																					
-796320	-1251936	-4917024	6894720	-18325440	-3764880	158400	68895360																				
-796320	-4917024	-1251936	-3764880	-18325440	6894720	-480960	-10108800	68895360																			
796320	6880608	8844192	-3769920	8195040	-16369920	5054720	-480960	158400	25373440																		
-353556	-5930820	-4406724	11889585	-6332580	1507815	-16369920	2984040	-1636200	-3298320	19652220																	
726264	-1342656	2413152	2984040	16394400	3392280	158400	-23872320	5054400	3640320	6894720	68895360																
611604	-938952	-938952	-1091070	3576960	-1091070	-6205680	-14735520	-14735520	-6205680	-1091070	-14735520	74212200															
726264	2413152	-1342656	3392280	16394400	2984040	3640320	5054400	-23872320	158400	-482760	12208320	-14735520	68895360														
-353556	-4406724	-5930820	1507815	-6332580	11889585	-3298320	-1636200	2984040	-16369920	1142910	-482760	-1091070	6894720	19652220													
22932	2614032	1604448	-5930820	2488320	-254340	8844192	-1342656	1264896	1444608	-8731800	-1251936	-938952	1220832	-197964	10668672												
-546588	2488320	-592272	-6332580	-8145360	-1398060	8195040	16394400	-4911840	-2531520	-4263840	-18325440	3576960	-4911840	-1398060	9208080	57970080											
-431928	1264896	1220832	-1636200	-4911840	-482760	-480960	5054400	12208320	3640320	-3764880	-10108800	-14735520	5054400	3392280	-4917024	-18325440	68895360										
-431928	1220832	1264896	-482760	-4911840	-1636200	3640320	12208320	5054400	-480960	3392280	5054400	-14735520	-10108800	-3764880	2413152	16394400	-23872320	68895360									
-546588	-592272	2488320	-1398060	-8145360	-6332580	-2531520	-4911840	16394400	8195040	-1398060	-4911840	3576960	-18325440	-4263840	-592272	-8145360	16394400	-18325440	57970080								
22932	1604448	2614032	-254340	2488320	-5930820	1444608	1264896	-1342656	8844192	-197964	1220832	-938952	-1251936	-8731800	537840	-592272	2413152	-4917024	9208080	10668672							
-56783	22932	-252972	-353556	-546588	73809	796320	726264	-431928	-388016	-1022490	-796320	611604	-431928	73809	955584	687960	-796320	726264	-546588	-252972	859908						
-252972	1604448	537840	-4406724	-592272	-197964	6880608	2413152	1220832	1444608	-6667920	-4917024	-938952	1264896	-254340	5334336	9208080	-1251936	-1342656	2488320	1604448	955584	10668672					
73809	-254340	-197964	1507815	-1398060	1142910	-3769920	3392280	-482760	-3298320	4711770	-3764880	-1091070	-1636200	1507815	-6667920	-4263840	6894720	2984040	-6332580	-4406724	-1022490	-8731800	19652220				
-388016	1444608	1444608	-3298320	-2531520	-3298320	5054720	3640320	3640320	5054720	-3769920	-480960	-6205680	-480960	-3769920	6880608	8195040	158400	158400	8195040	6880608	796320	8844192	-16369920	25373440			
73809	-197964	-254340	1142910	-1398060	1507815	-3298320	-482760	3392280	-3769920	1507815	-1636200	-1091070	-3764880	4711770	-4406724	-6332580	2984040	6894720	-4263840	-6667920	-353556	-5930820	11889585	-16369920	19652220		
-252972	537840	1604448	-197964	-592272	-4406724	1444608	1220832	2413152	6880608	-254340	1264896	-938952	-4917024	-6667920	1604448	2488320	-1342656	-1251936	9208080	5334336	22932	2614032	-5930820	8844192	-8731800	10668672	
-56783	-252972	22932	73809	-546588	-353556	-388016	-431928	726264	796320	73809	-431928	611604	-796320	-1022490	-252972	-546588	726264	-796320	687960	955584	-56783	22932	-353556	796320	-1022490	955584	859908

Appendix B

Detailed Derivation of Pollaczek's Formula

Fig. B.1 shows the buried current filament in the earth. The properties of the air and the earth are given in the figure. x and y axes are established from origin O as shown in the figure. t axis is in the opposite direction of y. The location coordinates for the filament are (x_f, y_f) or (x_f, t_f) with $t_f = -y_f \geq 0$.

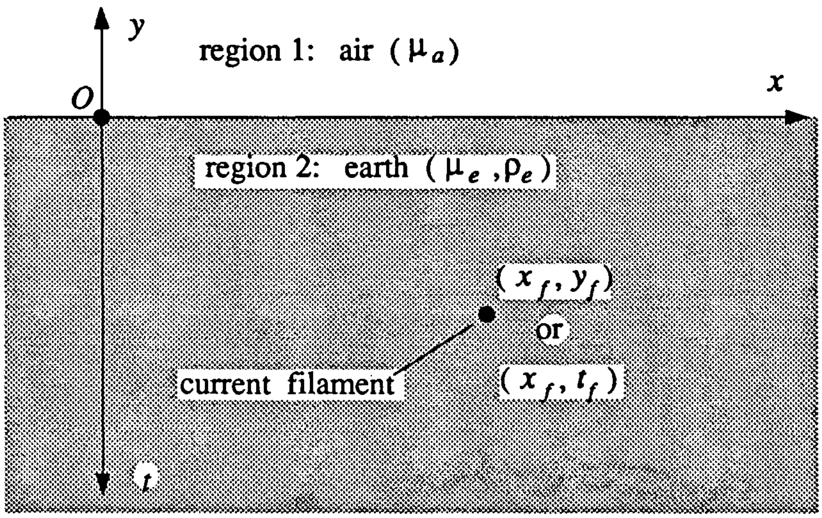

Figure B.1: A current filament buried in the earth

Applying the assumptions in Section 2.2 to this case the principal equations can be derived. Because of

$$\nabla \times \mathbf{E} = -j\omega \mathbf{B} \tag{B.1}$$

$$\frac{1}{\mu} \nabla \times \mathbf{B} = \mathbf{J} \tag{B.2}$$

$$\nabla \cdot \mathbf{E} = 0 \tag{B.3}$$

the following equation is got

$$\begin{aligned}\nabla\times\nabla\times\mathbf{E} &= \nabla(\nabla\cdot\mathbf{E})-\nabla^2\mathbf{E}=-\nabla^2\mathbf{E}\\ &= -j\omega\nabla\times\mathbf{B}=-j\omega\mu\mathbf{J}=\frac{-j\omega\mu}{\rho}\mathbf{E}\end{aligned} \tag{B.4}$$

The current density has one direction only. Therefore, the two-dimensional principal equation descibing the field in the problem is

$$\nabla^2 E = j\omega\mu J = \frac{1}{p^2}E \tag{B.5}$$

where

$$p^2 = \frac{\rho}{j\omega\mu} \tag{B.6}$$

p is the complex penetration depth. If E_a and E_e respectively represent E fields in the air and in the earth, (B.5) can now be splitted into two equations

$$\begin{aligned}\nabla^2 E_a &= 0 && y\geq 0 && \text{(B.7)}\\ \nabla^2 E_e &= \frac{1}{p_e^2}E_e + j\omega\mu_e I\delta(x-x_f)\delta(t-t_f) && t\geq 0 && \text{(B.8)}\end{aligned}$$

where

$$p_e^2 = \frac{\rho_e}{j\omega\mu_e} \tag{B.9}$$

I is the magnitude of the filament current. The Delta function is associated with the filament. The boundary conditions are

$$\begin{aligned}& E_a = E_e = E_0 && y=0 && \text{(B.10)}\\ & \frac{1}{\mu_a}\frac{\partial E_a}{\partial y} = \frac{1}{\mu_e}\frac{\partial E_e}{\partial y} = -\frac{1}{\mu_e}\frac{\partial E_e}{\partial t} && y=0; t=0 && \text{(B.11)}\\ & E_a = E_e = \frac{\partial E_a}{\partial x} = \frac{\partial E_e}{\partial x} = \frac{\partial E_a}{\partial y} = \frac{\partial E_e}{\partial y} = 0 && x=\infty \text{ and/or } y=\infty && \text{(B.12)}\end{aligned}$$

In order to solve (B.7) and (B.8) the integral transformation technique is applied. To x the following Fourier transformation pair is applied

$$\overline{f}(\alpha) = \int_{-\infty}^{\infty} f(x)e^{-j\omega x}dx \tag{B.13}$$

$$f(x) = \frac{1}{2\pi}\int_{-\infty}^{\infty} \overline{f}(\alpha)e^{jx\alpha}d\alpha \tag{B.14}$$

To y and t the following Fourier sine transformation pair is applied

$$\overline{f_s}(\lambda) = \int_0^{\infty} f(y)\sin(\lambda y)dy \tag{B.15}$$

$$f(y) = \frac{2}{\pi}\int_0^{\infty} \overline{f_s}(\lambda)\sin(y\lambda)d\lambda \tag{B.16}$$

For region 1, x and y are used as the coordinates. Define

$$\overline{E_a} = \int_{-\infty}^{\infty} E_a e^{-j\alpha x}dx \tag{B.17}$$

$$\overline{\overline{E_a}} = \int_0^{\infty} \overline{E_a}\sin(\lambda y)dy \tag{B.18}$$

Applying the Fourier transformation to x as

$$\begin{aligned}\int_{-\infty}^{\infty} \frac{\partial^2 E_a}{\partial x^2}e^{-j\alpha x}dx &= (-j\alpha)\frac{\partial E_a}{\partial x}e^{-j\alpha x}\Big|_{-\infty}^{\infty} - \int_{-\infty}^{\infty}\frac{\partial E_a}{\partial x}e^{-j\alpha x}(-j\alpha)dx \\ &= -E_a e^{-j\alpha x}(-j\alpha)^2\Big|_{-\infty}^{\infty} + \int_{-\infty}^{\infty} E_a e^{-j\alpha x}(-j\alpha)^2 dx \\ &= -\alpha^2\int_{-\infty}^{\infty} E_a e^{-j\alpha x}dx = -\alpha^2\overline{E_a} \end{aligned}\tag{B.19}$$

$$\int_{-\infty}^{\infty} \frac{\partial^2 E_a}{\partial y^2}e^{-j\alpha x}dx = \frac{\partial^2\overline{E_a}}{\partial y^2} \tag{B.20}$$

Then (B.7) becomes

$$-\alpha^2\overline{E_a} + \frac{\partial^2\overline{E_a}}{\partial y^2} = 0 \tag{B.21}$$

Applying the Fourier sine transformation to y as

$$\int_0^{\infty} -\alpha^2\overline{E_a}\sin(\lambda y)dy = -\alpha^2\overline{\overline{E_a}} \tag{B.22}$$

$$\begin{aligned}\int_0^{\infty}\frac{\partial^2\overline{E_a}}{\partial y^2}\sin(\lambda y)dy &= \frac{\partial\overline{E_a}}{\partial y}\sin(\lambda y)\Big|_0^{\infty} - \lambda\int_0^{\infty}\frac{\partial\overline{E_a}}{\partial y}\cos(\lambda y)dy \\ &= -\lambda\overline{E_a}\cos(\lambda y)\Big|_0^{\infty} - \lambda^2\int_0^{\infty}\overline{E_a}\sin(\lambda y)dy \\ &= \lambda\overline{E_0} - \lambda^2\overline{\overline{E_a}}\end{aligned}\tag{B.23}$$

(B.21) is changed to

$$\overline{\overline{E_a}} = \frac{\lambda}{\alpha^2 + \lambda^2}\overline{E_0} \tag{B.24}$$

For region2, x and t are used as the coordinates. Define

$$\overline{E_e} = \int_{-\infty}^{\infty} E_e e^{-j\alpha x} dx \tag{B.25}$$

$$\overline{\overline{E_e}} = \int_0^{\infty} \overline{E_e} \sin(\lambda t) dt \tag{B.26}$$

By similar process, the following equations can be derived

$$-\alpha^2 \overline{E_e} + \frac{\partial^2 \overline{E_e}}{\partial y^2} = \frac{1}{p_e^2}\overline{E_e} + j\omega\mu_e I e^{-j\alpha x_f}\delta(t - t_f) \tag{B.27}$$

$$(\alpha^2 + \frac{1}{p_e^2} + \lambda^2)\overline{\overline{E_e}} = \lambda\overline{E_0} - j\omega\mu_e I e^{-j\alpha x_f}\sin(\lambda t_f) \tag{B.28}$$

By assigning

$$\theta^2 = \alpha^2 + \frac{1}{p_e^2} \tag{B.29}$$

(B.28) becomes

$$\overline{\overline{E_e}} = \frac{\lambda}{\theta^2 + \lambda^2}\overline{E_0} - j\omega\mu_e I e^{-j\alpha x_f}\frac{\sin(\lambda t_f)}{\theta^2 + \lambda^2} \tag{B.30}$$

The inverse Fourier sine transformation is applied to (B.24) and (B.30) to get $\overline{E_a}$ and $\overline{E_e}$

$$\overline{E_a} = \frac{2}{\pi}\overline{E_0}\int_0^{\infty} \frac{\lambda \sin(y\lambda)}{\alpha^2 + \lambda^2} d\lambda \tag{B.31}$$

$$\overline{E_e} = \frac{2}{\pi}\overline{E_0}\int_0^{\infty} \frac{\lambda \sin(t\lambda)}{\theta^2 + \lambda^2} d\lambda - \frac{j2\omega\mu_e}{\pi} I e^{-j\alpha x_f}\int_0^{\infty} \frac{\sin(t_f\lambda)\sin(t\lambda)}{\theta^2 + \lambda^2} d\lambda \tag{B.32}$$

According to the mathematical handbook

$$\int_0^{\infty} \frac{\lambda \sin(y\lambda)}{\alpha^2 + \lambda^2} d\lambda = \frac{\pi}{2} e^{\alpha y} \quad \alpha \geq 0; y > 0 \tag{B.33}$$

$$= \frac{\pi}{2} e^{|\alpha| y} \quad y > 0 \tag{B.34}$$

$$\int_0^{\infty} \frac{\sin(t_f\lambda)\sin(t\lambda)}{\theta^2 + \lambda^2} d\lambda = \frac{\pi}{4\theta}\left(e^{-(t_f - t)\theta} - e^{-(t_f + t)\theta}\right) \quad \theta > 0; t_f \geq t \geq 0 \tag{B.35}$$

$$= \frac{\pi}{4\theta}\left(e^{-(t - t_f)\theta} - e^{-(t + t_f)\theta}\right) \quad \theta > 0; t \geq t_f \geq 0 \tag{B.36}$$

$$= \frac{\pi}{4|\theta|}\left(e^{-|t - t_f||\theta|} - e^{-|t + t_f||\theta|}\right) \tag{B.37}$$

Therefore,

$$\overline{E_a} = \overline{E_0} e^{-|\alpha| y} \tag{B.38}$$

$$\overline{E_e} = \overline{E_0} e^{-|\theta| t} - j\omega\mu_e I e^{-j\alpha x_f} \frac{1}{2|\theta|} \left(e^{-|t-t_f||\theta|} - e^{-|t+t_f||\theta|} \right) \tag{B.39}$$

Using boundary condition (B.11) $\overline{E_0}$ can be solved from the above two equations. Because

$$\left. \frac{\partial \overline{E_a}}{\partial y} \right|_{y=0} = -|\alpha| \overline{E_0} e^{-|\alpha| y} \Big|_{y=0} = -|\alpha| \overline{E_0} \tag{B.40}$$

$$\begin{aligned} \left. \frac{\partial \overline{E_e}}{\partial t} \right|_{t=0} &= -|\theta| \overline{E_0} e^{-|\theta| t} \Big|_{t=0} - j\omega\mu_e I e^{-j\alpha x_f} \frac{1}{2|\theta|} \left(|\theta| e^{(t-t_f)|\theta|} + |\theta| e^{(-t-t_f)|\theta|} \right) \Big|_{t=0} \\ &= -|\theta| \overline{E_0} - j\omega\mu_e I e^{-j\alpha x_f} e^{-t_f|\theta|} \end{aligned} \tag{B.41}$$

the following equation is got

$$-\frac{1}{\mu_a} |\alpha| \overline{E_0} = -\frac{1}{\mu_e} \left(-|\theta| \overline{E_0} - j\omega\mu_e I e^{-j\alpha x_f} e^{-t_f|\theta|} \right) \tag{B.42}$$

Therefore, $\overline{E_0}$ is given by

$$\overline{E_0} = -\frac{j\omega I e^{-j\alpha x_f} e^{-t_f|\theta|}}{\frac{1}{\mu_a}|\alpha| + \frac{1}{\mu_e}|\theta|} = -\frac{j\omega I e^{-j\alpha x_f} e^{-t_f\sqrt{\alpha^2+1/p_e^2}}}{\frac{1}{\mu_a}|\alpha| + \frac{1}{\mu_e}\sqrt{\alpha^2+1/p_e^2}} \tag{B.43}$$

The final solution of E_a and E_e can be got by applying the inverse Fourier transformation to (B.38) and (B.39) with $\overline{E_0}$ being replaced by (B.43). Also, t and t_f can now be changed back to $-y$ and $-y_f$, respectively. E_a and E_e are given by

$$\begin{aligned} E_a &= \frac{1}{2\pi} \int_{-\infty}^{\infty} \overline{E_a} e^{jx\alpha} d\alpha \\ &= -\frac{j\omega I}{2\pi} \int_{-\infty}^{\infty} \frac{e^{-t_f\sqrt{\alpha^2+1/p_e^2} - |\alpha| y}}{\frac{1}{\mu_a}|\alpha| + \frac{1}{\mu_e}\sqrt{\alpha^2+1/p_e^2}} e^{j(x-x_f)\alpha} d\alpha \\ &= -\frac{j\omega I}{\pi} \int_0^{\infty} \frac{e^{-y\alpha + y_f\sqrt{\alpha^2+1/p_e^2}}}{\frac{1}{\mu_a}\alpha + \frac{1}{\mu_e}\sqrt{\alpha^2+1/p_e^2}} \cos((x-x_f)\alpha) d\alpha \end{aligned} \tag{B.44}$$

$$
\begin{aligned}
E_e &= \frac{1}{2\pi}\int_{-\infty}^{\infty}\overline{E_e}e^{jx\alpha}d\alpha \\
&= -\frac{j\omega I}{2\pi}\int_{-\infty}^{\infty}\frac{e^{-t_f\sqrt{\alpha^2+1/p_e^2}-|\theta|t}}{\frac{1}{\mu_a}|\alpha|+\frac{1}{\mu_e}\sqrt{\alpha^2+1/p_e^2}}e^{j(x-x_f)\alpha}d\alpha \\
&\quad -\frac{j\omega\mu_e I}{2\pi}\int_{-\infty}^{\infty}\frac{e^{-|t-t_f||\theta|}-e^{-|t+t_f||\theta|}}{2|\theta|}e^{j(x-x_f)\alpha}d\alpha \\
&= -\frac{j\omega I}{\pi}\int_{0}^{\infty}\frac{e^{(y+y_f)\sqrt{\alpha^2+1/p_e^2}}}{\frac{1}{\mu_a}\alpha+\frac{1}{\mu_e}\sqrt{\alpha^2+1/p_e^2}}\cos((x-x_f)\alpha)d\alpha \\
&\quad -\frac{j\omega\mu_e I}{2\pi}\int_{-\infty}^{\infty}\frac{e^{-|-y+y_f|\sqrt{\alpha^2+1/p_e^2}}-e^{-|-y-y_f|\sqrt{\alpha^2+1/p_e^2}}}{2\sqrt{\alpha^2+1/p_e^2}}e^{j(x-x_f)\alpha}d\alpha
\end{aligned} \tag{B.45}
$$

E_e in the above equation can be further simplified into

$$
E_e = -\frac{j\omega\mu_e I}{2\pi}\left(\mathrm{K}_0(D/p_e)-\mathrm{K}_0(D'/p_e)+\int_0^{\infty}\frac{2e^{(y+y_f)\sqrt{\alpha^2+1/p_e^2}}}{\frac{\mu_e}{\mu_a}\alpha+\sqrt{\alpha^2+1/p_e^2}}\cos((x-x_f)\alpha)d\alpha\right) \tag{B.46}
$$

where

$$
\mathrm{K}_0(D/p_e) = \int_{-\infty}^{\infty}\frac{e^{-|-y+y_f|\sqrt{\alpha^2+1/p_e^2}}}{2\sqrt{\alpha^2+1/p_e^2}}e^{j(x-x_f)\alpha}d\alpha \tag{B.47}
$$

$$
\mathrm{K}_0(D'/p_e) = \int_{-\infty}^{\infty}\frac{e^{-|-y-y_f|\sqrt{\alpha^2+1/p_e^2}}}{2\sqrt{\alpha^2+1/p_e^2}}e^{j(x-x_f)\alpha}d\alpha \tag{B.48}
$$

$$
D = \sqrt{(x-x_f)^2+(y-y_f)^2} \tag{B.49}
$$

$$
D' = \sqrt{(x-x_f)^2+(y+y_f)^2} \tag{B.50}
$$

K_0 is the zero order second kind modified Bessel funciton.

Appendix C

List of Symbols

$\mathbf{A}$, A	:	magnetic vector potential
$[A]$	:	A vector
A_b	:	A function values on FEM boundary
$[A_B]$	:	A vector of Dirichlet boundary nodes
A_{B_i}	:	element of $[A_B]$
a_k	:	distance to centre of PT cable of the kth SC cable (k=A,B,C)
a_n	:	unknown coefficient for trial function φ_n
a_{mi}	:	polynomial coefficient in $P_m(N_p, \zeta)$
A_n	:	value of A at global node n
$A_{(k)}$	:	A distribution in conductor k
$A_{(ki)}$	:	A distribution in conductor k caused by conductor current I_i
$[A^{E_l}_{(ki)}]$	:	vector of $A_{(ki)}$ values in element E_l
$[A^{E_i}]$	:	vector of A values at local nodes in element E_i
$A^{E_i}_n$	:	element of $[A^{E_i}]$
$[A_U]$	:	A vector of unknown nodes
$\mathbf{B}$, B	:	magnetic field density
$[C]$	:	shunt capacitance matrix per unit length of transmission lines
C_{D_i}	:	coefficient in the formulas of SC coaxial cables
C_{I_i}	:	coefficient in the formulas of SC coaxial cables
C_{IN_k}	:	capacitance of the kth insulation in a SC cable

C_{K_i} : coefficient in the formulas of SC coaxial cables

C_k^d : diagonal element in $[C]$ of SC coaxial cables

C_k^{od} : off diagonal element in $[C]$ of SC coaxial cables

$C_{s_{i0}}$: direct self capacitance of conductor i

$C_{m_{ij}}$: direct mutual capacitance between conductors i and j

C_{ik} : element of $[C]$

c_p : perturbation coefficient of the earth

d : differentiation

$[D^{E_i}]$: shape function differentiation matrix in element E_i

$\mathbf{D}$: charge density

D : distance between a field point and a cable or diameter of strands

D' : distance between a field point and the image of a cable

$[D]$: submatrix in $[U] + j\omega[T]$ related to unknown nodes

$[D_B]$: submatrix in $[U] + j\omega[T]$ related to boundary nodes

$[D_L]$: banded lower triangular matrix

$[D_U]$: banded upper triangular matrix

d_m : common denominator in $P_m(N_p, \zeta)$

d_{ij} : width of the jth division from a surface of the ith conductor

$det[\,]$: determinant of a matrix

$diag(\,)$: a diagonal matrix

$\mathbf{dl}$: integral element

$\mathbf{E}$, E : electrical field

E_0 : E value on the earth surface

E_a : E field in the air

E_b : E function values on FEM boundary

E_B : vector of node values of E_b in a FEM mesh

E_C : E field in the earth with a deeply buried SC cable

E_e : E field in the earth

E_F : E field in the earth with a deeply buried current filament

E_i : element i in a FEM mesh

$[E_S]$: source electrical field vector

E_{S_i} : source electrical field in conductor i

$\overline{f}()$: inverse Fourier transformation of $f()$

$[F]$: integral coefficient matrix related to unknown nodes

$[F']$: update of $[F]$

$[F_A]$: a matrix modified from $[F]$

$[F_B]$: integral coefficient matrix related to Dirichlet nodes

f_{dj} : division factor for the jth division

F_{mk} : elements in matrix $[F]$

$F_{B_{lk}}$: elements in matrix $[F_B]$

$F_{mk}^{E_i}$: F_{mk} in local node numbers in element E_i

$F_{B_{lk}}^{E_i}$: $F_{B_{lk}}$ in local node numbers in element E_i

$[F_H]$: horizontal vector related to $[F]$

$[F'_H]$: update of $[F_H]$

$\overline{f_s}()$: inverse Fourier sine transformation of $f()$

$[F_V]$: a vector related to $[E_B]$

$[G]$: shunt conductance matrix per unit length of transmission lines

$[G_C]$: diagonal conductivity matrix of conductors

$g_0(x, y)$: Dirichlet boundary function

h : burial depth of an underground cable or a current filament

H : magnetic field

h_2, h_3 : layout geometry parameters of tunnel installed SC cables

i : index

I : conductor current

$[I]$: conductor current vector

I_{e_R}, I_{e_I} : real and imaginary parts of the earth current

I_n : the 1st kind modified Bessel function of the nth order

$[I_R]$, $[I_I]$: real part and imaginary part of $[I]$

$\mathrm{I}_0()$, $\mathrm{I}_1()$: first kind modified Bessel functions in 1st and 2nd order

I_i : conductor current in conductor i

I_{R_i}, I_{I_i} : real part and imaginary part of I_i

I_{A_i} : internal return current of cylindrical conductor i

I_{B_i} : external return current of cylindrical conductor i

$I_F(r)$: earth current within r of a deeply buried current filament

$[I_{E1}]$, $[I_{E2}]$: equivalent current vectors due to boundary conditions

$[I_{E3}]$, $[I_{E4}]$: equivalent current vectors due to boundary condition $[E_B]$

$[I'_{E1}]$, $[I'_{E2}]$: updates of $[I_{E1}]$ and $[I_{E2}]$

I_{ep} : partial earth return current

I_{ep_C} : partial earth return current of a deeply buried SC coaxial cable

I_{ep_F} : partial earth return current of a deeply buried current filament

j : complex number exclaimer or index

$\mathbf{J}$, J : current density

$J_{(i)}$: J distribution in conductor i

$J_{(ij)}$: J distribution in conductor i caused by conductor current I_j

$[J_{(ij)}^{E_l}]$: vector of $J_{(ij)}$ values in element E_l

J_R, J_I : real and imaginary part of J

J_S : source current density

$[J_S]$: source current density vector

J_{S_i} : source current density in conductor i

$[J_a^{E_i}]$: Jacobian transformation matrix in element E_i

k : index

K : number of conductors

$\mathrm{K}_0(),\ \mathrm{K}_1()$: second kind modified Bessel functions in 1st and 2nd order

K_f : factor in the GSW formula

K_n : the 2st kind modified Bessel function of the nth order

$[L(\omega)],\ [L]$: series inductance matrix per unit length of transmission lines

l : index

L_C : contour length of a sector-shaped core conductor

$[L_C(\omega)]$: series inductance matrix per unit length related to conductors

$[L_D]$: series inductance matrix per unit length related to dielectrics

L_{ij} : elements of $[L]$

M : number of elements in a FEM mesh

m : index

N : number of unknown nodes in a FEM mesh, number of space dimension

n : index or the number of outer strands

N_B : number of Dirichlet boundary nodes in a FEM mesh

N_{B_E} : number of Dirichlet boundary nodes in the earth

N_{E_i} : number of nodes in element E_i

N_p : degree of the auxiliary polynomials for simplex elements

N_S : number of sampling points in an isoparametric element

N_T : total number of nodes in a FEM mesh $N_T = N + N_B$

O : origin of x-y coordinates

$O()$: index sting for $[Q^{(k)}]$

$o(h_i)$: order of estimate errors

p : complex penetration depth

P : time-average power loss in a system or a field point

$P_m(N_p, \zeta)$: auxiliary polynomials of degree N_p

p_e : earth complex penetration depth

p_{ij} : time-average power loss related to conductor currents I_i and I_j

p_i : complex penetration depth of conductor i

Q : time-average reactive power in a system

$[q]$: vector of surface charges on conductors

q_i : surface charge on conductor i

q_{ij} : time-average reactive power related to conductor currents I_i and I_j

$\triangle q$: surface charge on an element side

$[Q^{(k)}]$: real integral matrices in simplex elements ($k = 1, 2, 3$)

$Q^{(k)}_{mn}$: element of $[Q^{(k)}]$

r : radius in polar coordinate system or the radius of outer strands

r_b : FEM boundary radius

r_e : inner earth radius or the outer radius of a stranded conductor

r_{eq} : equivalent radius from Borges da Silva's formula

r_A, r_B : inner and outer radii of an equivalent circular conductor

r_{A_i}, r_{B_i} : internal and external radii of cylindrical conductor i

$[R(\omega)]$, $[R]$: series resistance matrix per unit length of transmission lines

R_C : internal resistance of stranded conductors from the GSW formula

R_{ij} : elements of $[R]$

Re() : real part of the function

s : separation distance of SC cables

S : time-average complex power, or the eara of a triangle

S_1, S_2, S_3 : areas of subtriangles

S_C : cross-section area of a sector-shaped core conductor

S_R : solution region

$[S_C]$: conductor cross-section area matrix

$[S'_C]$: update of $[S_C]$

$[S_{C_A}]$: a matrix modified from $[S_C]$

S_{C_k} : cross-section area of conductor k

$[S_{C_V}]$: a vector related to $[E_B]$

S_{E_i} : region or area of element E_i

t : time or t axis in the opposition direction of y axis

t_f : t coordinate of a buried filament

$[T]$: coefficient matrix

T_{mn} : elements of $[T]$

$[T^{E_i}]$: imaginary integral matrix for isoparametric element E_i

$T^{E_i}_{mn}$: element of $[T^{E_i}]$

$[T_S]$: imaginary integral matrix for simplex elements

$T_{S_{mn}}$: elements of $[T_S]$

$[U]$: coefficient matrix

$[U^{E_i}]$: $[U]$ in element E_i

U_{mn} : elements of $[U]$

$U^{E_i}_{mn}$: U_{mn} in local node numbers in element E_i

$\mathbf{u_z}$: unit vector of z axis in Cartician coordinate system

$\mathbf{u_\theta}$: unit vector of θ axis in Polar coordinate system

$[V]$: conductor voltage vector with respect to the reference conductor

V_i : conductor voltage of conductor i

w : layout geometry parameter of tunnel installed SC cables

W_{E_F} : electric energy found from the numerical field solution

$W_{E_F}^{ij}$: W_{E_F} with conductors i and j energized

$W_{E_C}^{ij}$: electric energy from circuit analysis with conductors i and j energized

W_j : weighting factor of numerical integration for isoparametric elements

W_M : time-average magnetic energy stored in a system

$w_{M_{ij}}$: time-average magnetic energy related to conductor currents I_i and I_j

x, y : x and y axes perpendicular to the transmission line

x_1, x_2, x_3 : x coordinates of vertices in a simplex

x_f, y_f : x and y of a buried filament

$[x^{E_i}]$: vector of x coordinates of vertices for isoparametric element E_i

x_n, y_n : x and y coordinates of node n in a FEM mesh

x_P, y_P : x and y coordinates of field point P

y_1, y_2, y_3 : y coordinates of vertices in a simplex

$[y^{E_i}]$: vector of y coordinates of vertices for isoparametric element E_i

$[Y(\omega)]$, $[Y]$: shunt admittance matrix per unit length of transmission lines

z : z axis parallel with the transmission line

$[Z(\omega)]$, $[Z]$: series impedance matrix per unit length of transmission lines

Z_e : earth return impedance

Z_{ij} : elements of $[Z]$

Z_{kl} : submatrix in $[Z]$ related to phases k and l (k,l=A,B,C)

Z_{A_i} : internal surface impedance of cylindrical conductor i

Z_{B_i} : external surface impedance of cylindrical conductor i

Z_{M_i} : transfer impedance of cylindrical conductor i

Z_k^d : diagonal element (k,k) in $[Z]$ of a SC coaxial cable

Z_k^{od} : off diagonal element (i,k) and (k,j) $(i,j < k)$ in $[Z]$ of a SC coaxial cable

Z_{EQ_i} : equivalent impedance related to cylindrical conductors i nad $i+1$

Z_{D_i} : impedance related to the dielectrics between cylindrical conductors i and j

$[\mathbf{1}_V]$: a vector filled with 1 and 0

$[\ ]^t$: transposition of the matrix

$[\ ]^*$: conjugate of the function

$|\ |$: absolute value of the function

α : variable in Fourier transformation

$\alpha_{m_1 m_2 m_3}$: shape function for simplex elements

$[\beta]$: shape function vector for isoparametric elements

β_i : shape function for isoparametric elements

δ : real penetration depth in conductors

δ_i : δ in conductor i

δ_e : δ in the earth

$\delta()$: Deric function

δ : real penetration depth in conductors

ϵ : permittivity

ϵ_{E_i} : permittivity in element E_i

ϵ_k : permittivity of the k insulation

ϵ_r : relative permittivity

ζ : simplex coordinate

ζ_i : simplex coordinate i

θ : a variable or span angle of sector-shaped regions

$\theta_k^{E_i}$: include angle of vertex k in simplex element E_i

λ : wave length or variable in Fourier sine transformation

ψ_0 : function to enforce the Dirichlet boundary condition

μ : permeability

μ_a : permeability in the air

μ_e : permeability in the earth

μ_0 : permeability in the vacuum

μ_r : relative permeability

μ_k : permeability in conductor k

μ_{E_i} : permeability in element E_i

ρ : volume charge density or conductor resistivity

ρ_e : earth resistivity

σ : conductivity

σ_k : conductivity in conductor k

σ_{E_i} : conductivity in element E_i

(v, ν) : local coordinates for isoparametric elements

(v_j, ν_k) : sampling point local coordinates in isoparametric elements

(v, ν) : local coordinates for isoparametric elements

ϕ : electrical scalar potential or position angle

$[\phi]$: electrical scalar potential vector

ϕ_n : value of ϕ at global node n

$\phi_n^{E_i}$: local node value of ϕ in element E_i

$[\phi^{E_i}]$: $[\phi]$ in element E_i

ω : radius frequency

φ_n : trial function for global node n

φ_{B_i} : trial function for Dirichlet node i

$\varphi_n^{E_i}$: trial function for local node n in element E_i

Γ : boundary surrounding the solution region S_R

Γ_0 : Dirichlet boundary

Γ_1 : homogeneous Neumann boundary

Γ_{C_j} : periphery of the cross-section area of conductor j